

AD-A222 202

NAVAL POSTGRADUATE SCHOOL Monterey, California



THESIS

DTIC
ELECTE
JUN 04 1990
S E D
Co

FLOW VISUALIZATION OF DYNAMIC STALL
ON AN OSCILLATING AIRFOIL

by

Bruce E. Brydges

September 1989

Thesis Advisor:

M. S. Chandrasekhara

Approved for public release; distribution is unlimited

99 05 31 093

UNCLASSIFIED

SECURITY CLASSIFICATION OF THIS PAGE

REPORT DOCUMENTATION PAGE

1a REPORT SECURITY CLASSIFICATION Unclassified			1b RESTRICTIVE MARKINGS		
2a SECURITY CLASSIFICATION AUTHORITY			3 DISTRIBUTION/AVAILABILITY OF REPORT		
2b DECLASSIFICATION/DOWNGRADING SCHEDULE			Approved for public release; distribution is unlimited.		
4 PERFORMING ORGANIZATION REPORT NUMBER(S)			5 MONITORING ORGANIZATION REPORT NUMBER(S)		
6a NAME OF PERFORMING ORGANIZATION Naval Postgraduate School		6b OFFICE SYMBOL (If Applicable) 31	7a NAME OF MONITORING ORGANIZATION Naval Postgraduate School		
6c ADDRESS (City, State, and ZIP Code) Monterey, CA 93943-5000		7b ADDRESS (City, State, and ZIP Code) Monterey, CA 93943-5000			
8a NAME OF FUNDING/SPONSORING ORGANIZATION		8b OFFICE SYMBOL (If Applicable)	9 PROCUREMENT INSTRUMENT IDENTIFICATION NUMBER		
8c ADDRESS (City, State, and ZIP Code)			10 SOURCE OF FUNDING NUMBERS		
			PROGRAM ELEMENT NO.	PROJECT NO.	TASK NO. WORK UNIT ACCESSION NO.
11 TITLE(Include Security Classification) FLOW VISUALIZATION OF DYNAMIC STALL ON AN OSCILLATING AIRFOIL					
12 PERSONAL AUTHOR(S) BRYDGES, BRUCE E.					
13a TYPE OF REPORT Master's Thesis		13b TIME COVERED From To		14 DATE OF REPORT (Year, Month, Day) 1989 September	
				15 PAGE COUNT 116	
16 SUPPLEMENTARY NOTATION The views expressed in this thesis are those of the author and do not reflect the official policy or position of the Department of Defense or the U.S. Government.					
17 COSATI CODES			18 SUBJECT TERMS (Continue on reverse if necessary and identify by block number)		
FIELD	GROUP	SUB-GROUP	Dynamic Stall; Dynamic lift, Unsteady lift; Helicopter retreating blade stall; Oscillating airfoil; Flow visualization; Schlieren method; <i>Theses. (jkl)</i>		
19 ABSTRACT (Continue on reverse if necessary and identify by block number) <i>at infinity</i> Stroboscopic schlieren photography was used to investigate the effects of compressibility, reduced frequency, and amplitude on the dynamic stall of a NACA 0012 airfoil subjected to sinusoidal oscillation. The Mach number was varied from $M_\infty = 0.25$ to $M_\infty = 0.45$ (corresponding to a Reynolds number variation of $Re = 450,000$ to $Re = 810,000$); the reduced frequency was varied from $k = 0.025$ to $k = 0.10$. Oscillation amplitudes of $\alpha_m = 5^\circ$ and $\alpha_m = 10^\circ$ were compared. Schlieren photographs are presented, which document the dynamic stall vortex formation, convection, and shedding sequence for various experimental conditions. Additionally, a preliminary examination of the flow reattachment process was conducted. Data derived from the photographs indicates that increasing the compressibility causes dynamic stall to occur at lower angles of attack; while, increasing the reduced frequency and/or the oscillation amplitude effectively delays dynamic stall effects to a higher angle of attack. Flow reattachment is sensitive to both Mach number and reduced frequency for low values of these parameters; when either the Mach number or reduced frequency is sufficiently high, the reattachment process stabilizes. <i>Keywords:</i>					
20 DISTRIBUTION/AVAILABILITY OF ABSTRACT <input checked="" type="checkbox"/> UNCLASSIFIED/UNLIMITED <input type="checkbox"/> SAME AS RPT. <input type="checkbox"/> DTIC USERS			21 ABSTRACT SECURITY CLASSIFICATION Unclassified		
22a NAME OF RESPONSIBLE INDIVIDUAL M. S. Chandrasekhara			22b TELEPHONE (Include Area code) (415) 694-4269		22c OFFICE SYMBOL Code 31CH

DD FORM 1473, JUNE 86

Previous editions are obsolete

SECURITY CLASSIFICATION OF THIS PAGE

S/N 0102-LF-014-6603

UNCLASSIFIED

*alpha sub n**day i*

Approved for public release; distribution is unlimited.

Flow Visualization of Dynamic Stall on an Oscillating Airfoil

by

Bruce E. Brydges
Captain, United States Army
B.S., United States Military Academy, 1979


Submitted in partial fulfillment of the
requirements for the degree of

MASTER OF SCIENCE IN AERONAUTICAL ENGINEERING

from the

NAVAL POSTGRADUATE SCHOOL
September 1989

Author:



Bruce E. Brydges

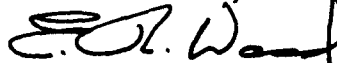
Approved by:



Muguru S. Chandrasekhara, Thesis Advisor



Max F. Platzer, Second Reader



E. Roberts Wood, Chairman,
Department of Aeronautics and Astronautics

ABSTRACT

Stroboscopic schlieren photography was used to investigate the effects of compressibility, reduced frequency, and amplitude on the dynamic stall of a NACA 0012 airfoil subjected to sinusoidal oscillation. The Mach number was varied from $M_\infty = 0.25$ to $M_\infty = 0.45$ (corresponding to a Reynolds number variation of $Re = 450,000$ to $Re = 810,000$); the reduced frequency was varied from $k = 0.025$ to $k = 0.10$. Oscillation amplitudes of $\alpha_m = 5^\circ$ and $\alpha_m = 10^\circ$ were compared. Schlieren photographs are presented, which document the dynamic stall vortex formation, convection, and shedding sequence for various experimental conditions. Additionally, a preliminary examination of the flow reattachment process was conducted. Data derived from the photographs indicates that increasing the compressibility causes dynamic stall to occur at lower angles of attack; while, increasing the reduced frequency and/or the oscillation amplitude effectively delays dynamic stall effects to a higher angle of attack. Flow reattachment is sensitive to both Mach number and reduced frequency for low values of these parameters; when either the Mach number or reduced frequency is sufficiently high, the reattachment process stabilizes.



Accession For	
NTIS GRA&I	<input checked="" type="checkbox"/>
DTIC TAB	<input checked="" type="checkbox"/>
Unannounced	<input type="checkbox"/>
Justification	
By _____	
Distribution/	
Availability Codes	
Dist	Avail and/or Special
A-1	

TABLE OF CONTENTS

I.	INTRODUCTION	1
A.	HELICOPTER ROTOR BEHAVIOR IN FORWARD FLIGHT	1
B.	DYNAMIC LIFT/STALL	2
1.	Dynamic Stall Events	2
2.	Stall Regimes	4
C.	THESIS GOALS	5
II.	DESCRIPTION OF THE EXPERIMENT	7
A.	FACILITY	7
1.	Wind Tunnel	7
a.	Drive System	7
b.	Inflow Section	8
c.	Test Section	8
d.	Tunnel Throat	10
2.	Instrumentation	10
3.	Stroboscopic Schlieren System	11
B.	PROCEDURE	13
C.	EXPERIMENTAL CONDITIONS	14
III.	RESULTS AND DISCUSSION	15
A.	STROBOSCOPIC SCHLIEREN ANALYSIS	15
B.	COMPRESSIBILITY EFFECTS	17
C.	REDUCED FREQUENCY EFFECTS	20
D.	AMPLITUDE EFFECTS	22

E.	CONVECTION VELOCITY OF THE DYNAMIC STALL VORTEX	24
F.	REATTACHMENT	26
IV.	CONCLUSIONS AND RECOMMENDATIONS	28
A.	CONCLUSIONS	28
B.	RECOMMENDATIONS	28
	APPENDIX A – NOMENCLATURE	30
	APPENDIX B – FIGURES	32
	LIST OF REFERENCES	101
	INITIAL DISTRIBUTION LIST	103

LIST OF FIGURES

Figure

1.	Angle of Attack Distribution for Example Helicopter -----	32
2.	Events of Dynamic Stall on NACA 0012 Airfoil -----	33
3.	Dynamic Stall Regimes -----	34
4.	Viscous Interaction During Dynamic Stall -----	35
5.	Local Mach Number on Leading Edge of an Oscillating Airfoil vs. Freestream Mach Number -----	36
6.	Schematic of the Compressible Dynamic Stall Facility -----	37
7.	Side View of the Test Section -----	38
8.	End View of the Test Section -----	39
9.	Airfoil Support Structure -----	40
10.	Transition to Stall; $M_\infty = 0.25$, $Re = 450,000$, $k \approx 0.025$ -----	41
11.	Transition to Stall; $M_\infty = 0.25$, $Re = 450,000$, $k \approx 0.050$ -----	42
12.	Transition to Stall; $M_\infty = 0.25$, $Re = 450,000$, $k \approx 0.075$ -----	43
13.	Transition to Stall; $M_\infty = 0.25$, $Re = 450,000$, $k \approx 0.10$ -----	44
14.	Transition to Stall; $M_\infty = 0.30$, $Re = 540,000$, $k \approx 0.025$ -----	45
15.	Transition to Stall; $M_\infty = 0.30$, $Re = 540,000$, $k \approx 0.050$ -----	46
16.	Transition to Stall; $M_\infty = 0.30$, $Re = 540,000$, $k \approx 0.075$ -----	47
17.	Transition to Stall; $M_\infty = 0.30$, $Re = 540,000$, $k \approx 0.10$ -----	48
18.	Transition to Stall; $M_\infty = 0.35$, $Re = 630,000$, $k \approx 0.025$ -----	49
19.	Transition to Stall; $M_\infty = 0.35$, $Re = 630,000$, $k \approx 0.050$ -----	50

20.	Transition to Stall; $M_\infty = 0.35$, $Re = 630,000$, $k = 0.075$	51
21.	Transition to Stall; $M_\infty = 0.35$, $Re = 630,000$, $k = 0.10$	52
22.	Transition to Stall; $M_\infty = 0.40$, $Re = 720,000$, $k = 0.025$	53
23.	Transition to Stall; $M_\infty = 0.40$, $Re = 720,000$, $k = 0.050$	55
24.	Transition to Stall; $M_\infty = 0.40$, $Re = 720,000$, $k = 0.075$	56
25.	Transition to Stall; $M_\infty = 0.45$, $Re = 810,000$, $k = 0.025$	57
26.	Transition to Stall; $M_\infty = 0.45$, $Re = 810,000$, $k = 0.050$	58
27.	Transition to Stall; $M_\infty = 0.45$, $Re = 810,000$, $k = 0.075$	59
28.	Compressibility Effects on Transition to Stall	60
29.	Reduced Frequency Effects on Transition to Stall	62
30.	Amplitude Effects on Transition to Stall; $M = 0.25$, $Re = 450,000$	65
31.	Amplitude Effects on Transition to Stall; $M = 0.30$, $Re = 540,000$	67
32.	Amplitude Effects on Transition to Stall; $M = 0.35$, $Re = 630,000$	69
33.	Amplitude Effects on Transition to Stall; $M = 0.40$, $Re = 720,000$	71
34.	Amplitude Effects on Transition to Stall; $M = 0.45$, $Re = 810,000$	72
35.	Convection Velocity of the Dynamic Stall Vortex; $M = 0.25$, $Re = 450,000$	73
36.	Convection Velocity of the Dynamic Stall Vortex; $M = 0.30$, $Re = 540,000$	74
37.	Convection Velocity of the Dynamic Stall Vortex; $M = 0.35$, $Re = 630,000$	75
38.	Convection Velocity of the Dynamic Stall Vortex; $M = 0.40$, $Re = 720,000$	76
39.	Convection Velocity of the Dynamic Stall Vortex; $M = 0.45$, $Re = 810,000$	77

40.	Reattachment; $M = 0.25$, $Re = 450,000$, $k = 0.025$	78
41.	Reattachment; $M = 0.25$, $Re = 450,000$, $k = 0.050$	79
42.	Reattachment; $M = 0.25$, $Re = 450,000$, $k = 0.075$	80
43.	Reattachment; $M = 0.25$, $Re = 450,000$, $k = 0.10$	81
44.	Reattachment; $M = 0.30$, $Re = 540,000$, $k = 0.025$	82
45.	Reattachment; $M = 0.30$, $Re = 540,000$, $k = 0.050$	83
46.	Reattachment; $M = 0.30$, $Re = 540,000$, $k = 0.075$	84
47.	Reattachment; $M = 0.30$, $Re = 540,000$, $k = 0.10$	85
48.	Reattachment; $M = 0.35$, $Re = 630,000$, $k = 0.025$	86
49.	Reattachment; $M = 0.35$, $Re = 630,000$, $k = 0.050$	87
50.	Reattachment; $M = 0.35$, $Re = 630,000$, $k = 0.075$	88
51.	Reattachment; $M = 0.35$, $Re = 630,000$, $k = 0.10$	89
52.	Reattachment; $M = 0.40$, $Re = 720,000$, $k = 0.025$	90
53.	Reattachment; $M = 0.40$, $Re = 720,000$, $k = 0.050$	91
54.	Reattachment; $M = 0.40$, $Re = 720,000$, $k = 0.075$	92
55.	Reattachment; $M = 0.45$, $Re = 810,000$, $k = 0.025$	93
56.	Reattachment; $M = 0.45$, $Re = 810,000$, $k = 0.050$	94
57.	Reattachment; $M = 0.45$, $Re = 810,000$, $k = 0.075$	95
58.	Compressibility Effects on Reattachment	96
59.	Reduced Frequency Effects on Reattachment	98

LIST OF TABLES

Table

I.	Experimental Conditions — $\alpha(t) = 10^\circ + 5^\circ \sin(\omega t)$ -----	14
II.	Vortex Formation Angles of Attack — $\alpha(t) = 10^\circ + 5^\circ \sin(\omega t)$ -----	19
III.	Vortex Formation Locations — $\alpha(t) = 10^\circ + 5^\circ \sin(\omega t)$ -----	19
IV.	Vortex Release Angles of Attack — $\alpha(t) = 10^\circ + 5^\circ \sin(\omega t)$ -----	20
V.	Vortex Formation Angles of Attack — $\alpha(t) = 10^\circ + 10^\circ \sin(\omega t)$ -----	22
VI.	Vortex Formation Locations — $\alpha(t) = 10^\circ + 10^\circ \sin(\omega t)$ -----	23
VII.	Vortex Release Angles of Attack — $\alpha(t) = 10^\circ + 10^\circ \sin(\omega t)$ -----	23

ACKNOWLEDGEMENTS

This research was conducted at the Fluid Mechanics Laboratory of the NASA Ames Research Center. I am deeply indebted to the entire staff for their constant, professional support. I wish to thank Dr. Sanford S. Davis, Chief, FML, for providing me with the resources and technical/administrative services necessary to complete this investigation. Dr. Larry Carr, Jim Laub and David Yaste were always willing to provide their time and a helping hand; I am appreciative. I am especially grateful to Michael Fidrich for his daily, hands-on assistance in conducting the experiment.

I would like to extend my sincere appreciation to Dr. M. S. Chandrasekhara for providing me with the opportunity, background and motivation to conduct this research. His interest and expertise in the field of unsteady fluid dynamics were invaluable.

Mr. Jorge Rios, of the Imaging Technology Branch, NASA Ames, provided fast and friendly support in processing of the photographs which were the basis of this examination. He was instrumental in its timely completion.

Finally, I want to thank my wife, Lou Ann, for her patience and understanding.

I. INTRODUCTION

A. HELICOPTER ROTOR BEHAVIOR IN FORWARD FLIGHT

The local angle of attack on a rotor blade element for a helicopter in forward flight is a function of many parameters, including:

- The forward velocity of the helicopter.
- The rotational speed of the rotor.
- The radial distance to the blade element.
- The azimuthal position of the rotor blade.
- The flapping angle and velocity.
- The blade twist.
- The angle of the rotor shaft.
- The gross weight of the helicopter.
- The flight altitude.

Figure 1 [Ref. 1] shows the angle of attack distribution for an example helicopter flying at 115 knots. It can be seen that the distribution is nonuniform and that the retreating blade experiences much larger values of angle of attack than the advancing blade. The angle of attack for a blade element may be simply approximated by a sinusoidal function of the form:

$$\alpha = \alpha_0 + \alpha_m \sin \psi$$

If the angle of attack on a retreating blade element becomes sufficiently high, the blade element stalls; however, the stall process and attendant force and moment behavior is quite different from the static stall associated with fixed-wing airfoils. Helicopter retreating blade stall is a dynamic phenomenon unique to unsteady flows; it is the primary limitation to the maximum velocity and high speed maneuverability of a helicopter in forward flight.

B. DYNAMIC LIFT/STALL

The advent of the helicopter led aerodynamicists to the discovery that airfoils undergoing rapid changes in angle of attack attain higher values of lift than static airfoils. This phenomenon was termed *dynamic lift*. Unfortunately, this increase in lift is usually followed by large excursions in lift, drag and pitching moment: similarly termed *dynamic stall*. The two terms are used almost interchangeably by aerodynamicists because the phenomena always accompany each other. The term most commonly used to describe the events that result in the dynamic delay of stall on airfoils undergoing unsteady motion is dynamic stall.

Experiments on oscillating airfoils have shown that the dynamic stall process is characterized by the formation, passage and subsequent shedding of a vortex. This dynamic stall vortex forms near the leading edge of an unsteady airfoil, passes downstream on the upper surface, and is shed into the wake.

The dynamic stall vortex induces a highly nonlinear, fluctuating pressure field. The aerodynamic forces and moments, that accompany the dynamic stall process, exhibit large amounts of hysteresis with respect to the instantaneous angle of attack, $\alpha(t)$, especially if α oscillates around some mean angle, α_0 , that is of the order of the static stall angle of attack, α_{ss} . [Ref. 2]

1. Dynamic Stall Events

Figure 2 [Ref. 3] shows the behavior of the normal (lift) force coefficient and pitching moment coefficient versus angle of attack for a NACA 0012 airfoil undergoing dynamic stall. The inset on the right side of the figure

depicts the dynamic stall events corresponding to points on the two graphs. While the actual behavior of the aerodynamic forces and moment are dependent upon many parameters, Figure 2 sufficiently demonstrates the force/moment trends of dynamic stall.

The sequential events which characterize the dynamic stall process (corresponding to Figure 2) are:

- 1) The upward pitching airfoil exceeds the static stall angle of attack with no discernable change in the flow over the airfoil.
- 2) Flow reversal in the boundary layer begins near the trailing edge of the airfoil, and progresses upstream on the surface of the airfoil.
- 3) Large eddies appear in the boundary layer.
- 4) Flow reversal spreads over much of the airfoil.
- 5) The pitching motion of the airfoil introduces vorticity into the flow, which coalesces near the leading edge, forming the dynamic stall vortex. The vortex grows and begins to move downstream over the upper surface of the airfoil.
- 6) The vortex continues to move downstream; the lift-curve slope increases dramatically.
- 7) The vortex movement induces a strong, negative pitching moment (moment stall). The lift continues to increase sharply.
- 8) Maximum lift is attained, followed by an abrupt, severe loss of lift.
- 9) Maximum negative moment occurs.
- 10) The vortex is shed into the wake; the airfoil is fully stalled.
- 11) Boundary layer reattachment begins at the leading edge and progresses downstream on the airfoil surface. Hysteresis in force/moment behavior is observed.
- 12) Flow reattachment is complete; lift and moment return to unstalled values.

McCroskey [Ref. 2] provides the following observations concerning the dynamic stall process:

- 1) As the dynamic stall vortex approaches the trailing edge, lift, moment and drag reach their largest values, although not simultaneously, and then drop dramatically.
- 2) Secondary and tertiary vortices produce additional fluctuations in the airloads, but at greatly reduced levels.
- 3) Flow reattachment occurs at an angle of attack much lower than the static stall angle of attack. The reattachment point moves rearward at a speed well below U_∞ , so that several chord lengths of travel are required before the flow completely returns to the approximately linear domain.

The convection speed at which the dynamic stall vortex moves downstream over the airfoil has been addressed in numerous investigations, and has been determined to have a value in the range of $.3 U_\infty$ to $.55 U_\infty$. [Refs. 2, 4, 5]

2. Stall Regimes

The instantaneous angle of attack for an airfoil undergoing sinusoidal motion is given by:

$$\alpha(t) = \alpha_0 + \alpha_m \sin(\omega t).$$

The maximum angle of attack attained during the oscillation cycle is the primary factor that influences the extent of flow separation on the unsteady airfoil; hence the dynamic stall regime encountered by the airfoil.

If α_{\max} is of the order of the static stall angle, the boundary layer thickens; however, almost no flow separation occurs. When α_{\max} is increased to values slightly above α_{ss} , a limited amount of separation occurs during a

small portion of the oscillation cycle; hysteresis is observed in the force/moment of the airfoil, but a negative pitching moment is not observed. This condition is indicative of stall onset.

Increasing α_{\max} to a value slightly above stall onset results in higher values of lift, accompanied by increased drag and a negative pitching moment with marked hysteresis during the downward half of the cycle. This is classified as the light stall regime.

Further increases in α_{\max} lead to deep dynamic stall, characterized by very large values of lift, drag and negative pitching moment, and the presence of significant hysteresis effects.

The effect of increasing α_{\max} can be seen in Figure 3 [Ref. 2] where $\alpha_m = 10^\circ$ and α_0 is varied from 3° to 10° for a NACA 0012 airfoil undergoing sinusoidal motion with a reduced frequency of $k = 0.10$.

Qualitatively, the stall regimes may be classified by the scale of viscous interaction, as depicted in Figure 4 [Ref. 6]. In light stall, the vertical extent of the viscous zone is on the order of the airfoil thickness. Deep stall is dominated by the vortex-shedding phenomenon and the scale of the viscous zone is on the order of the airfoil chord.

C. THESIS GOALS

A significant improvement in helicopter performance could be realized if it were possible to reap the benefits of dynamic lift without incurring the penalties associated with dynamic stall. This research was done as part of ongoing studies being conducted by Chandrasekhara and Carr [Ref. 4], with the ultimate goal of increased helicopter performance through control of dynamic stall. The knowledge gained through these efforts, however, will

have applications to all unsteady flow regimes, including supermaneuverable fighter and turbine aerodynamics.

This research involved the use of a unique facility, employing stroboscopic schlieren photography, to investigate and document the dynamic stall process. The specific areas of interest for this investigation were:

- 1) *Compressibility effects* — The effect of increased freestream Mach number was examined, with particular interest in shock development. Figure 5 [Ref. 4] shows that when the freestream Mach number exceeds about 0.2, the velocity near the leading edge of an oscillating airfoil becomes supersonic.
- 2) *Reduced frequency effects* — The effect of increasing the reduced frequency, k , was examined. The reduced frequency "is the portion of the oscillation cycle, in radians, which occurs during the time the air travels half of a chord length over the airfoil" [Ref. 1]; it is expressed as:

$$k = \frac{\omega c}{2U_{\infty}}$$

- 3) *Amplitude effects* — The effect of increasing the amplitude of oscillation for the angle of attack, α_m , while maintaining a constant mean angle of attack, α_0 , was examined.
- 4) *Dynamic stall vortex convection velocity, U_{DSV}* — The speed at which the dynamic stall vortex convects downstream over the upper surface of the airfoil was examined for comparison with the results of other studies.
- 5) *The reattachment process* — A cursory examination of the effects of parameter variation on the flow reattachment characteristics was conducted.

II. DESCRIPTION OF THE EXPERIMENT

A. FACILITY

The Compressible Dynamic Stall Facility (CDSF), located in the Fluid Mechanics Laboratory (FML) at the NASA Ames Research Center, was used to conduct an analysis of the dynamic stall on a harmonically oscillating airfoil. The CDSF is unique in that it permits visualization, and measurement, of the entire unsteady flowfield, at conditions which are representative of those experienced by a helicopter rotor blade in forward flight.

The CDSF consists of a wind tunnel, a stroboscopic schlieren system, a laser-Doppler velocimetry system, and associated hardware and instrumentation; the CDSF is shown in Figure 6 [Ref. 7].

1. Wind Tunnel

The FML has four tunnel bays which are centered on an in-draft, choked throat wind tunnel system. The system permits simultaneous experiments to be conducted utilizing one drive system. One of the tunnel bays houses the CDSF.

a. Drive System

A 240,000 cfm, 9,000 hp, fully automated centrifugal evacuation compressor drives the wind tunnel. The compressor is connected to the tunnel exit through a manifold, and maintains a vacuum pressure which is sufficient to cause sonic velocity at a throat immediately downstream of the test section. An electronic control panel, located at the rear of the test bay, is used to open/close a shutoff valve between the compressor and the tunnel. A second valve, which is manually operated, is located outside the FML. Control

automation is provided by a computer, located in the control bay, which monitors the operating conditions, and adjusts the guide vanes and bypass flow for efficient compressor operation.

b. Inflow Section

Atmospheric air is drawn through the bellmouth intake into the settling chamber which measures 49 cm wide by 59 cm high by 108 cm long. The settling chamber is constructed of 2.54 cm thick transparent Lucite.

Six fine mesh anti-turbulence screens are fitted into machined grooves in the walls of the settling chamber. Davis [Ref. 8] has reported the flow uniformity to be $\pm 0.25\%$ at 58 m/sec, with a turbulence intensity of 0.083% with a bandwidth of 50–50,000 Hz.

A 75 cm long contraction section leads to the test section. The contraction section is constructed of a 0.64 cm thick lead sheet enveloped by layers of fiberglass.

c. Test Section

The dimensions of the test section are 35 cm high by 25 cm wide by 100 cm long. Figures 7 and 8 [Ref. 7] are schematic diagrams of the test section as viewed from the side and upstream end, respectively.

The airfoil is a solid aluminum NACA 0012, with a chord of 7.62 cm. It is mounted spanwise between two D-shaped windows with a clearance of approximately 0.55 mm between the airfoil and the windows. Lateral impact loads are damped by thin, circular rubber cushions located between the airfoil and the windows. Tapered pins, located at $x/c = 0.25$ (the axis of rotation) and $x/c = 0.70$, are used to support the airfoil. The pins have spherical tips of 5.89 mm and 4.24 mm, respectively. The pins are push-fitted

into split plastic inserts, which are held together by bands and plastic tips. The pin assembly is push-fitted into delrin sleeves in the windows. The right side of Figure 9 [Ref. 7] shows the airfoil support structure.

The windows are schlieren quality, borosilicate glass (BK-7); they are 2.54 cm thick and have a diameter of 15.2 cm. They are supported by circular, magnesium frames which are mounted on bearing races to allow rotation of the windows. Sliding seals prevent the passage of ambient air into the test section.

Simultaneous oscillation of both windows is provided by flywheels, which are linked to the upstream portion of the window frames by connecting rods. The airfoil, in turn, experiences a sinusoidal oscillation of the form: $\alpha(t) = \alpha_0 + \alpha_m \sin(\omega t)$.

Eccentric disks are mounted flush with the flywheels and are coupled by a smaller shaft within the flywheel shaft. The drive disk is positioned to establish the oscillation amplitude for any half degree value between 2° and 10°.

The mean angle of attack of the airfoil is established by positioning of the indexing plates. The indexing plates are centered around the circular window frames on each side of the test section, and they support the flywheel assembly. The mean angle of attack is adjusted, for any value between 0° and 15°, by rotation and anchoring of the indexing plates.

A variable-speed AC motor (rated at 1 hp), connected to a belted pulley, drives the flywheel shaft. A potentiometer on the motor control box is used to adjust the motor speed. The motor is capable of imparting an

oscillation frequency of 100 Hz at maximum oscillation amplitude. The motor maintains a constant speed, to within 1%.

Additional details of the test section are provided by Sticht [Ref. 9], and Carr and Chandrasekhara [Ref. 7].

d. Tunnel Throat

A variable-area, sonic throat is located just downstream of the test section; the throat stabilizes the flow and is used to adjust the flow velocity through the test section. The throat consists of ramp-like plate assemblies which are mounted on the upper and lower tunnel walls. A DC motor (0.5 hp) is used to increase/decrease the throat height through a chain-driven gear system. A DC digital ammeter is incorporated to indicate throat height. The throat may be adjusted to yield a maximum freestream velocity of $M=0.5$.

2. Instrumentation

The wind tunnel is instrumented with 144 pressure ports. A scani-valve system, using a high resolution transducer, measures the pressures. The scani-valve reads six barrel ports; each port is connected to 24 pressure taps. The pressure information is automatically recorded using a Microvax II computer. A software program titled "FMDAS.LDV" incorporates the pressure inputs with a standard temperature to provide flow conditions, including freestream Mach number.

The test section is instrumented with two high resolution encoders to provide frequency and angle of attack information. An absolute encoder is mounted on the window frame and is geared to the indexing plate. This encoder measures the mean angle of attack with a resolution of 3,600 counts per cycle (0.1° per count).

An incremental, optical shaft encoder is linked to the flywheel shaft with a belted drive system. This encoder measures the frequency of oscillation and instantaneous phase count with a resolution of 200 counts per cycle.

Both encoders provide 16 bit, digital output data to a phase comparator. The phase comparator is used to pulse the strobe at the desired angle of attack. The phase comparator consists of internal counters and transparent latches. The oscillation frequency, mean phase angle, instantaneous phase angle and desired phase angle are digitally displayed. The desired phase angle is selected by sequencing a series of binary coded decimal (BCD) toggle switches. The phase comparator is interfaced with the strobe triggering mechanism; a push-button on the triggering mechanism is pressed and the strobe is pulsed at the desired phase angle. The instantaneous phase angle display freezes when the strobe is flashed; this permits verification that the flash angle matches the desired phase angle. A second button on the triggering mechanism is pressed to reset the instantaneous phase angle display.

A multiplexer interfaces the phase comparator with the Microvax II computer and enhances the resolution of the instantaneous phase count to 800 counts per cycle. The oscillation amplitude is input to the computer by the operator. The computer generates instantaneous angle of attack information based on the mean phase count, instantaneous phase count and oscillation amplitude.

3. Stroboscopic Schlieren System

Schlieren photography is an optical flow visualization technique that is used to establish an overall picture of an unsteady flowfield; thereby gaining insight to the qualitative aspect of the flow before embarking

on detailed quantitative investigations. Optical techniques are non-intrusive; they are advantageous over other visualization methods in that they do not require installation of a sensing device which might alter the flowfield.

The schlieren method uses the relationship between the gradients of density and optical index of refraction to produce an image of the density field in a transparent fluid. The schlieren technique is well suited to the analysis of dynamic stall on oscillating airfoils because, until deep stall occurs, the flow tends to remain two-dimensional. Goldstein [Ref. 10] provides an excellent review of the physical concepts of schlieren flow visualization and a description of the technique.

Stroboscopic schlieren photography provides an instantaneous picture of the unsteady flowfield because the density gradients are occurring at the instant the photograph is taken. The stroboscope is coupled to the motion of the window, so that the stroboscope is flashed when the airfoil is precisely at the specified angle of attack. The entire dynamic stall process is documented by sequentially taking photographs throughout the oscillation cycle.

The stroboscopic light source is a Type 3015 Strobrite, with a maximum intensity of 300×10^6 beam candles and a flashing rate of 1000 per second. A remote triggering device is pulsed once for single-exposure photographs or continuously for movies. The recycling circuitry is sufficiently responsive so as to permit studies at the highest frequency of interest.

An iris diaphragm is located 0.5 mm in front of the stroboscope to form a point source. The diaphragm location is coincident with the focal points of the stroboscope lens and a large spherical mirror. The mirror, which

measures 45 cm in diameter and has a 3m focal length, is located 3m from the test section. The mirror reflects light from the point source into the test section as a parallel cylinder of light.

A second spherical mirror, identical to the first, is located 3m from the other side of the test section. This mirror reflects the refracted light, which exits the test section, onto the vertical knife-edge (razor blade). The knife-edge is located at the focal point of the second mirror.

A lens is located behind the knife-edge to focus the light that passes the knife-edge. The lens is 5.4 cm in diameter is 1 cm thick; it has a focal length of approximately 600 mm.

A plane, circular mirror (10.5 cm diameter) directs the focused light to the photographic focal plane of the camera. This investigation involved the taking of single-exposure photographs using a galvanized photographic plate and Polaroid Type 52 film.

B. PROCEDURE

The eccentric disks and indexing plates were positioned to provide the desired oscillation characteristics. The throat height was adjusted, with the compressor operating and tunnel manifold open, to yield the desired freestream velocity. The AC motor speed was adjusted to set the desired oscillation frequency.

The image was viewed on the photographic plate (with no film installed) and the position of the knife-edge was adjusted, as necessary, to permit viewing of the flowfield around the airfoil and to enhance the contrast of the image. A visual inspection of the stall sequence was conducted to determine the range of phase angles that would allow tracking of the dynamic stall vortex development, passage and shedding. Additional phase angles were selected to complete the oscillation cycle, including the reattachment process.

The desired phase angle was input to the phase comparator and film was loaded onto the photographic plate. The strobe was triggered and the photograph was recovered. Verification was made to insure that the flash angle matched that of the desired phase angle. The next phase angle was input to the phase comparator and the instantaneous phase angle display was reset. The sequence was repeated until all desired phase angles were shot.

C. EXPERIMENTAL CONDITIONS

The indexing plates were positioned to give a mean angle of attack of 10° . The eccentric disks were positioned to give an oscillation amplitude of 5° . The airfoil, then, experienced sinusoidal motion of the form:

$$\alpha(t) = 10^\circ + 5^\circ \sin(\omega t).$$

The experiment was conducted for different configurations of freestream velocity and reduced frequency. The freestream velocity was varied from $M_\infty = 0.25$ to $M_\infty = 0.45$; the corresponding Reynolds number variation was $Re = 450,000$ to $Re = 810,000$. The reduced frequency was varied from $k = 0.025$ to $k = 0.10$. Table I shows the specific conditions of the tests.

TABLE I. EXPERIMENTAL CONDITIONS
 $\alpha(t) = 10^\circ + 5^\circ \sin(\omega t)$

M	k			
	0.025	0.050	0.075	0.10
0.25	X	X	X	X
0.30	X	X	X	X
0.35	X	X	X	X
0.40	X	X	X	
0.45	X	X	X	

X: tested configuration

III. RESULTS AND DISCUSSION

A. STROBOSCOPIC SCHLIEREN ANALYSIS

Figures 10–27 show the transition to dynamic stall for each test configuration. Each figure is a series of schlieren photographs taken at progressively increasing angles of attack during the upstroke portion of the oscillation cycle. The knife-edge was oriented such that positive density gradients appear dark in the photographs. The formation of the dynamic stall vortex, its passage along the airfoil upper surface and subsequent shedding into the wake, are clearly visible in each of these figures. It is sometimes difficult to determine the exact location of the dynamic stall vortex in the photographs, because of the relatively large region of density gradient. In these instances, the vortex location was interpreted to be the center on the strong density gradient region; this introduces a degree of subjectivity into the results.

It must be noted that the thin streaks which are perpendicular to the airfoil on the upper and lower surfaces, at the 70% chord position, are due to cracks in the glass window. These cracks occurred when the airfoil support pins were being push-fitted into the windows during earlier work by Chandrasekhara and Carr [Ref. 4]. The cracks have not propagated through continued use of the CDSF and do not affect the flow in the test section.

Also, in some of the figures, streaks are present which coincide with the streamlines of the sidewall flow. The streaks were caused by a seepage of oil from the window seal. It was determined that this did not affect the investigation as there was no leakage of airflow into the tunnel through the seals. The seepage condition was remedied by installing tape over the affected

portion of the seal. These streaks clearly demonstrate that the airfoil flow, and the schlieren photographs, were not affected by the airfoil/window junction flow, thus establishing the two-dimensionality of the dynamic stall flow.

The following observations can be made from Figures 10-27:

- (1) The dark area on the lower surface of the airfoil leading edge is due to the strong density gradient associated with the flow stagnation region.
- (2) The white patch on the upper surface of the leading edge indicates the leading edge suction, induced by flow acceleration over the leading edge of the airfoil. This is an area of decreasing pressure (negative density gradient).
- (3) The dark, bubble-like area immediately downstream of the white patch, at the lower angles of attack, is a region of positive density gradient (adverse pressure gradient) which accompanies the flow deceleration. This region contains the vorticity that is generated due to the pitching motion of the airfoil.
- (4) As the angle of attack is increased, the region of vorticity is seen to grow. The vorticity coalesces to form the dynamic stall vortex. This usually occurs at about the 20% chord point on the airfoil. The formation of the vortex is accompanied by considerable thickening of the boundary layer. The airfoil experiences leading edge stall, which is indicated by the white streak originating at the leading edge. By the time the dynamic stall vortex has fully formed, and leading edge stall occurs, the generation of useful vorticity has ceased. [Ref. 4]
- (5) The dynamic stall vortex penetrates the shear layer and convects downstream over the upper surface of the airfoil as the angle of attack is further increased. The dynamic stall vortex is indicated by the dark region within the viscous zone.
- (6) At the higher angles of attack, the dynamic stall vortex is seen to lift off the surface of the airfoil and is eventually shed into the wake. The airfoil experiences deep dynamic stall when the vortex is released from the airfoil surface or convects past the trailing edge. Deep dynamic stall is indicated by the presence of a fully separated shear layer, where density gradients are relatively small.

The airfoil generates lift as long as the dynamic stall vortex remains on the surface [Ref. 11]. Understanding the fluid flow physics resulting in

dynamic stall vortex formation, in response to degree of unsteadiness, is the essential first step toward the eventual control of dynamic stall.

An interesting observation was made for the conditions: $M = 0.40$ and $k = 0.025$ (Figure 22). Acoustic waves, strong enough to be seen in the schlieren photographs, are present in the angle of attack range from $\alpha = 10.0^\circ$ to $\alpha = 10.8^\circ$. The acoustic waves, which are simply alternating zones of high and low density air, are seen to propagate upstream from the leading edge in a circular pattern; they have no apparent effect on the flow over the airfoil, or on the dynamic stall process. The fact that they are clearly visible also shows that the waves are, indeed, cylindrical; they are approximately centered around the vortex.

B. COMPRESSIBILITY EFFECTS

The airfoil experienced deep dynamic stall for all conditions tested. No shocks were observed; however, compressibility was seen to significantly influence the behavior of the dynamic stall vortex. Due to the nature of the investigation, the dependence of the compressibility effects, on Mach number and Reynolds number variation, could not be ascertained. It is believed that the compressibility effects are dominated by variation of the freestream velocity; however, studies should be conducted to determine the influence of Mach number and Reynolds number variation, independently.

The effects of compressibility, on the transition to dynamic stall, are shown in Figure 28 for reduced frequencies of $k = 0.025, 0.050, 0.075$ and 0.10 . In the figure, the location of the dynamic stall vortex on the airfoil (x/c) is plotted against the airfoil angle of attack (α) for each of the Mach numbers tested. It should be noted that the center of the vorticity region was plotted

for the lower angles of attack, before the dynamic stall vortex was fully formed.

The behavior of the dynamic stall vortex was observed to be quite similar for the conditions of $M_\infty = 0.25$ and $M_\infty = 0.30$; however, a marked difference in the vortex behavior was noted when the freestream Mach number exceeded 0.30.

In Figure 28, the formation of the dynamic stall vortex is indicated by the point where the slope of each curve changes significantly. It is readily observed that increasing the freestream Mach number caused the dynamic stall vortex to form at progressively lower angles of attack; this is not unexpected, as the static stall angle decreases with increasing Mach number. The chordwise location at which the dynamic stall vortex formed on the airfoil, however, was consistent (within experimental scatter) until the freestream Mach number reached 0.35. When $M_\infty > 0.35$, the dynamic stall vortex was observed to form further downstream from the leading edge. The angles of attack and chordwise locations, corresponding to formation of the dynamic stall vortex for the conditions tested, are summarized in Tables II and III, respectively.

The airfoil was observed to experience deep dynamic stall at lower angles of attack as the freestream Mach number was increased (especially when $M_\infty > 0.30$). This effect may be directly related to the fact that the dynamic stall vortex forms at lower angles of attack with increasing Mach number. When the dynamic stall vortex forms at lower angles of attack, the airfoil motion has imparted less vorticity to the flow; and thus, the vortex that forms tends to be weaker. This decreased strength of the dynamic stall

TABLE II. VORTEX FORMATION ANGLES OF ATTACK

$$\alpha(t) = 10^\circ + 5^\circ \sin(\omega t)$$

M	k			
	0.025	0.050	0.075	0.10
0.25	12.4	12.6	12.9	13.3
0.30	12.3	12.6	12.3	13.3
0.35	11.2	11.2	11.6	11.9
0.40	11.0	10.8	11.2	X
0.45	10.1	10.4	10.8	X

X: not tested

TABLE III. VORTEX FORMATION LOCATIONS

$$\alpha(t) = 10^\circ + 5^\circ \sin(\omega t)$$

M	k			
	0.025	0.050	0.075	0.10
0.25	.12	.13	.15	.16
0.30	.13	.16	.12	.18
0.35	.14	.12	.15	.15
0.40	.19	.18	.21	X
0.45	.26	.24	.24	X

X: not tested

vortex, at higher Mach numbers, results in the vortex being shed into the wake at a lower angle of attack.

Table IV shows the angles of attack at which the dynamic stall vortex convected past the trailing edge, or was released into the wake, for the conditions of the experiment. The vortex release angles of attack were obtained from the schlieren photographs, and should be considered accurate to within about 0.1° due to the resolution of the phase angles selected to document the dynamic stall process.

TABLE IV. VORTEX RELEASE ANGLES OF ATTACK
 $\alpha(t) = 10^\circ + 5^\circ \sin(\omega t)$

M	k			
	0.025	0.050	0.075	0.10
0.25	13.7	13.9	14.4	14.7
0.30	13.3	14.1	14.3	14.6
0.35	12.3	12.9	13.8	14.1
0.40	11.9	12.3	12.9	X
0.45	11.2	11.9	12.6	X

X: not tested

C. REDUCED FREQUENCY EFFECTS

Figure 29 contains plots of the chordwise location of the dynamic stall vortex versus airfoil angle of attack for freestream Mach numbers of $M_\infty = 0.25, 0.30, 0.35, 0.40$ and 0.45 . These plots show the effect of reduced frequency variation on the transition to dynamic stall.

The dominant effect of increasing the reduced frequency was to cause the dynamic stall vortex to remain on the surface of the airfoil to a higher angle of attack (see Table IV), thereby delaying the effects of dynamic stall. This trend was observed for all Mach numbers studied. This effect suggests that increasing the oscillation frequency, in and of itself, may be a viable method of controlling dynamic stall, if the induced adverse pitching moment is not too severe.

Table II shows that, for most cases observed, increasing the reduced frequency delayed the inception of the vortex to a slightly higher angle of attack. This delay results in the formation of a stronger vortex; which is necessary to sustain the larger adverse pressure gradients induced by the increased pitch rate of the airfoil.

Chandrasekhara and Carr [Ref. 4] observed that increasing the reduced frequency caused the dynamic stall vortex to form closer to the leading edge of the airfoil (for compressible flows). This effect, however, was not observed in the present investigation. This apparent discrepancy is probably due to the following factors:

- (1) The net vorticity input is considerably less at 5° amplitude, with the result that consolidation into a discrete vortex may occur later in the oscillation cycle.
- (2) The resolution of the phase counts (angles of attack) which were selected for photographs, affects the determination of the location at which the vortex forms. The degree of uncertainty, in this determination, depends upon the difference in phase count between the two successive photographs that define the change in the slope of the curves in Figures 28-36.

D. AMPLITUDE EFFECTS

The behavior of the dynamic stall vortex, observed in this investigation, was compared to that observed by Chandrasekhara and Carr [Ref. 4] in order to gain insight into the effects of oscillation amplitude on dynamic stall. The airfoil motion examined by Chandrasekhara and Carr was:

$$\alpha(t) = 10^\circ + 10^\circ \sin(\omega t).$$

Figures 30–34 show the amplitude effects on the transition to dynamic stall for freestream Mach numbers of $M_\infty = 0.25, 0.30, 0.35, 0.40$ and 0.45 , respectively. In these figures, the chordwise location of the vortex is plotted against the angle of attack of the airfoil for the commonly examined reduced frequencies.

Tables V and VI summarize the angles of attack and chordwise locations, respectively, corresponding to formation of the dynamic stall vortex for an oscillation amplitude of 10° . Table VII shows the vortex release angles of attack observed by Chandrasekhara and Carr ($\alpha_m = 10^\circ$).

TABLE V. VORTEX FORMATION ANGLES OF ATTACK
 $\alpha(t) = 10^\circ + 10^\circ \sin(\omega t)$

M	k			
	0.025	0.050	0.075	0.10
0.25	13.1	13.8	14.5	13.1
0.30	13.1	13.1	13.8	14.5
0.35	12.3	12.3	12.3	X
0.40	11.4	10.8	X	X
0.45	10.8	11.2	X	X

X: not tested

TABLE VI. VORTEX FORMATION LOCATIONS

$$\alpha(t) = 10^\circ + 10^\circ \sin(\omega t)$$

M	k			
	0.025	0.050	0.075	0.10
0.25	.14	.14	.16	.08
0.30	.16	.07	.12	.12
0.35	.25	.14	.07	X
0.40	.26	.16	X	X
0.45	.26	.16	X	X

X: not tested

TABLE VII. VORTEX RELEASE ANGLES OF ATTACK

$$\alpha(t) = 10^\circ + 10^\circ \sin(\omega t)$$

M	k			
	0.025	0.050	0.075	0.10
0.25	14.5	15.9	17.1	18.1
0.30	14.1	15.9	17.6	18.1
0.35	13.8	15.2	15.9	X
0.40	13.1	14.5	X	X
0.45	12.3	14.2	X	X

X: not tested

McCroskey [Ref. 2] and Carr [Ref. 3] note that varying the oscillation amplitude affects dynamic stall in a manner similar to frequency variation. This effect was substantiated in the present investigation; variation of the oscillation amplitude was observed to influence the behavior of the dynamic

stall vortex in a manner opposite to that produced by variation of the freestream Mach number.

Increasing α_m generally caused the vortex formation to occur at a slightly higher angle of attack; no conclusions can be made as to the effect on the location of the vortex formation. The vortex was released from the airfoil at a substantially higher angle of attack when the oscillation amplitude was increased; this effect was especially pronounced at the higher values of reduced frequency. This demonstrates that the vortex behavior is strongly dependent upon the pitch rate of the airfoil. A similar observation was made by McCroskey et al [Ref. 12].

The adverse pressure gradients induced by increasing α_m to 10° are larger than that for the case of $\alpha_m = 5^\circ$. It may seem surprising, then, that the vortex is able to sustain the strong pressure gradients and remain on the surface of the airfoil to higher angles of attack. Reynolds and Carr [Ref. 13], however, have shown that the surface acceleration and pressure gradient near the leading edge generate the vorticity which evolves into the dynamic stall vortex. The vorticity induced by the airfoil motion, is larger for the higher oscillation amplitude; thus, the vortex that forms tends to be stronger.

It appears that the vortex formation process may be the dominating factor in the delay of dynamic stall. This area requires further study; a detailed examination of activity at the leading edge should lead to a better understanding of the vortex formation process.

E. CONVECTION VELOCITY OF THE DYNAMIC STALL VORTEX

The convection velocity of the dynamic stall vortex, U_{DSV} , was determined by measuring the location of the vortex for any two consecutive phase

angles and dividing the chordwise distance travelled by the time difference for the two phase angles. Figures 35–39 are plots of the vortex convection velocity (normalized with the freestream velocity) versus the chordwise location of the vortex, for Mach numbers of $M = 0.25, 0.30, 0.35, 0.40$ and 0.45 , respectively. Each of these figures contains plots for the reduced frequencies that were examined.

The trend of each plot is consistent; three stages were observed, with regard to the convection velocity, in the behavior of the dynamic stall vortex. The first stage corresponds to the formation of the dynamic stall vortex, and the convection velocity is near zero. Vorticity is generated during this stage and coalesces to form the vortex.

In the second stage, the vortex gathers strength and acts upon the adverse pressure gradient downstream of the suction peak. The convection velocity steadily increases as the vortex sustains the increasing pressure.

The outer flow forces overcome the inner, viscous flow resistance in the last stage. The vortex breaks away from the surface and penetrates the viscous zone, disturbing the potential flow. The vortex convects downstream, within the shear layer, at a near constant velocity. [Ref. 13]

Chandrasekhara and Carr [Ref. 4] determined the vortex convection velocity, in the third stage, to be $0.3 U_{\infty}$. Figures 35–39 show that this is a reasonable estimation. Some of the plots indicate a lower value for U_{DSV} , and there is some extent of scatter in the data (particularly in the third stage). This may be attributed to the following points:

- (1) The determination of the vortex location was somewhat subjective.

- (2) Only the velocity in the chordwise direction was considered; the velocity of the vortex, normal to the airfoil, was neglected. The normal velocity, in some cases, was large, depending on the vortex strength.

F. REATTACHMENT

Figures 40–57 show the flow reattachment process for each of the test conditions. Each figure is a sequence of schlieren photographs taken at progressively decreasing angles of attack during the downstroke. The reattachment point is quite discernable in the photographs, as the process occurs rearward from the leading edge.

The examination of the reattachment process was cursory in nature; as such, only a few phase angles were photographed for each test configuration. Completion of the reattachment was not documented for some of the test conditions.

An interesting observation was noted for the conditions: $M = 0.45$ and $k = 0.050$ (Figure 56). Here, the flow reattachment point was observed to move back upstream as the airfoil pitched downward from $\alpha = 10.4^\circ$ to $\alpha = 10.0^\circ$. The reason for this is not known; it may be a response to a possible presence of a shock or separation bubble, or merely a transient effect occurring because the photographs were taken during different cycles of oscillation. The resolution between the phase angles needs to be improved and a detailed investigation should begin earlier in the downstroke.

Figures 58 and 59 show the effects of compressibility and reduced frequency, respectively, on the reattachment process. Each figure contains plots of the chordwise location of the reattachment point versus the angle of attack for the airfoil. The lack of sufficient data points renders it impossible to make

any definitive statements about the response of the reattachment process to variations in the freestream Mach number and reduced frequency; however, noticeable trends can still be seen in the two figures.

Increasing the freestream velocity delayed the flow reattachment to lower angles of attack. This is a logical effect because the static stall angle varies inversely with the freestream velocity; however, this effect was negated as the reduced frequency was increased.

Similarly, a delay in the reattachment process was observed as the reduced frequency was increased; this effect was reduced for increased values of freestream Mach number. The effect of reduced frequency on reattachment is surprising, because it would be expected that reattachment would occur in a manner that somewhat mirrors the stall process. Herring et al [Ref. 14] observed similar results during ramp down tests on a family of NACA 23012 airfoils.

IV. CONCLUSIONS AND RECOMMENDATIONS

A. CONCLUSIONS

- (1) The airfoil experienced deep dynamic stall for all conditions tested, indicating that a maximum angle of attack of 15° is sufficient to cause formation of the dynamic stall vortex. The formation of the vortex and its subsequent behavior, however, strongly depend on the parameters of compressibility, reduced frequency and oscillation amplitude.
- (2) Although no shocks were observed, compressibility effects are significant when the freestream Mach number exceeds 0.3. The dynamic stall vortex forms, and is released from the airfoil, at lower angles of attack as the Mach number is increased.
- (3) The dynamic stall process is delayed by increasing the reduced frequency. The vortex forms at slightly higher angles of attack, and is released at substantially higher angles of attack, for progressively increasing values of oscillation frequency.
- (4) Oscillation amplitude effects dynamic stall in a manner similar to the reduced frequency. The combination of increased amplitude and frequency significantly delays the effects of dynamic stall, indicating the importance of pitch rate.
- (5) The dynamic stall vortex convects at a near constant velocity of approximately $0.3 U_\infty$.
- (6) Both the freestream Mach number and the reduced frequency impact on the reattachment process. Increasing either parameter delays the flow reattachment; however, when either parameter is sufficiently high, the reattachment process stabilizes and is not affected by variation of the other parameter.

B. RECOMMENDATIONS

- (1) The resolution of the phase angles selected needs to be improved to obtain more accurate data on the vortex formation and shedding angles of attack and locations.

- (2) A detailed investigation should be conducted to ascertain the details of the vortex formation process near the leading edge. This phenomenon is not well understood, and it seems to be the key factor in determining the character of dynamic stall.
- (3) Studies should be conducted, using airfoils of varying chord lengths, to delineate the effects of Mach number and Reynolds number on the dynamic stall process.
- (4) A similar investigation should be conducted for the case of $\alpha_m = 2^\circ$, so as to validate the observations made for the amplitude effects. In this configuration, the airfoil may only experience deep dynamic stall for high values of freestream velocity, if at all. Such an investigation should include combinations of amplitude and frequency which provide matched pitch rates to determine if the effects are indeed a response to amplitude variation or, rather, to pitch rate variation.

APPENDIX A. NOMENCLATURE

The terms used within this presentation are explained below:

Symbol	Definition	Units
A_1	First lateral harmonic of blade feathering	deg
B_1	First longitudinal coefficient of blade flapping	deg
C_T	Coefficient of thrust	
c	Airfoil chord	cm
k	Reduced frequency	rad
M	Mach number	
Re	Reynolds number	
t	Time	sec
U	Velocity	m/sec
x	Location of airfoil	cm
α	Angle of attack	deg
μ	Advance ratio	
ω	Circular frequency	rad/sec
ψ	Azimuthal position of rotor blade	deg
σ	Solidity	
θ	Pitch setting	deg

Subscripts	Definition
DSV	Dynamic stall vortex
m	Maximum oscillation amplitude
max	Maximum value
ss	Static stall
TPP	Tip path plane
0	Mean value
∞	Freestream condition

APPENDIX B **FIGURES**

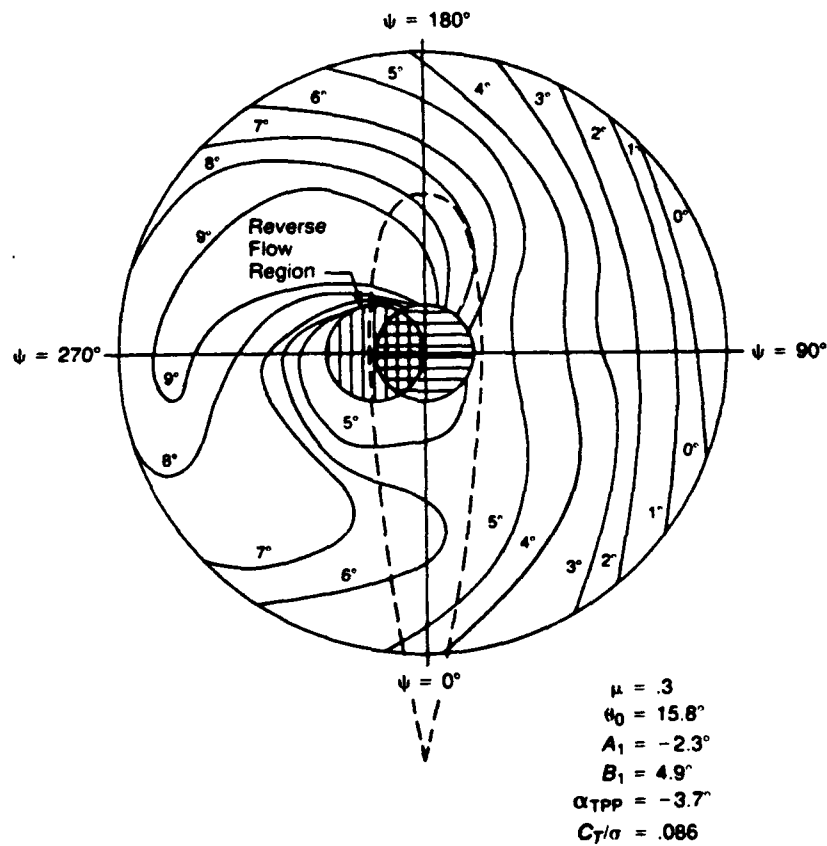


Figure 1. Angle of Attack Distribution for Example Helicopter

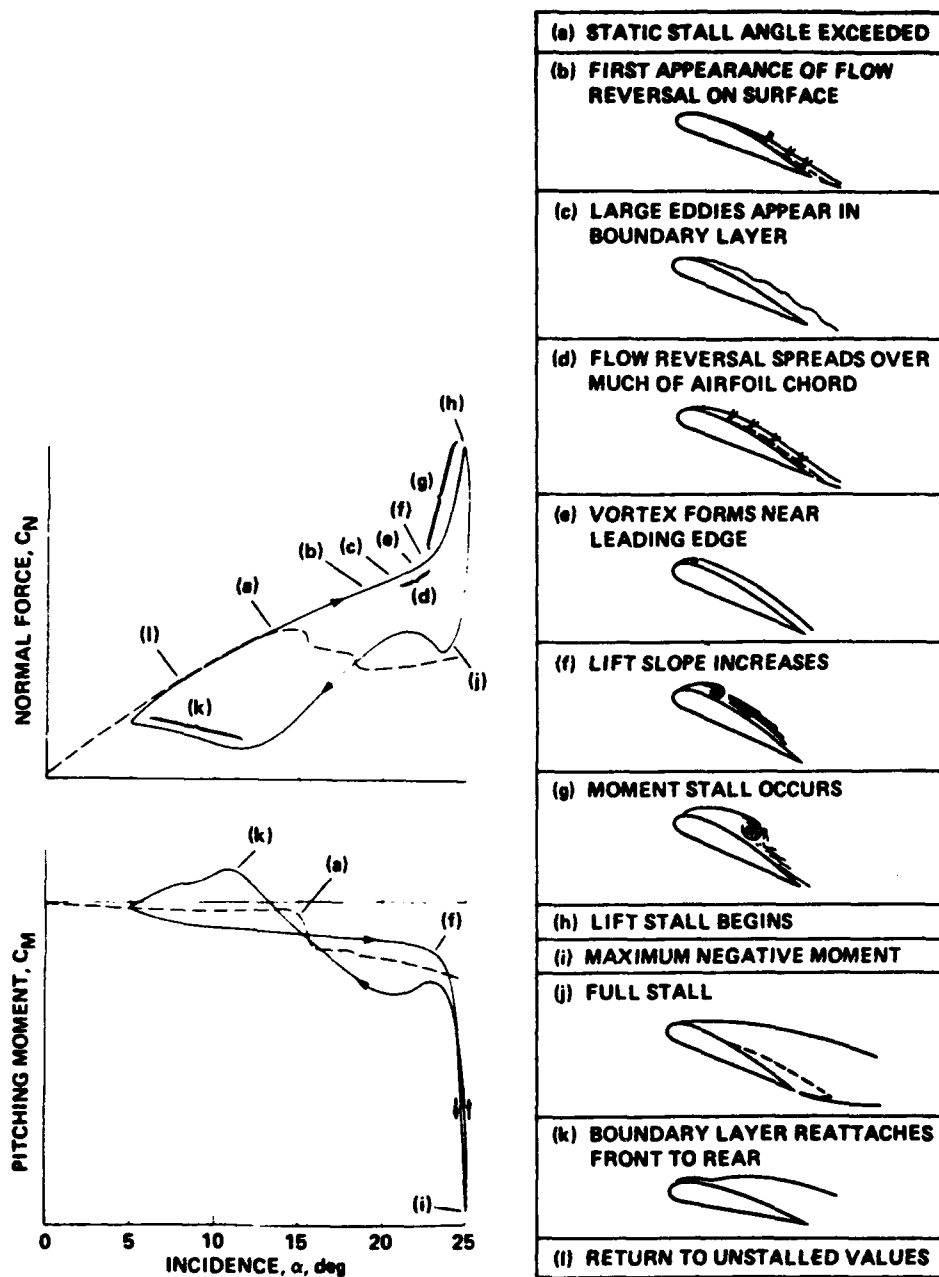


Figure 2. Events of Dynamic Stall on NACA 0012 Airfoil

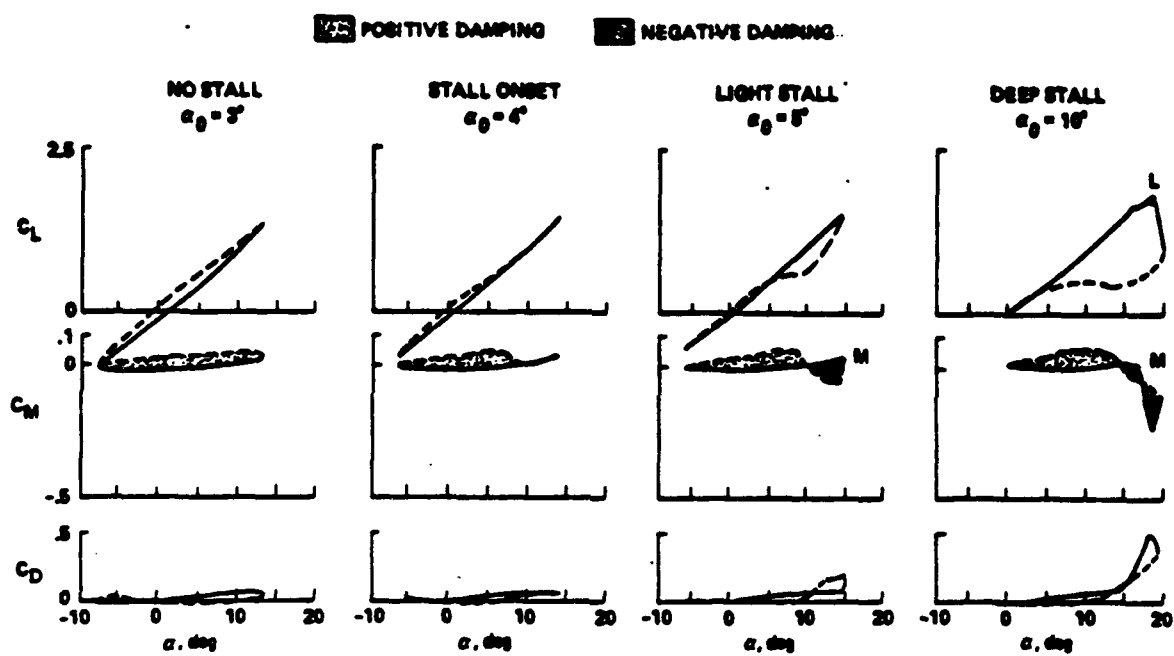


Figure 3. Dynamic Stall Regimes

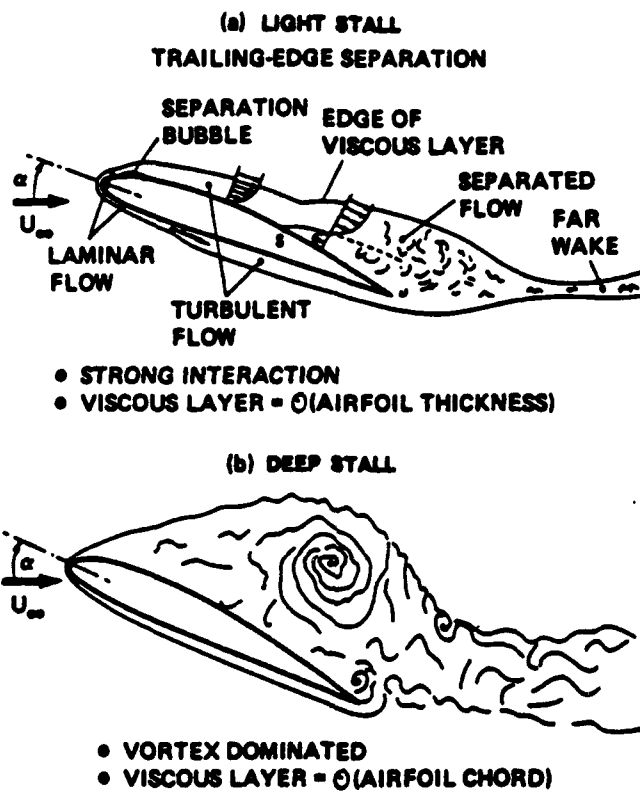


Figure 4. Viscous Interaction During Dynamic Stall

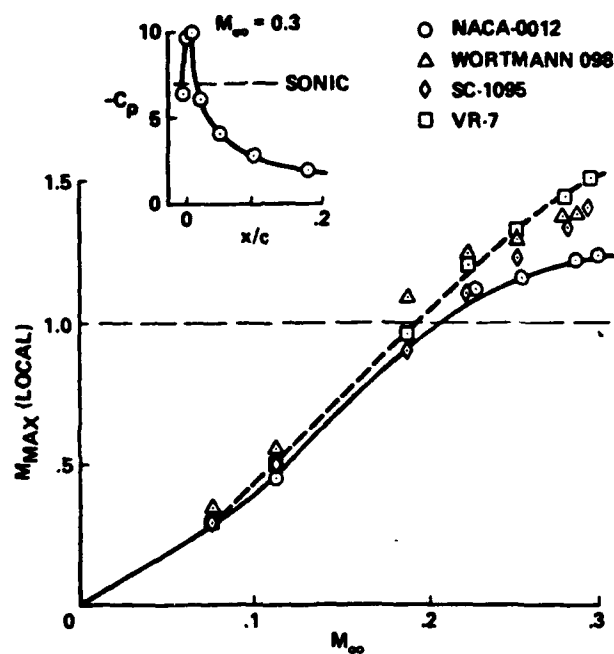


Figure 5. Local Mach Number on Leading Edge of an Oscillating Airfoil vs. Freestream Mach Number

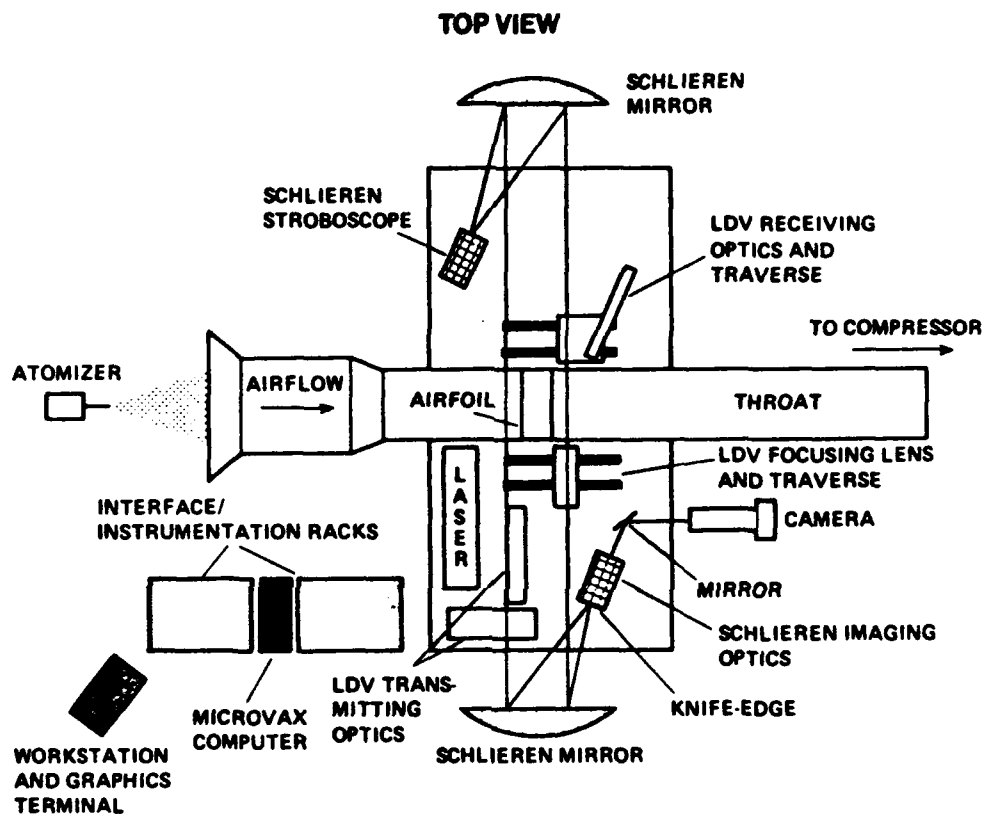


Figure 6. Schematic of the Compressible Dynamic Stall Facility

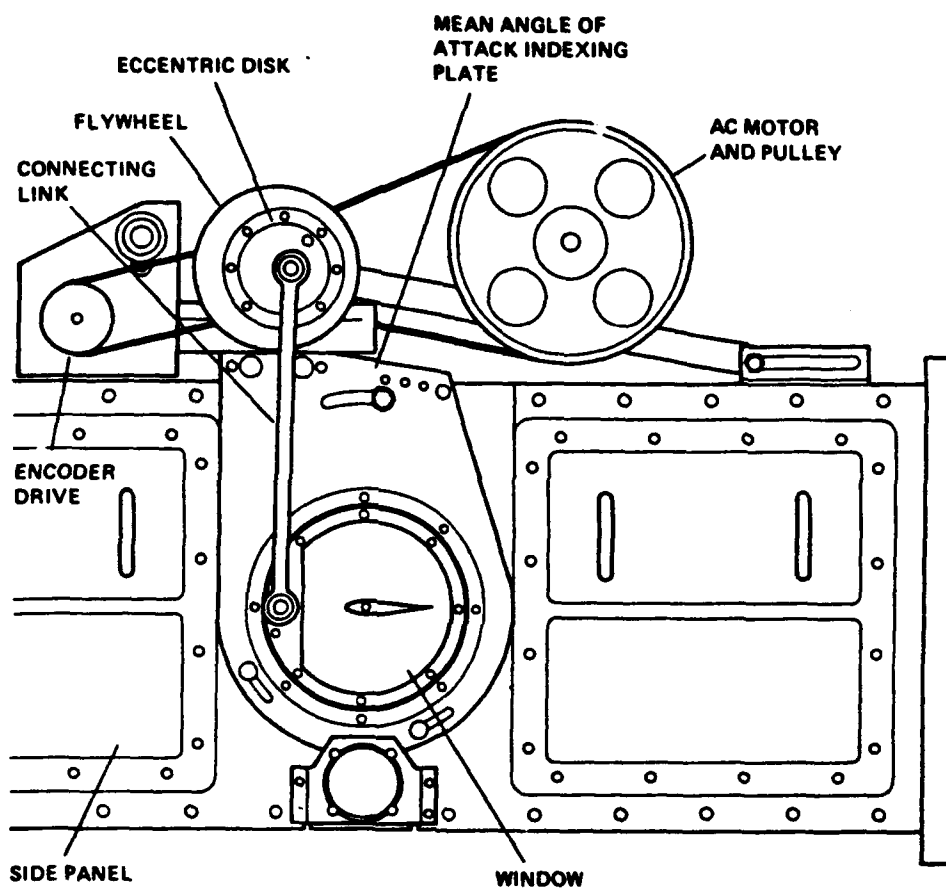


Figure 7. Side View of the Test Section

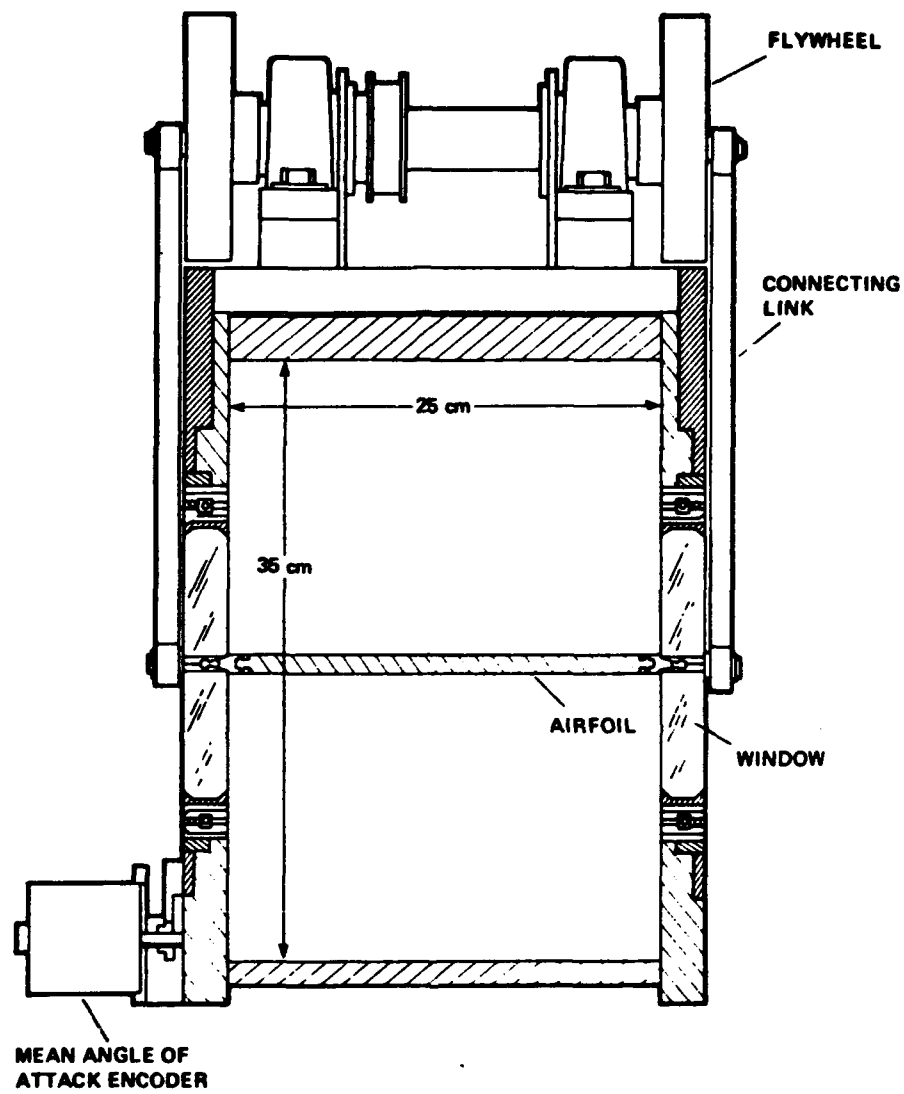


Figure 8. End View of the Test Section

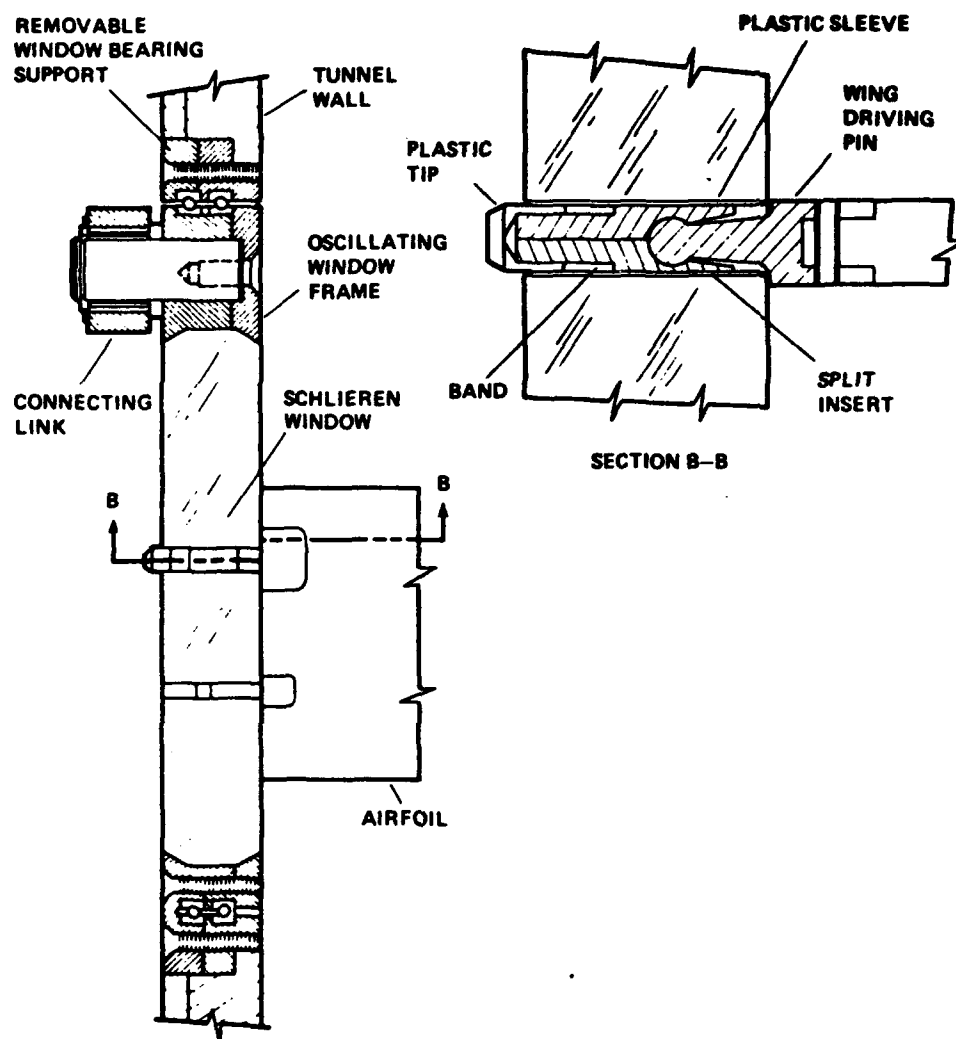


Figure 9. Airfoil Support Structure

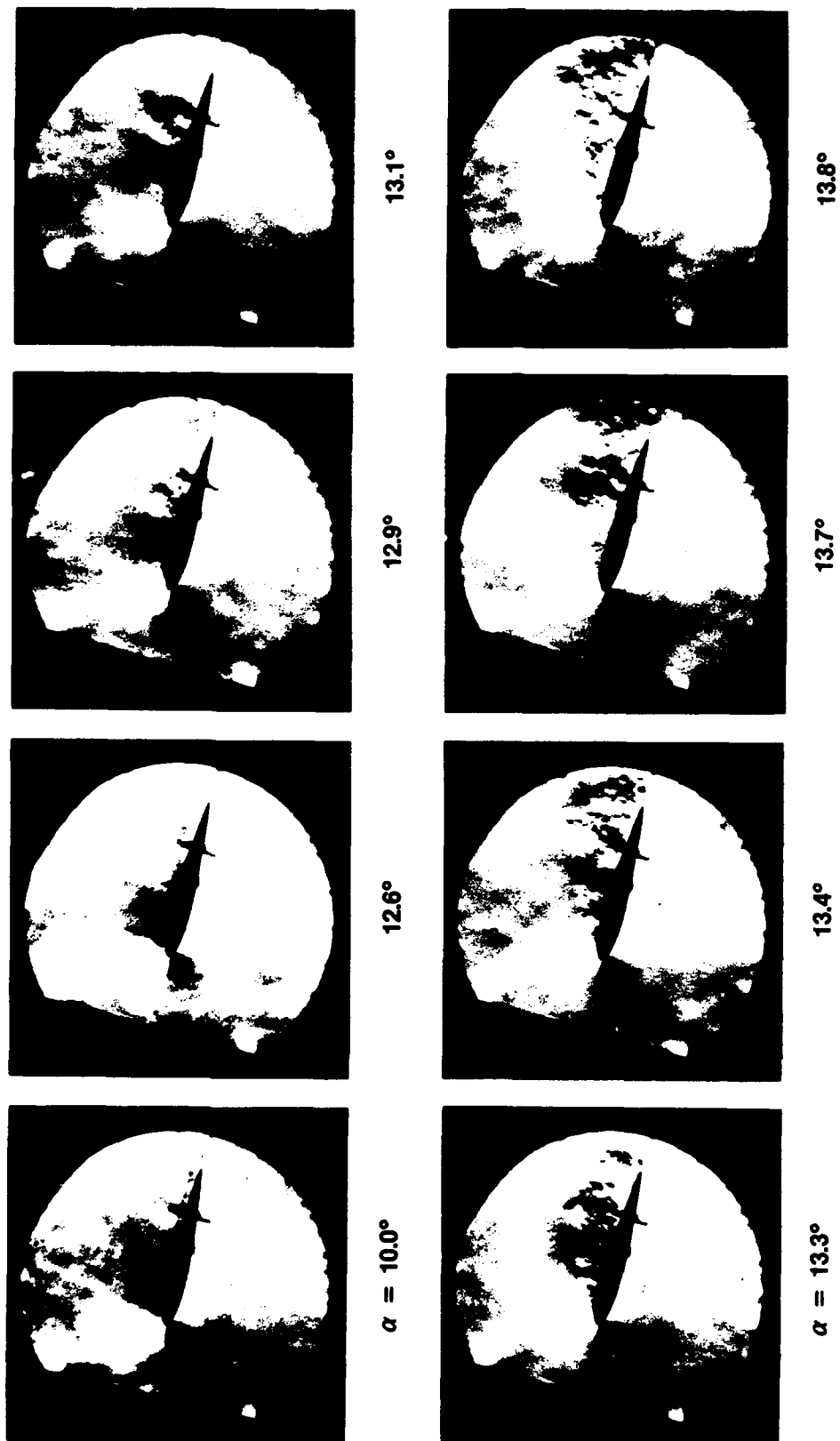


Figure 10. Transition to Stall; $M_\infty = 0.25$, $Re = 450,000$, $k = 0.025$

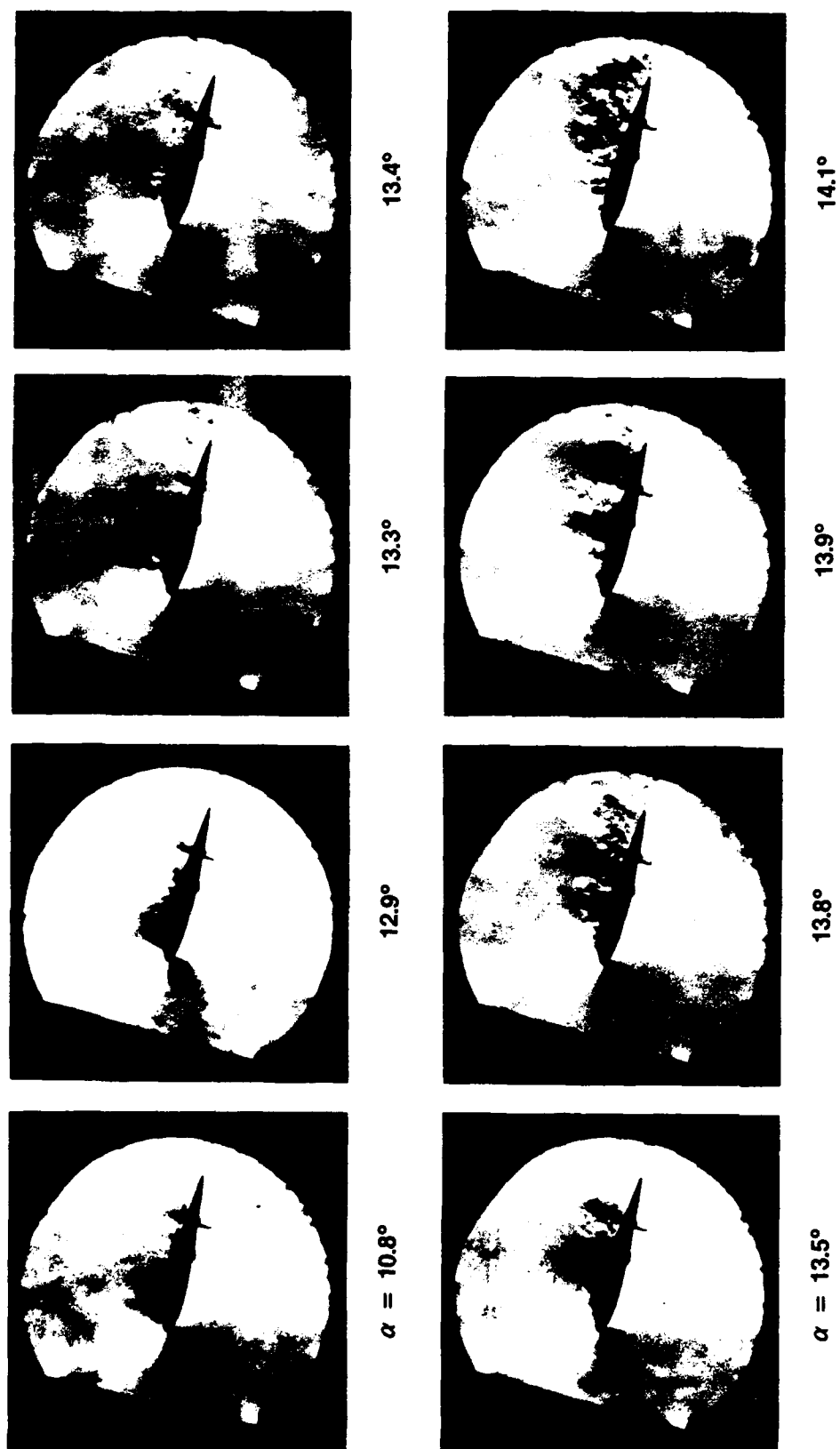


Figure 11. Transition to Stall; $M_\infty = 0.25$, $Re = 450,000$, $k = 0.050$



13.8°



13.5°



13.3°



$\alpha = 10.0^\circ$



14.6°



14.5°



14.4°



$\alpha = 14.1^\circ$

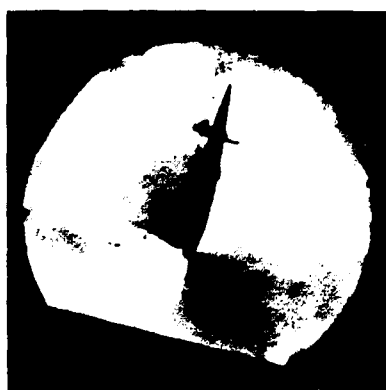
Figure 12. Transition to Stall; $M_\infty = 0.25$, $Re = 450,000$, $k = 0.075$



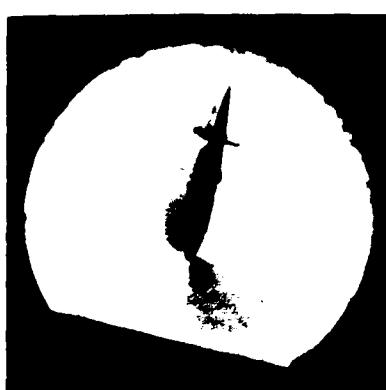
$\alpha = 10.8^\circ$



12.9°



13.5°



14.1°



$\alpha = 14.3^\circ$



14.5°



14.7°



14.8°

Figure 13. Transition to Stall; $M_\infty = 0.25$, $Re = 450,000$, $k = 0.10$

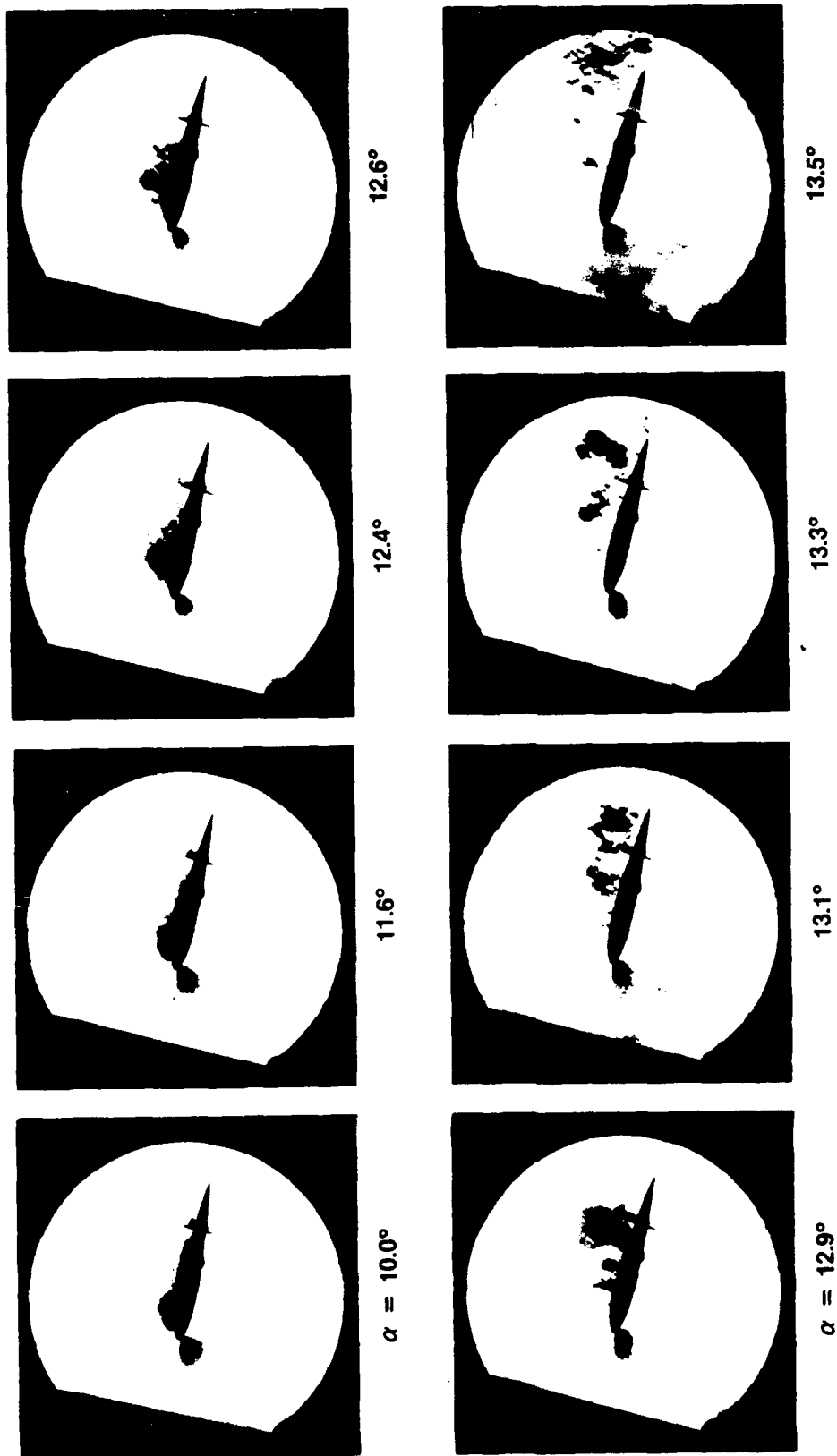


Figure 14. Transition to Stall; $M_\infty = 0.30$, $Re = 540,000$, $k = 0.025$

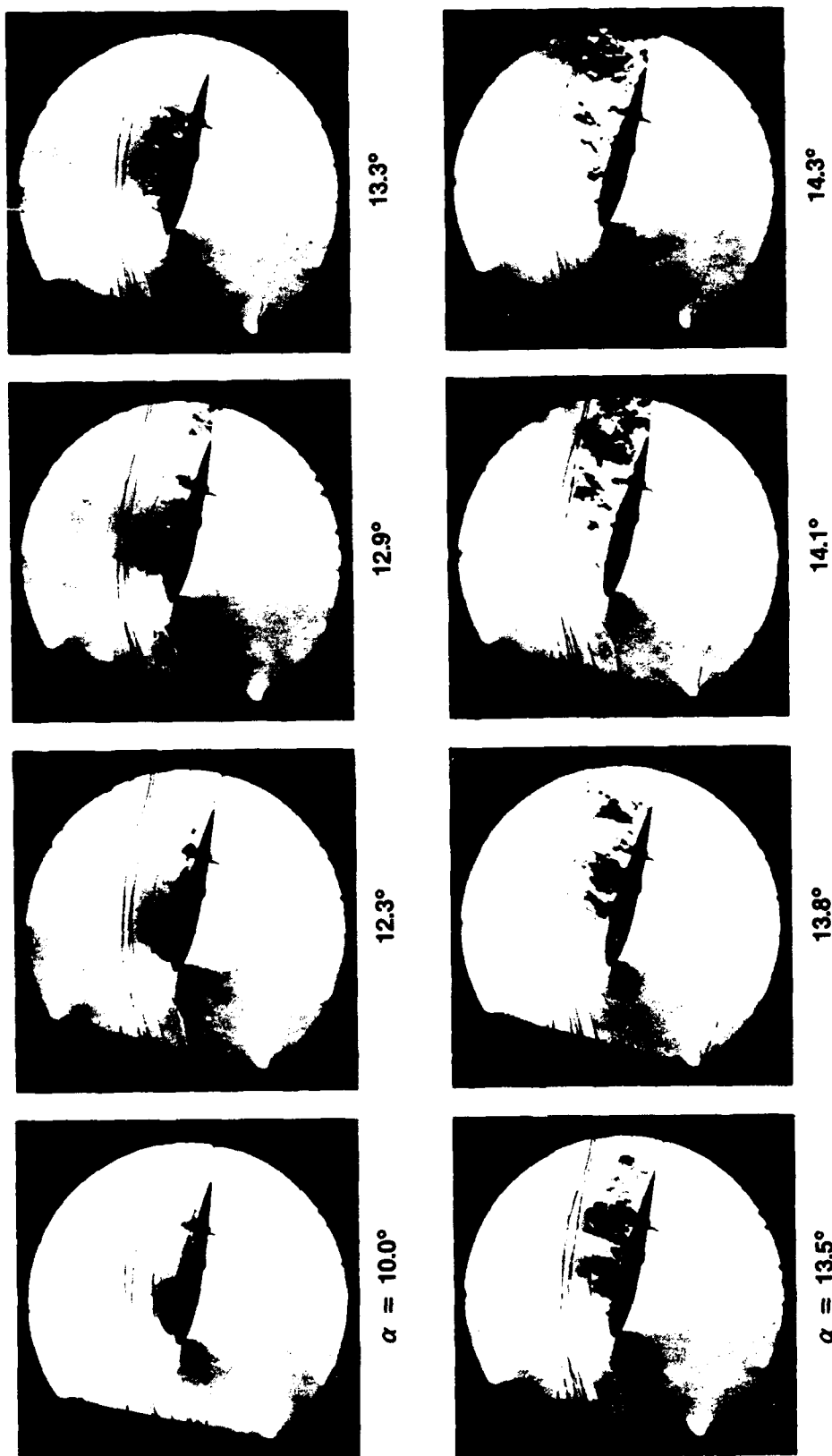


Figure 15. Transition to Stall; $M_\infty = 0.30$, $Re = 540,000$, $k = 0.050$

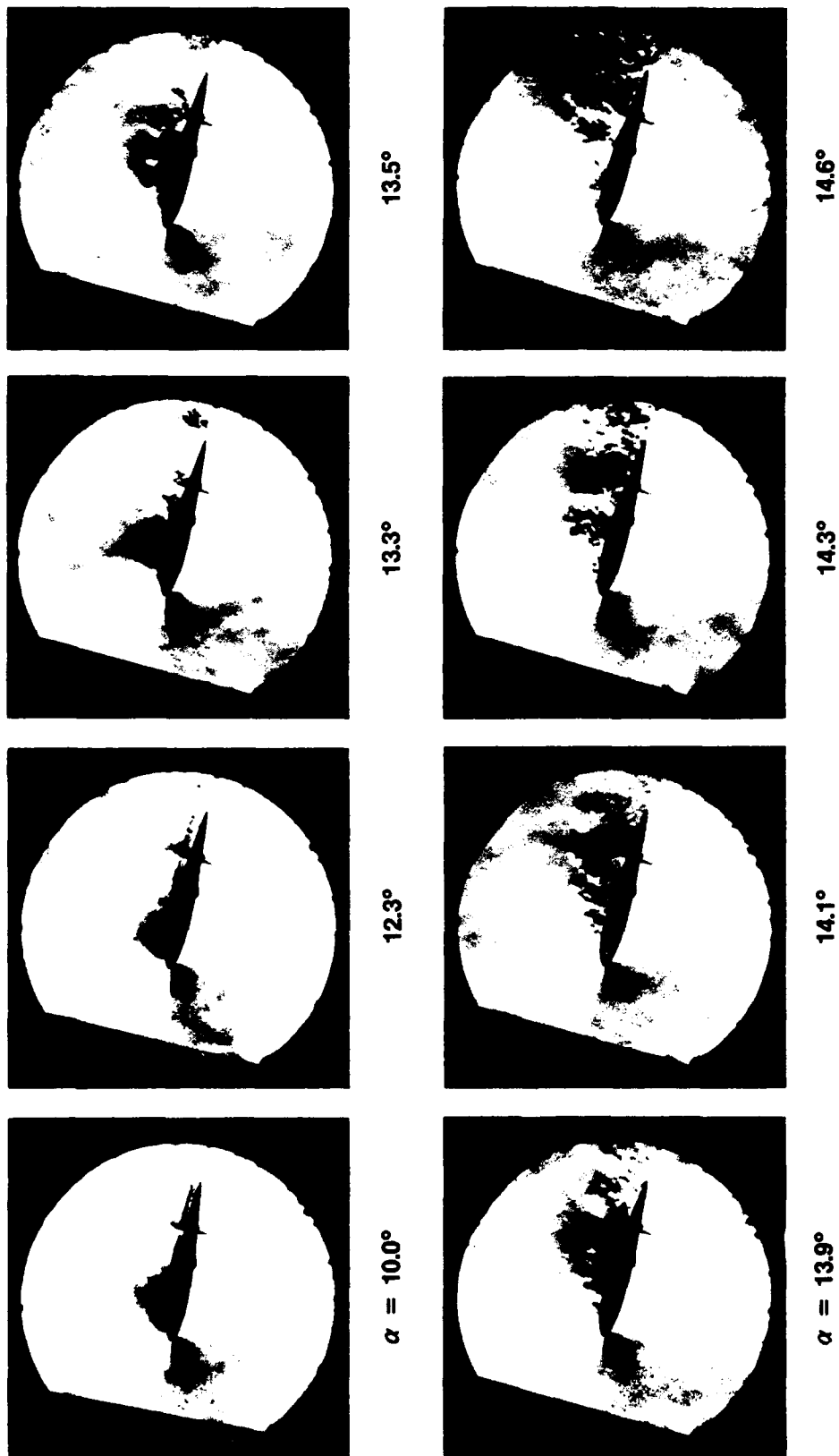


Figure 16. Transition to Stall; $M_\infty = 0.30$, $Re = 540,000$, $k = 0.075$

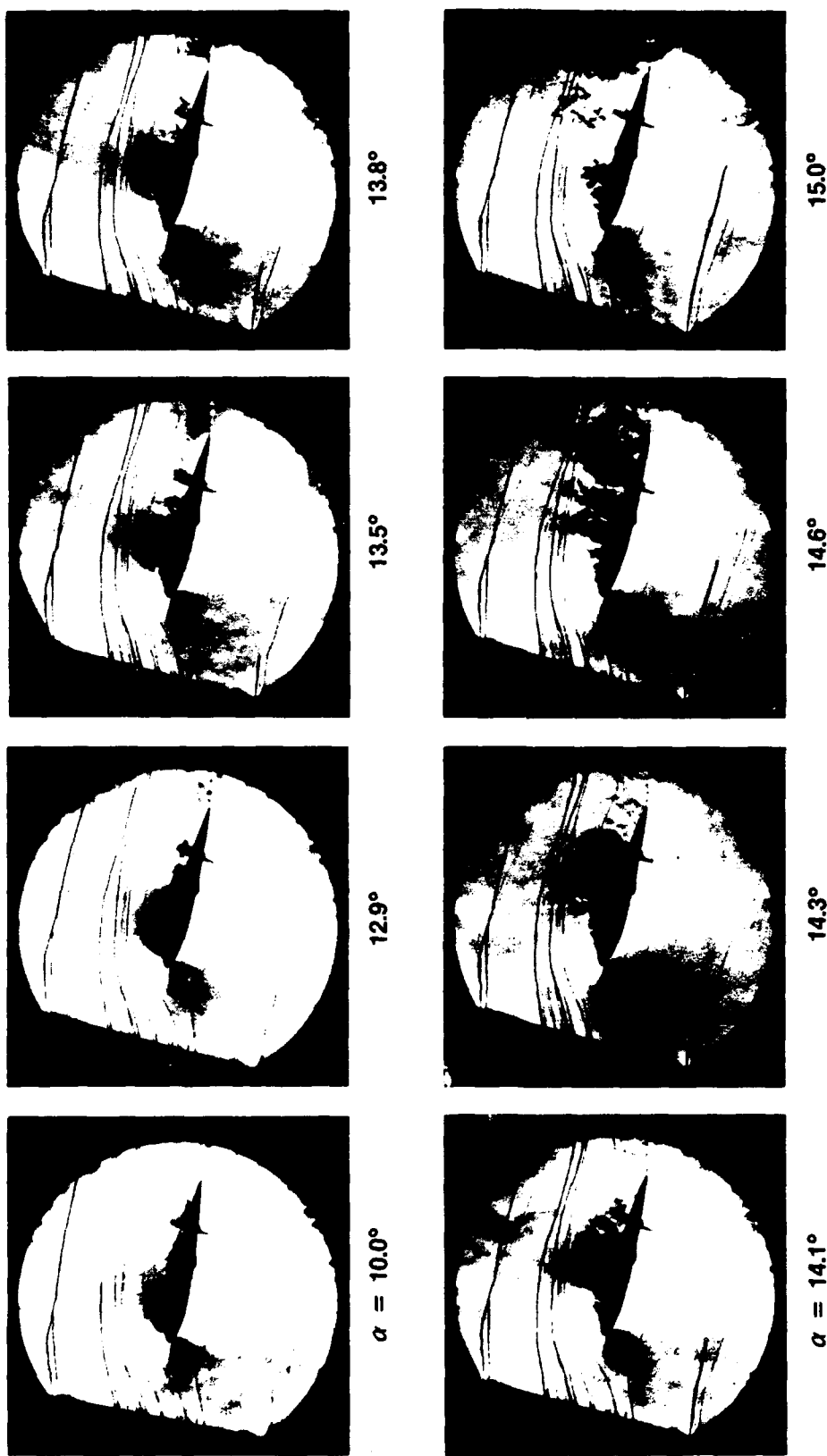


Figure 17. Transition to Stall; $M_\infty = 0.30$, $Re = 540,000$, $k = 0.10$

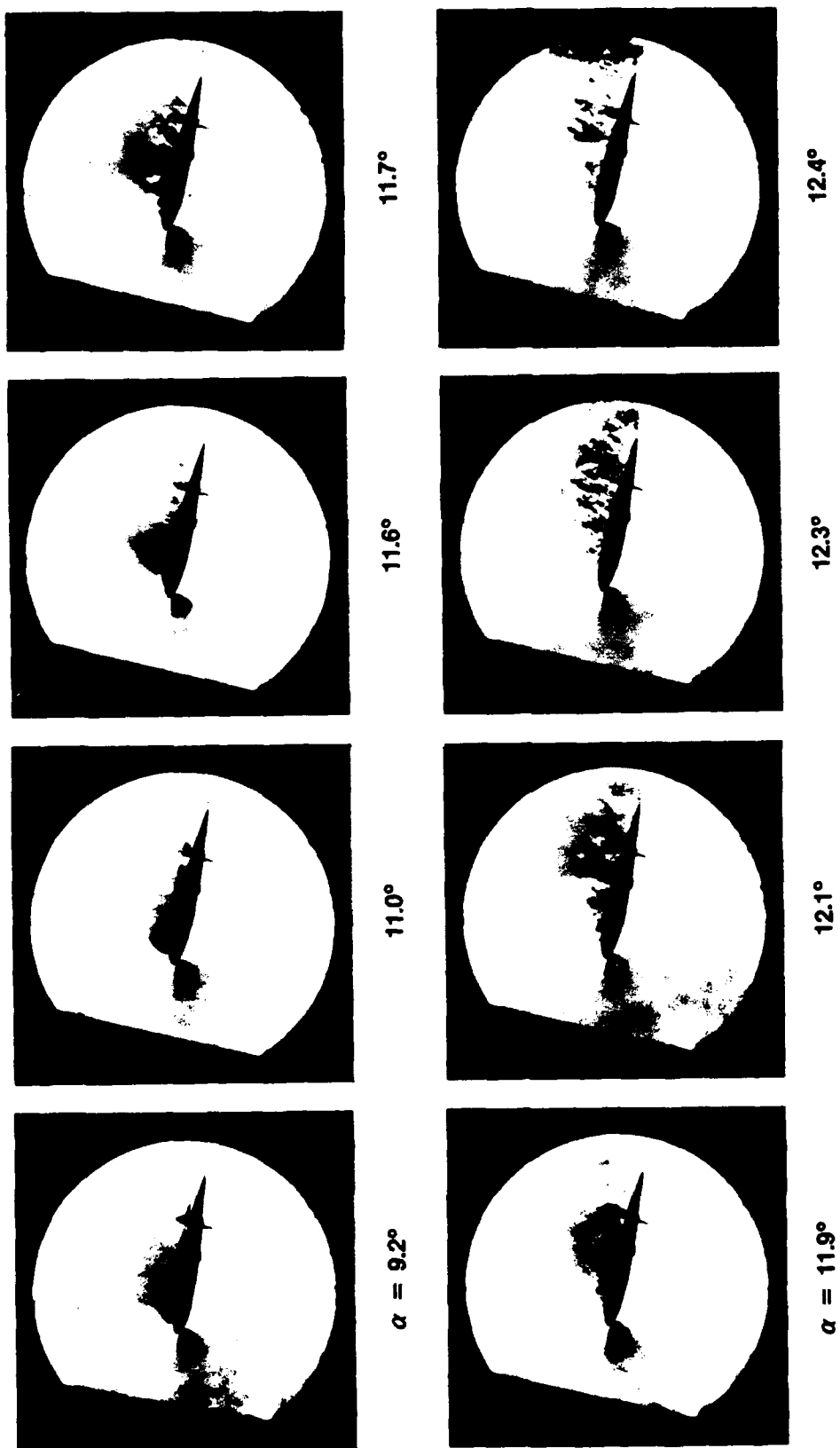


Figure 18. Transition to Stall; $M_\infty = 0.35$, $Re = 630,000$, $k = 0.025$

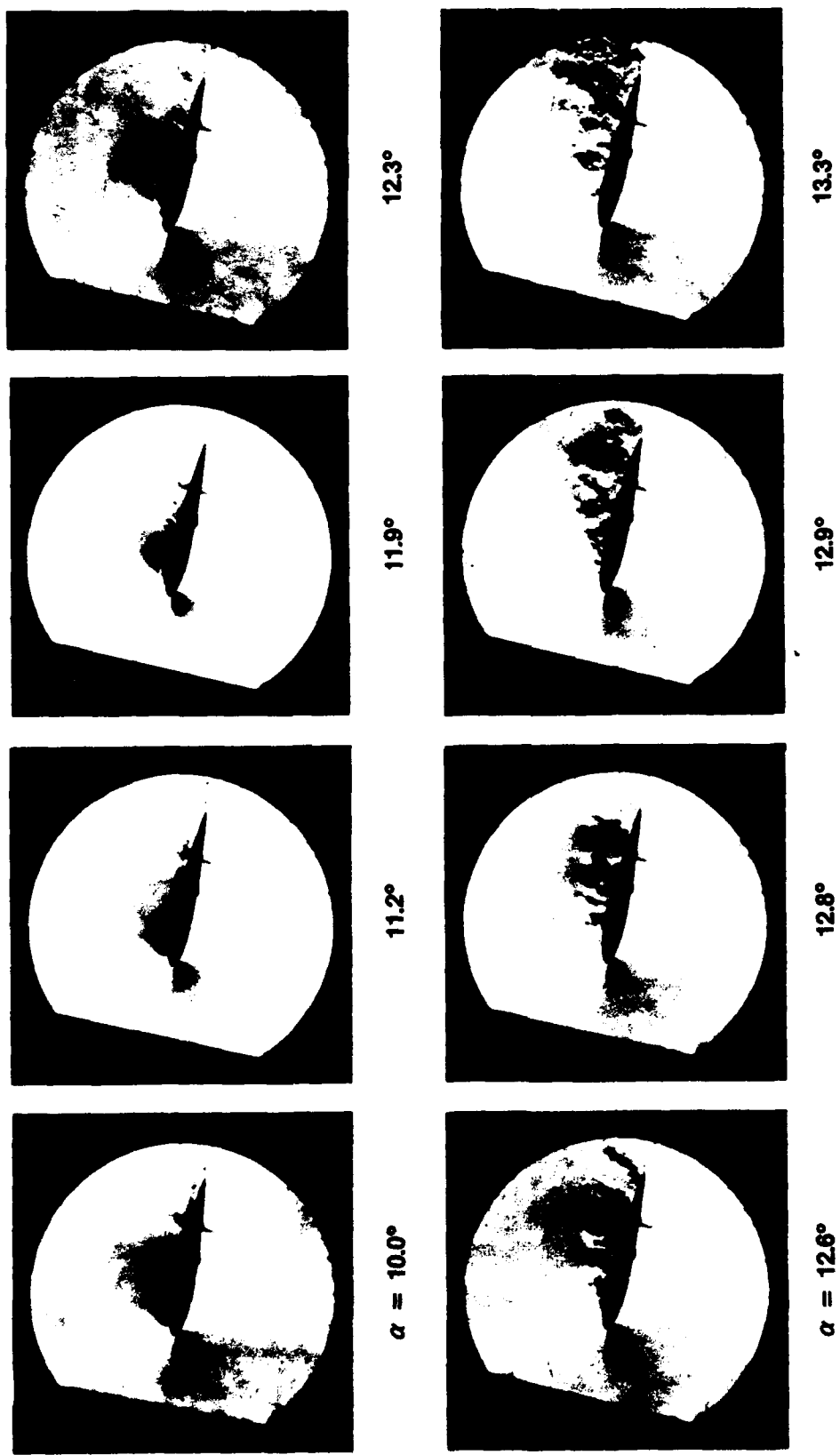


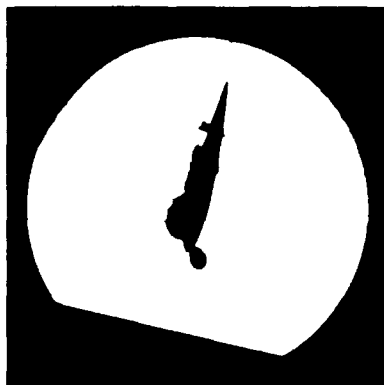
Figure 19. Transition to Stall; $M_\infty = 0.35$, $Re = 630,000$, $k = 0.050$



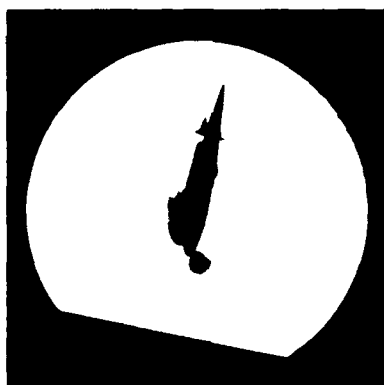
12.8°



12.4°



11.6°



$\alpha = 10.0^\circ$



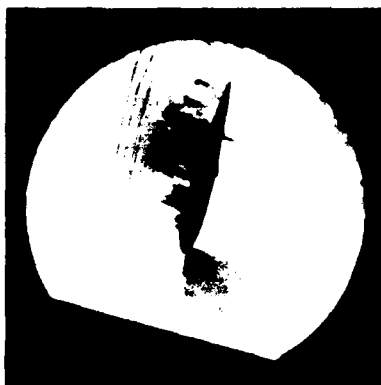
14.1°



13.8°



13.5°



$\alpha = 13.1^\circ$

Figure 20. Transition to Stall; $M_\infty = 0.35$, $Re = 630,000$, $k = 0.075$

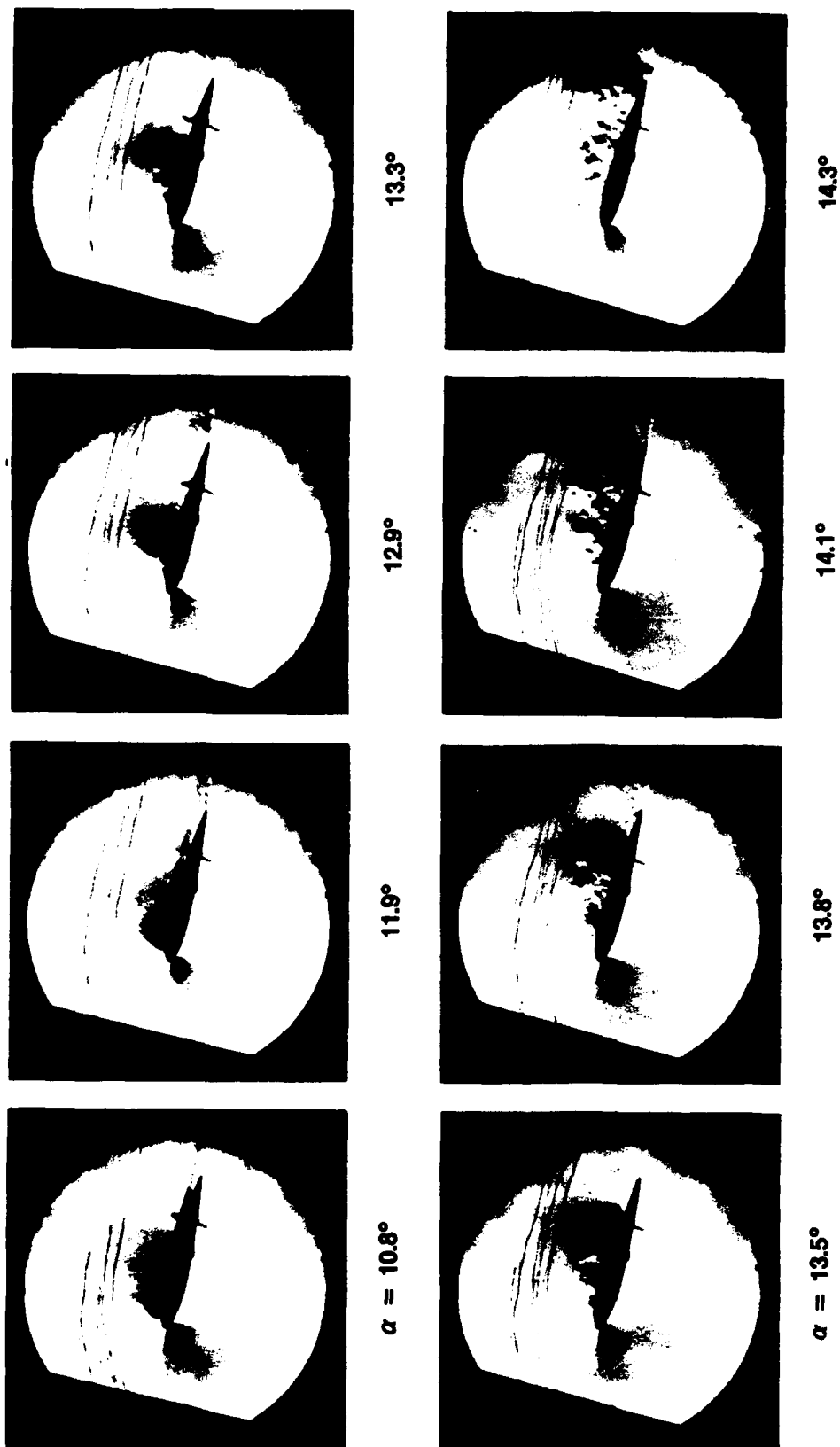


Figure 21. Transition to Stall; $M_\infty = 0.35$, $Re = 630,000$, $k = 0.10$

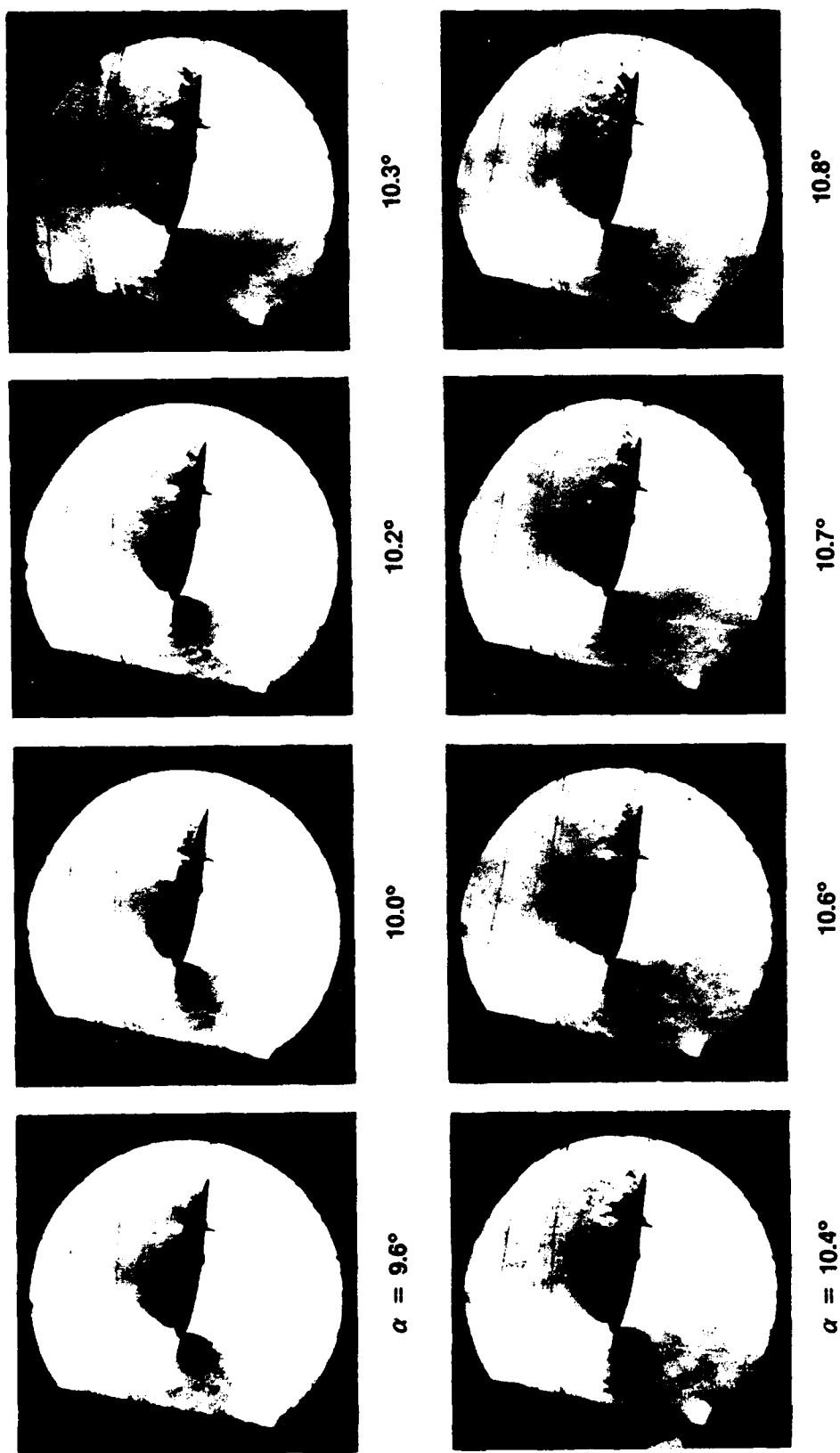
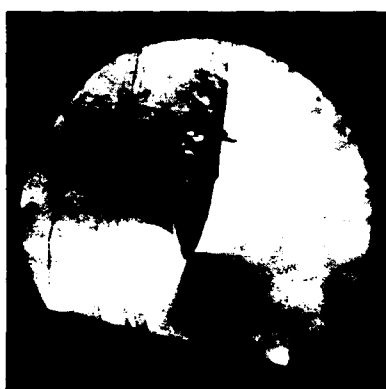


Figure 22. Transition to Stall; $M_\infty = 0.40$, $Re = 720,000$, $k = 0.025$



11.4°



11.3°



11.2°



$\alpha = 11.0^\circ$



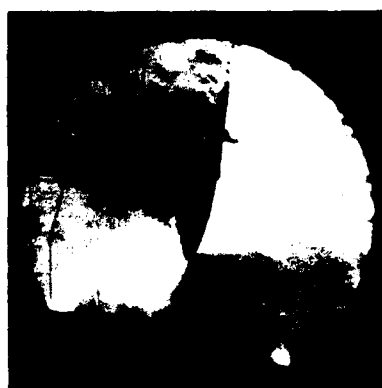
13.5°



11.9°



11.6°



$\alpha = 11.5^\circ$

Figure 22. Transition to Stall; $M_\infty = 0.40$, $Re = 720,000$, $k = 0.025$ (Continued)

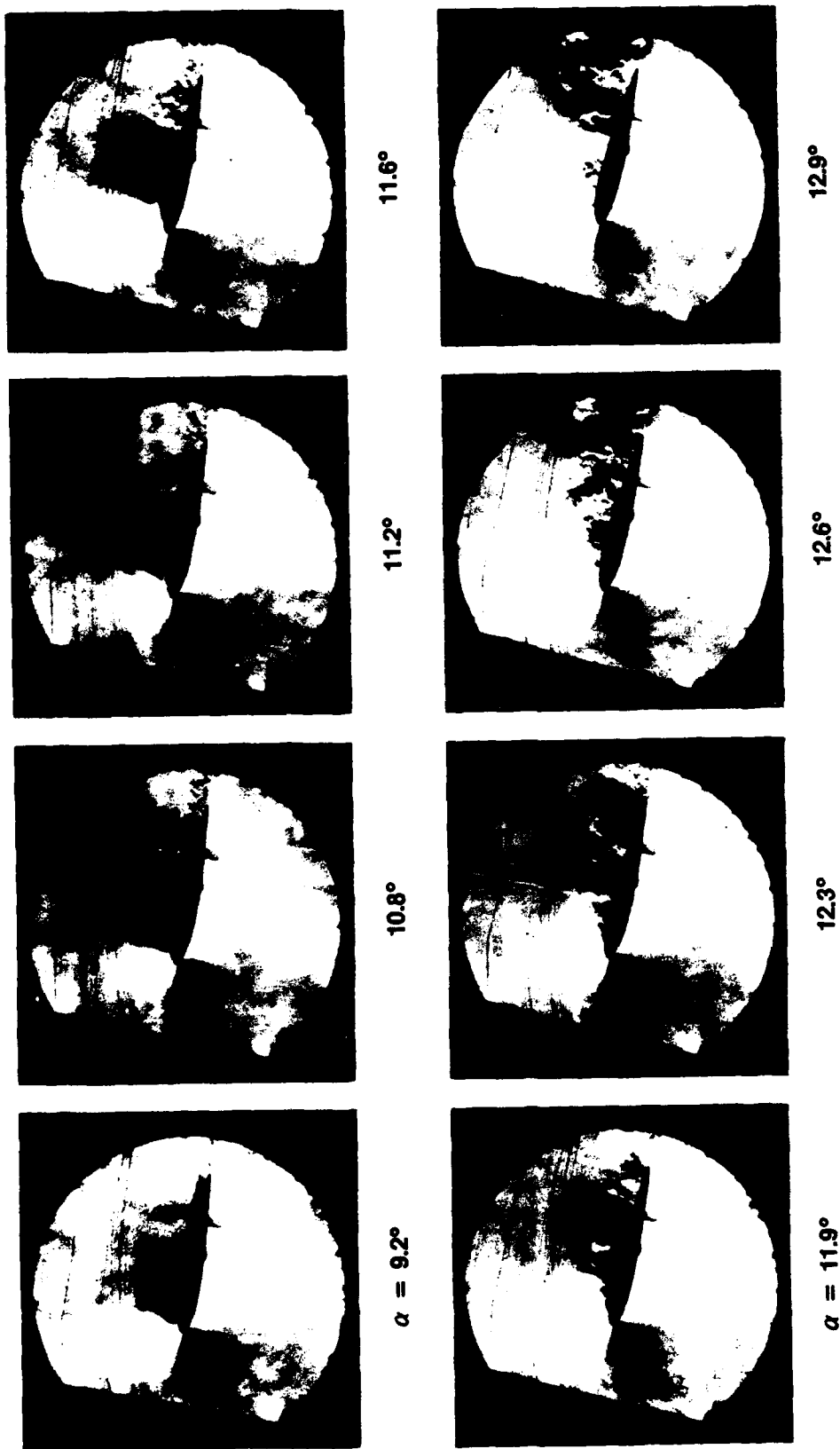


Figure 23. Transition to Stall; $M_\infty = 0.40$, $Re = 720,000$, $k = 0.050$

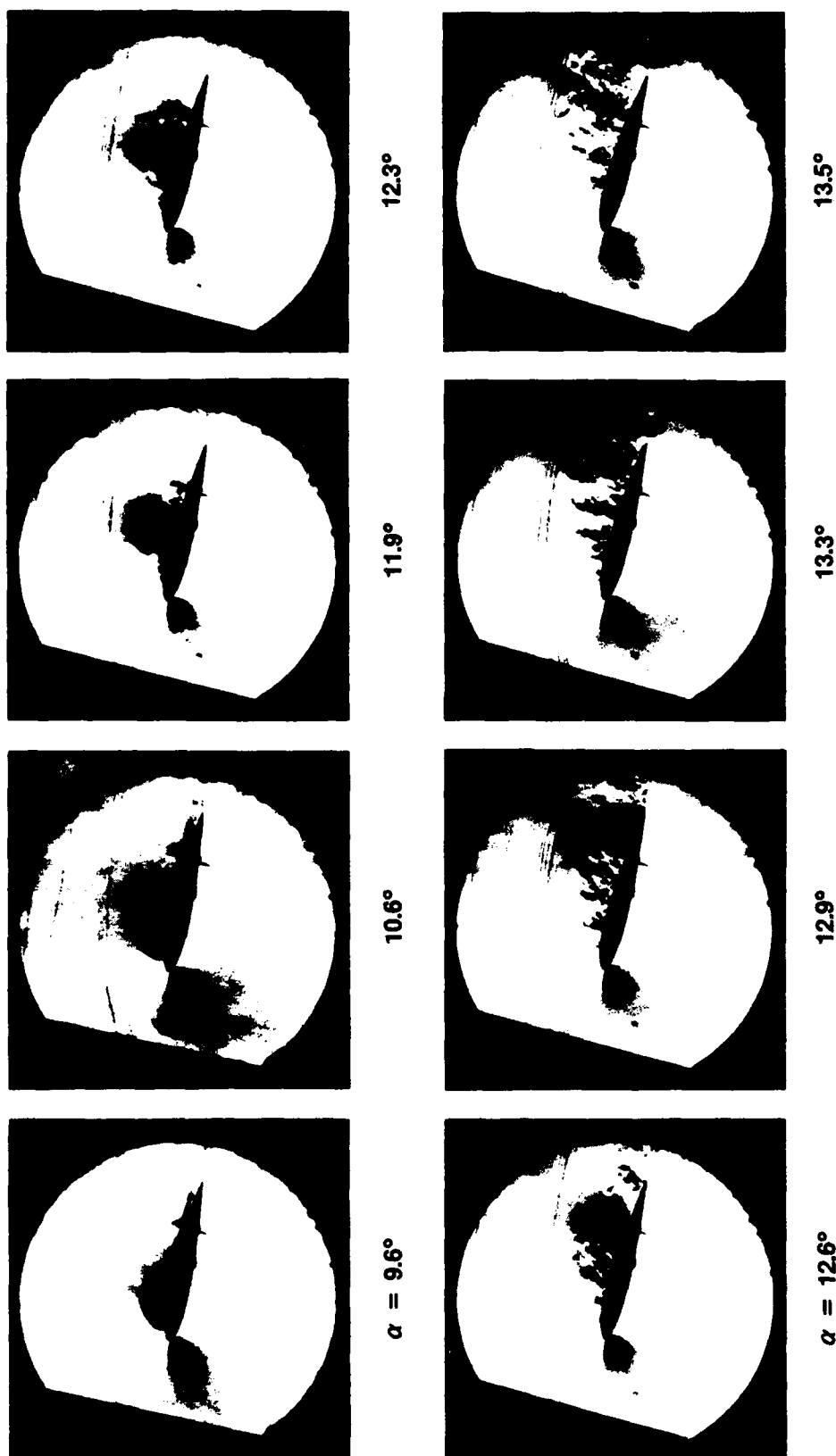


Figure 24. Transition to Stall; $M_\infty = 0.40$, $Re = 720,000$, $k = 0.075$

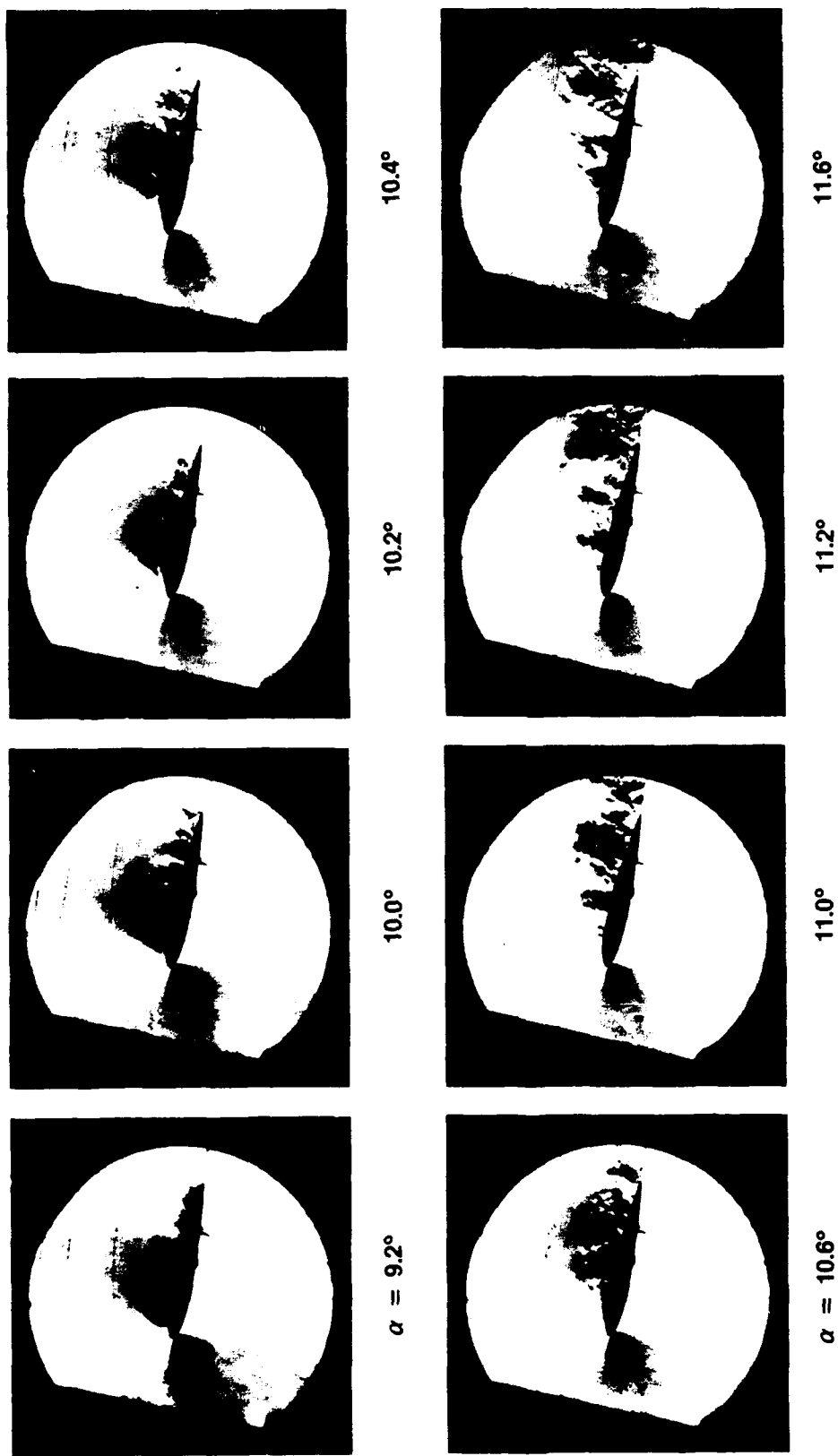


Figure 25. Transition to Stall; $M_\infty = 0.45$, $Re = 810,000$, $k = 0.025$

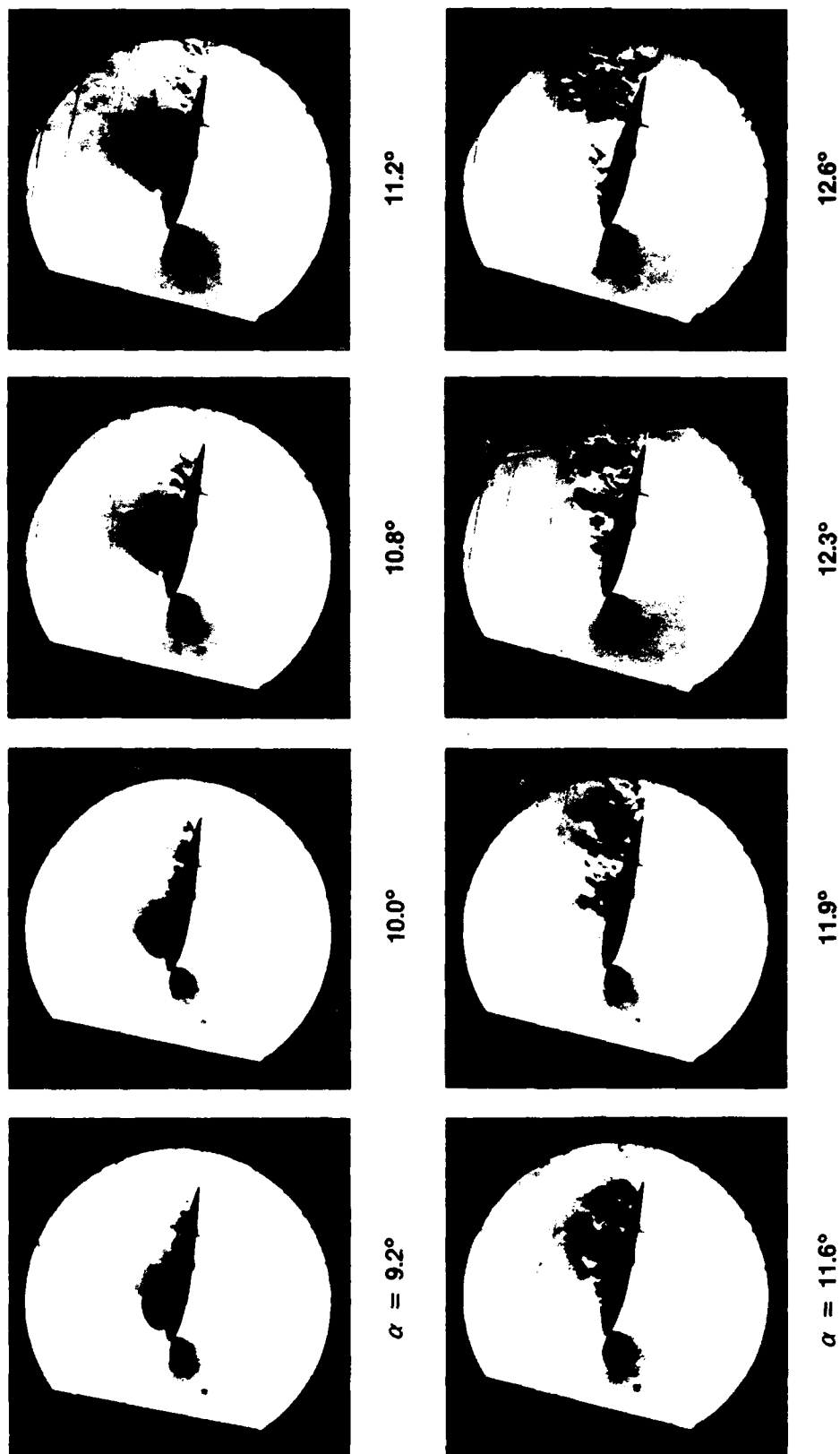
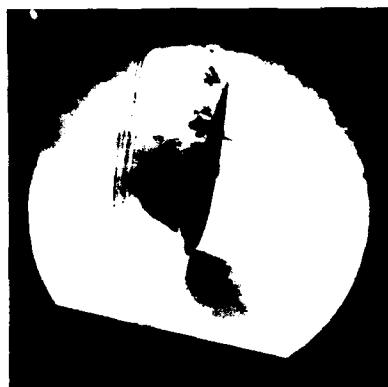


Figure 26. Transition to Stall; $M_\infty = 0.45$, $Re = 810,000$, $k = 0.050$



$\alpha = 9.2^\circ$



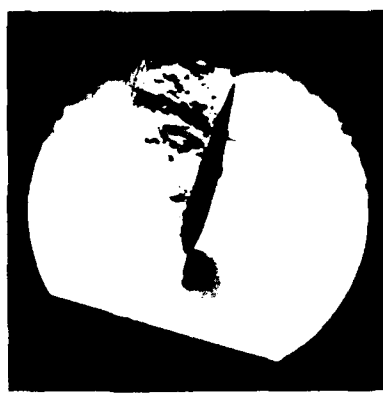
10.0°



11.2°



11.9°



$\alpha = 12.3^\circ$



12.6°



12.9°



13.5°

Figure 27. Transition to Stall; $M_\infty = 0.45$, $Re = 810,000$, $k = 0.075$

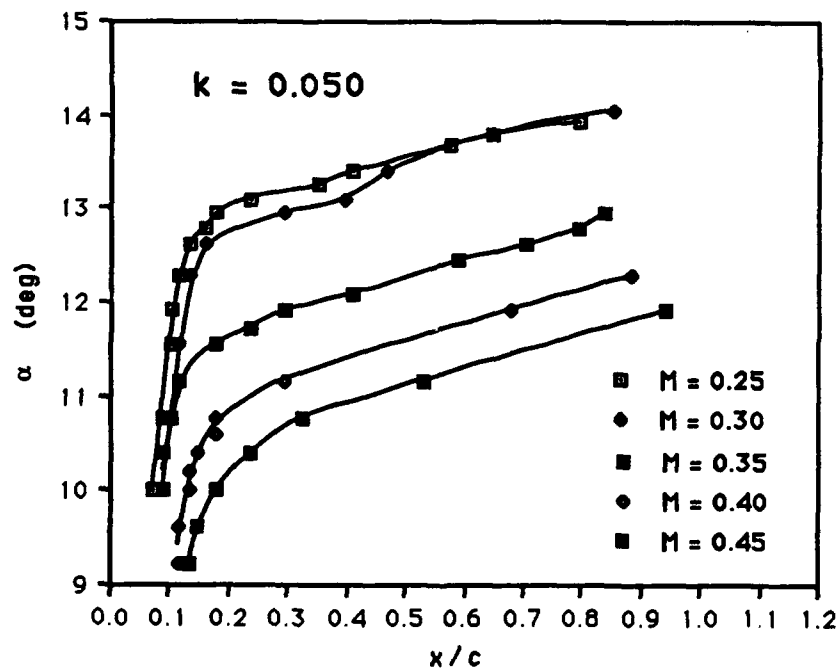
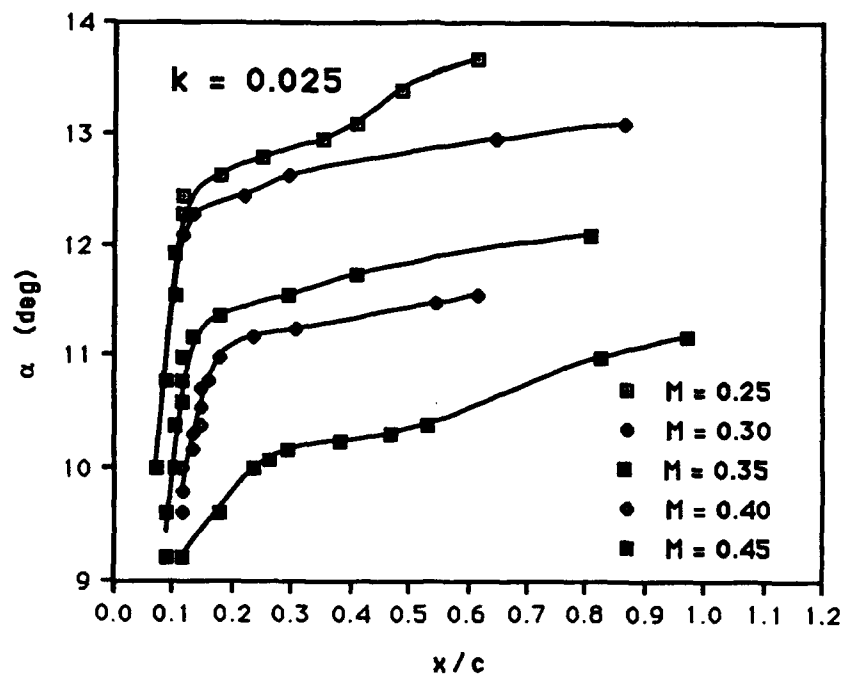


Figure 28. Compressibility Effects on Transition to Stall

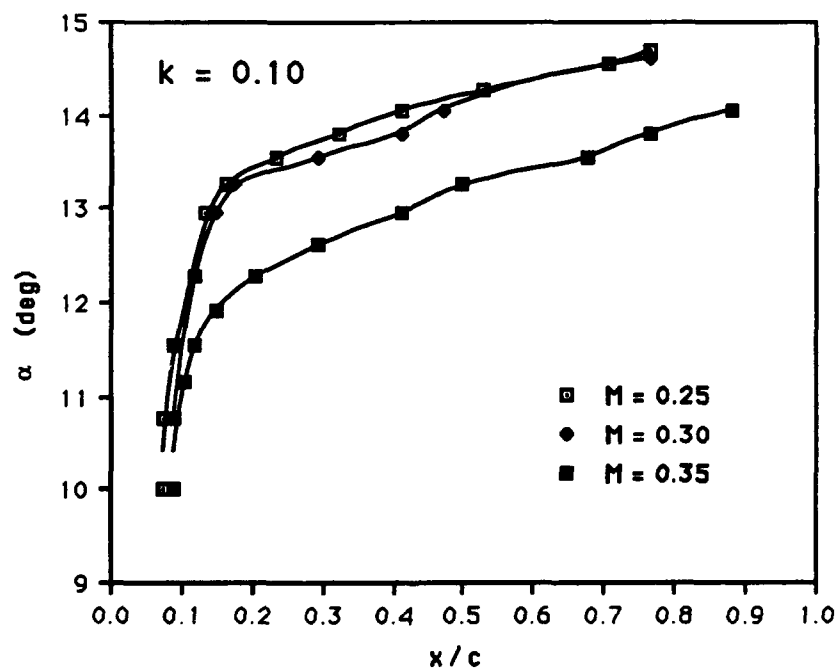
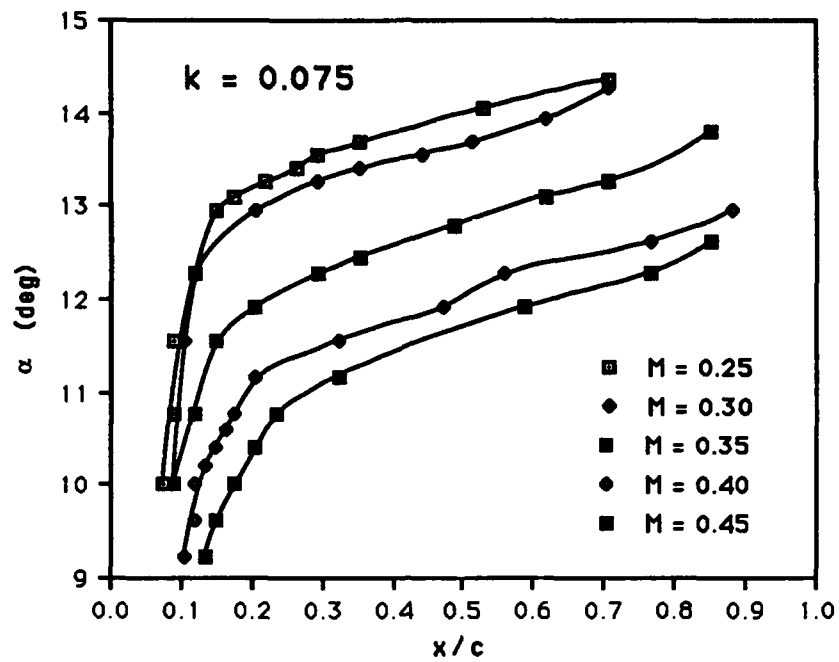


Figure 28. Compressibility Effects on Transition to Stall (Continued)

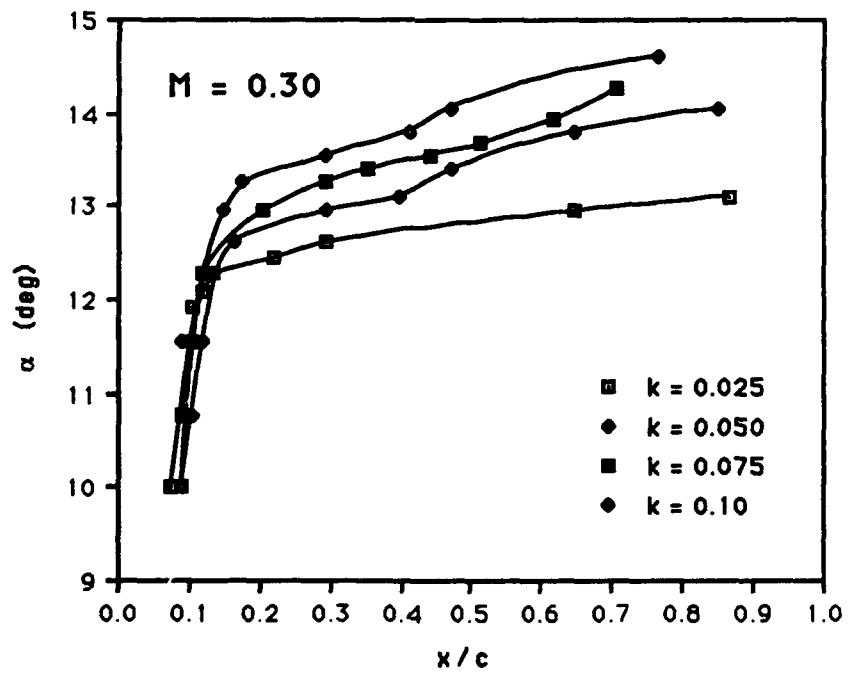
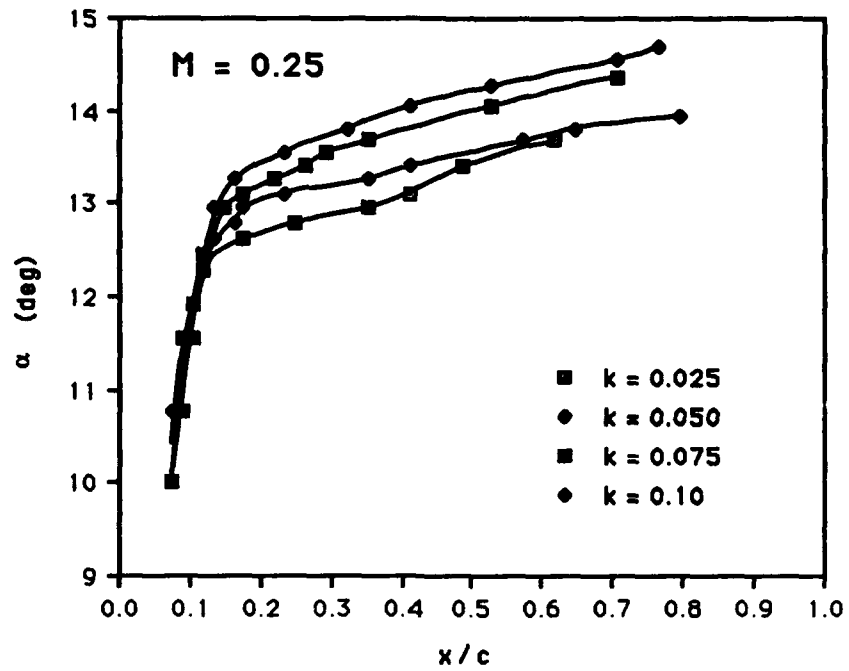


Figure 29. Reduced Frequency Effects on Transition to Stall

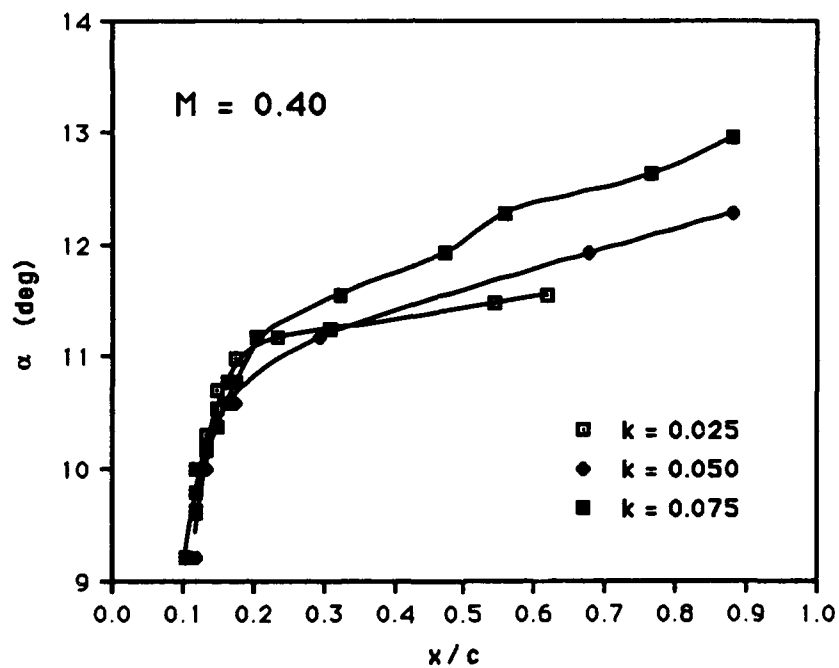
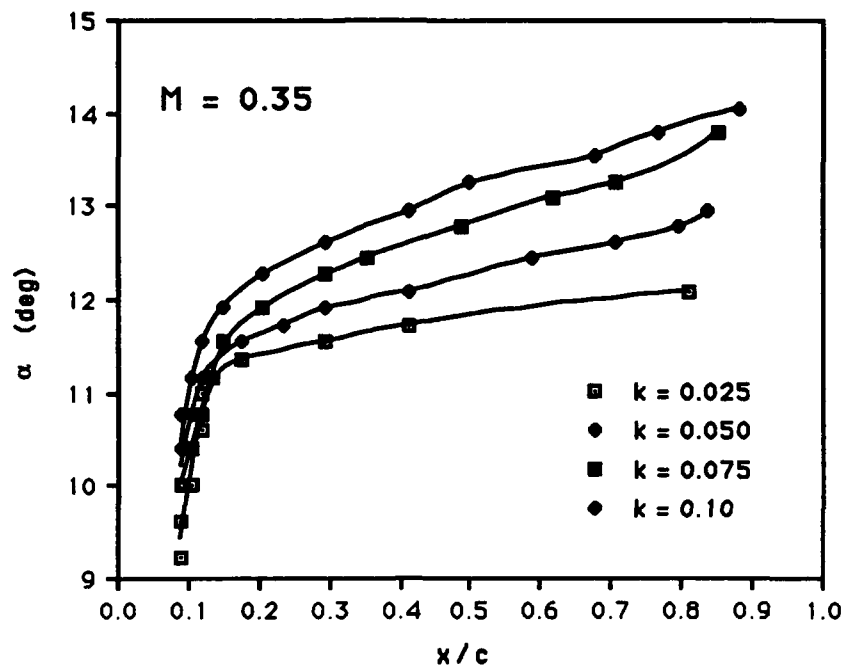


Figure 29. Reduced Frequency Effects on Transition to Stall (Continued)

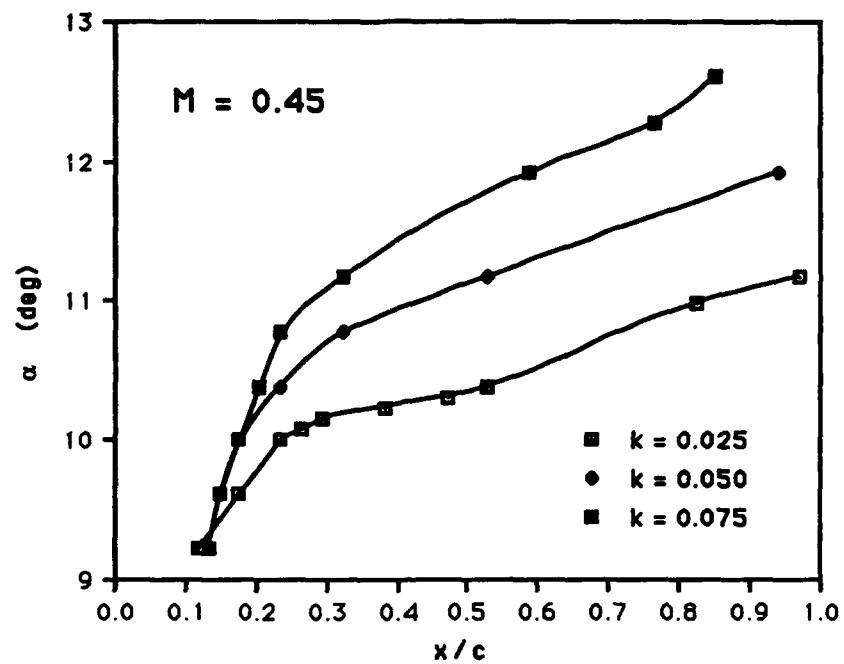


Figure 29. Reduced Frequency Effects on Transition to Stall (Continued)

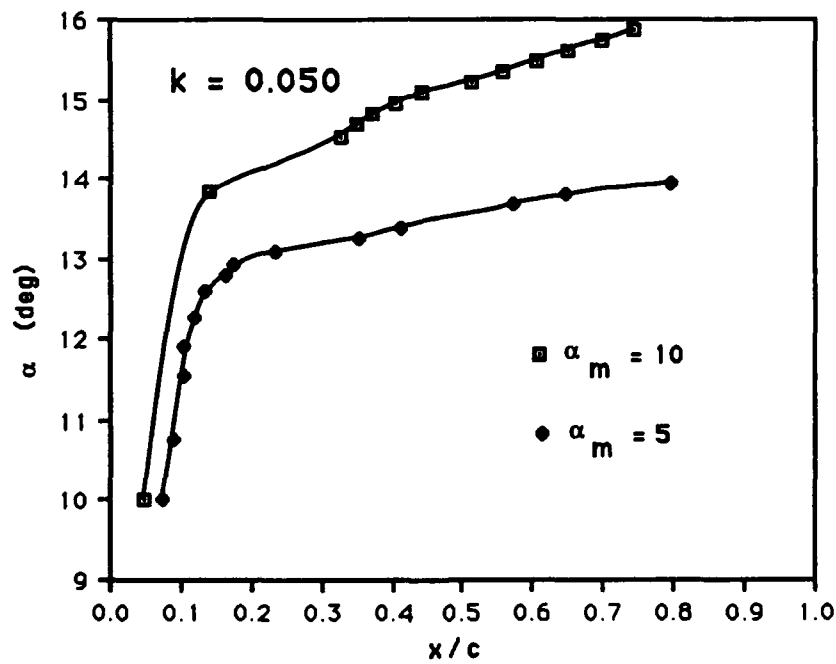
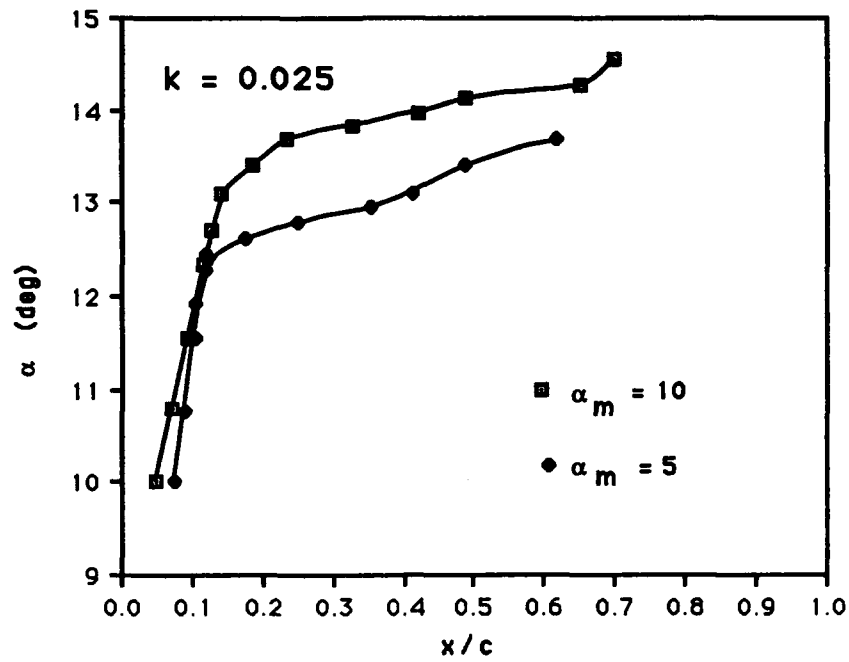


Figure 30. Amplitude Effects on Transition to Stall;
 $M = 0.25$, $Re = 450,000$

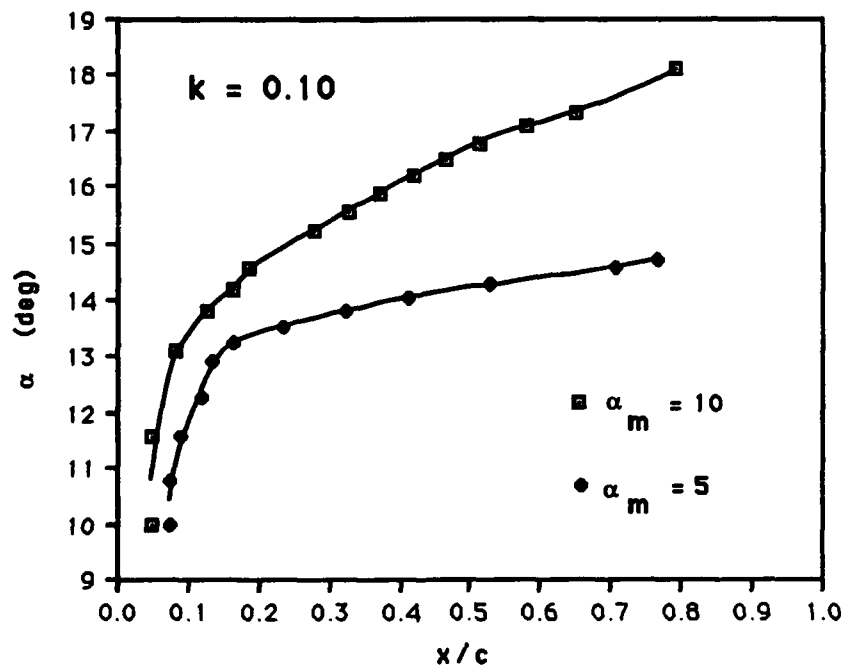
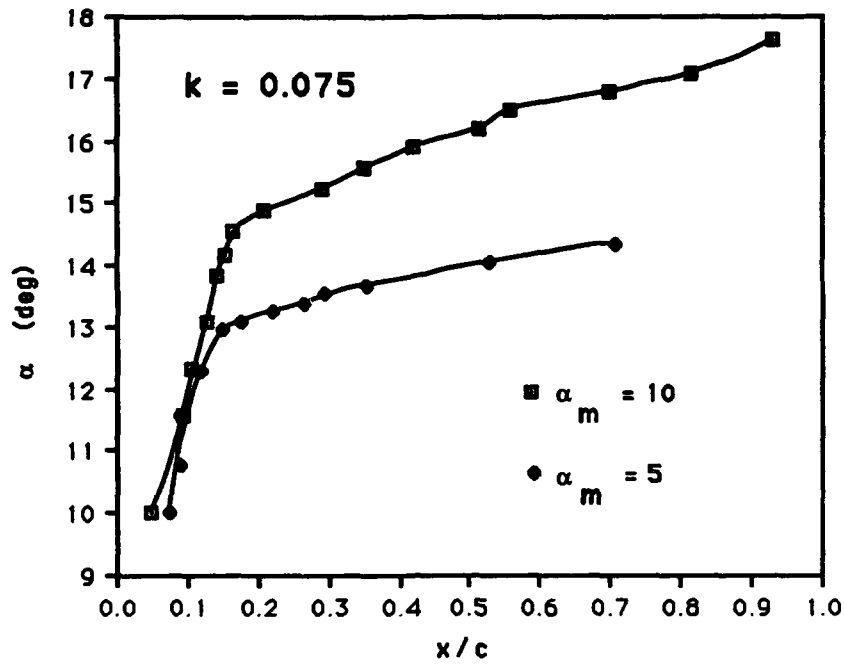


Figure 30. Amplitude Effects on Transition to Stall;
 $M = 0.25$, $Re = 450,000$ (Continued)

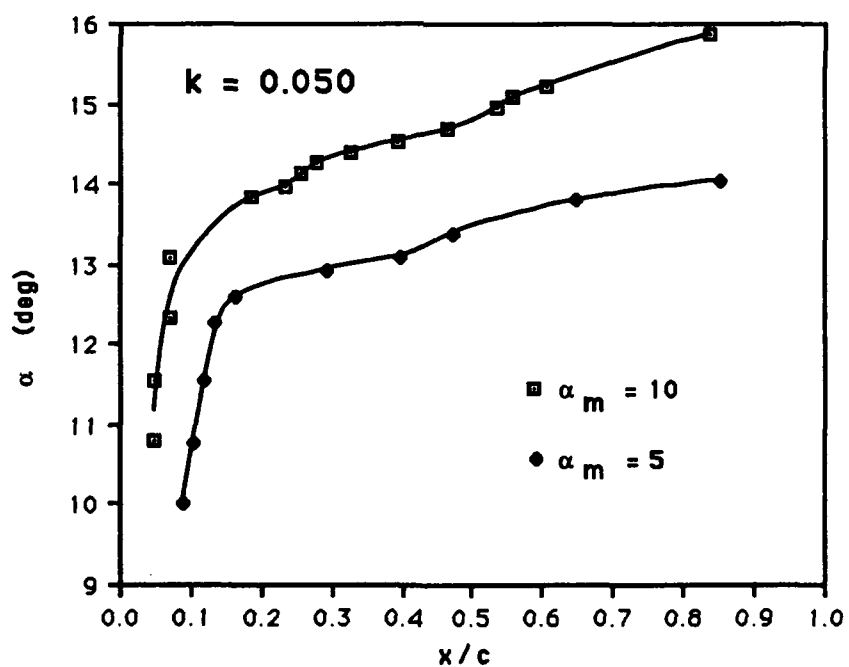
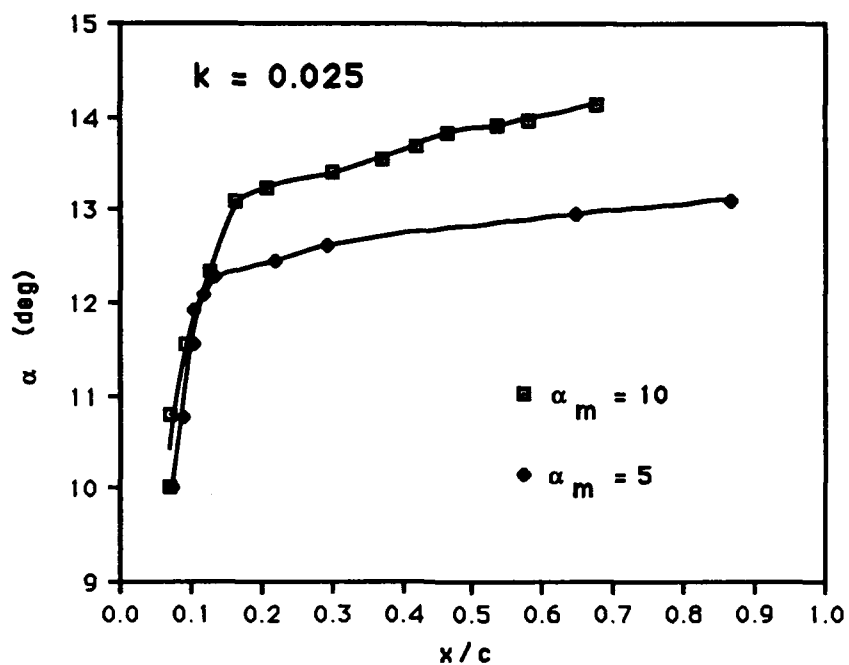


Figure 31. Amplitude Effects on Transition to Stall;
 $M = 0.30$, $Re = 540,000$

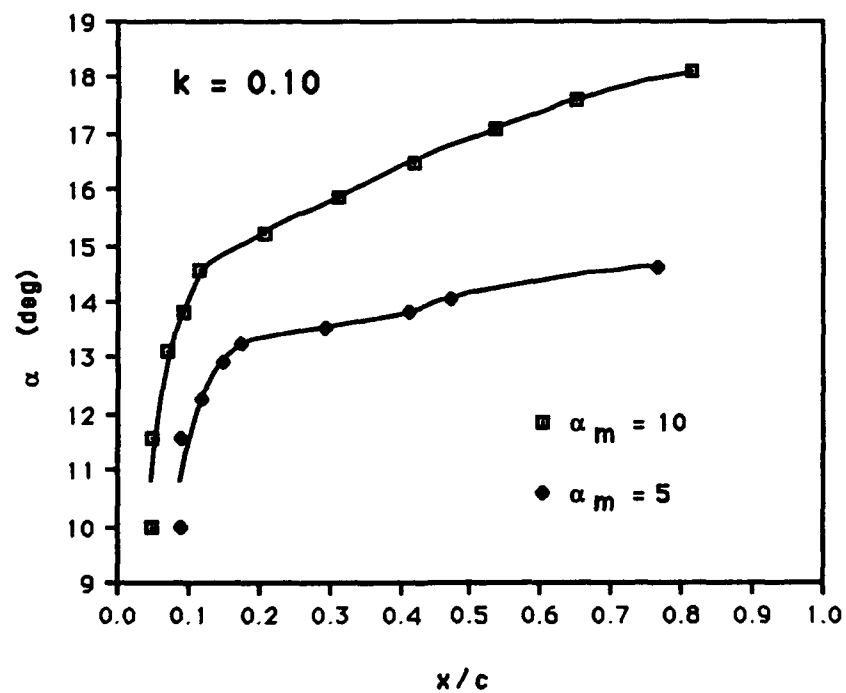
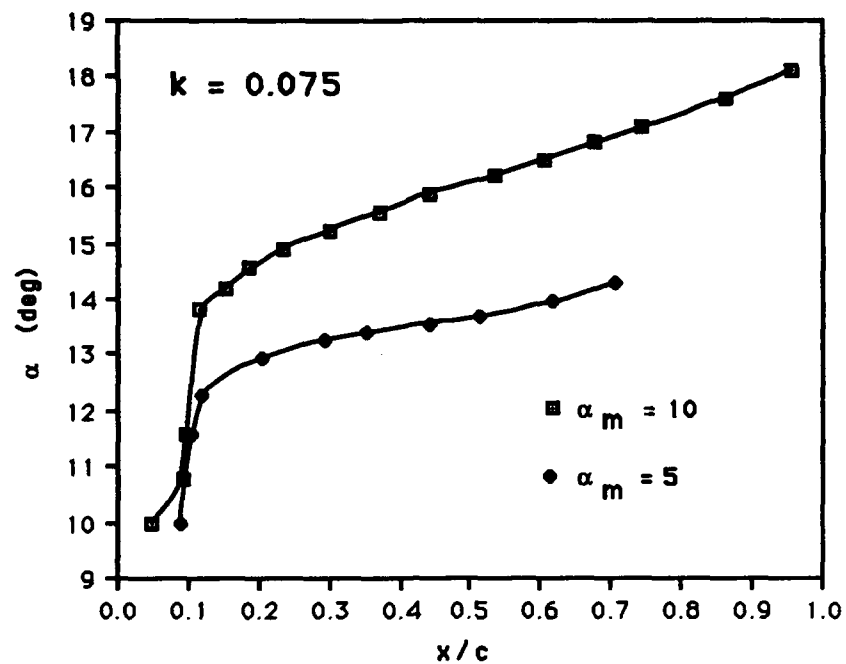


Figure 31. Amplitude Effects on Transition to Stall;
 $M = 0.30$, $Re = 540,000$ (Continued)

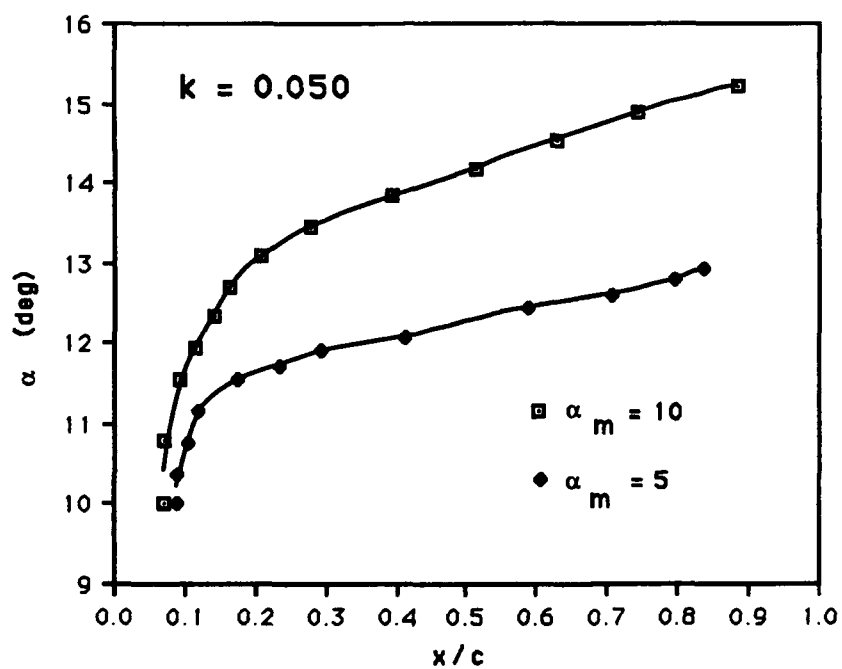
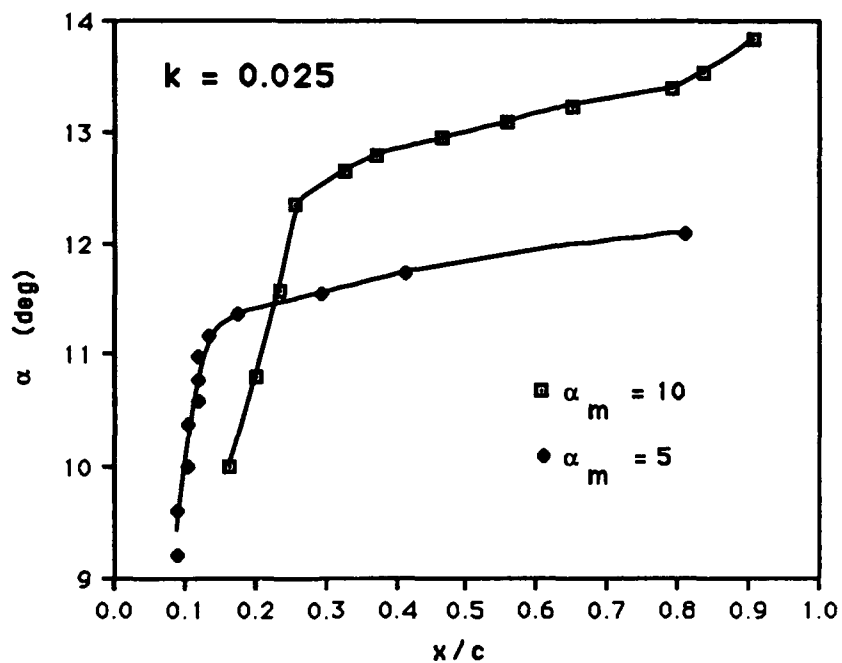


Figure 32. Amplitude Effects on Transition to Stall;
 $M = 0.35$, $Re = 630,000$

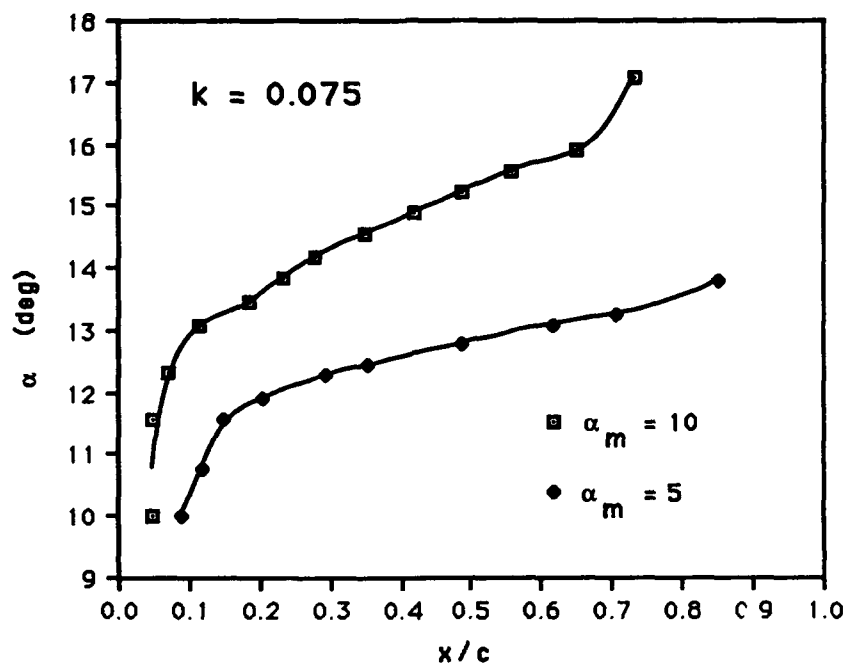


Figure 32. Amplitude Effects on Transition to Stall;
 $M = 0.35$, $Re = 630,000$ (Continued)

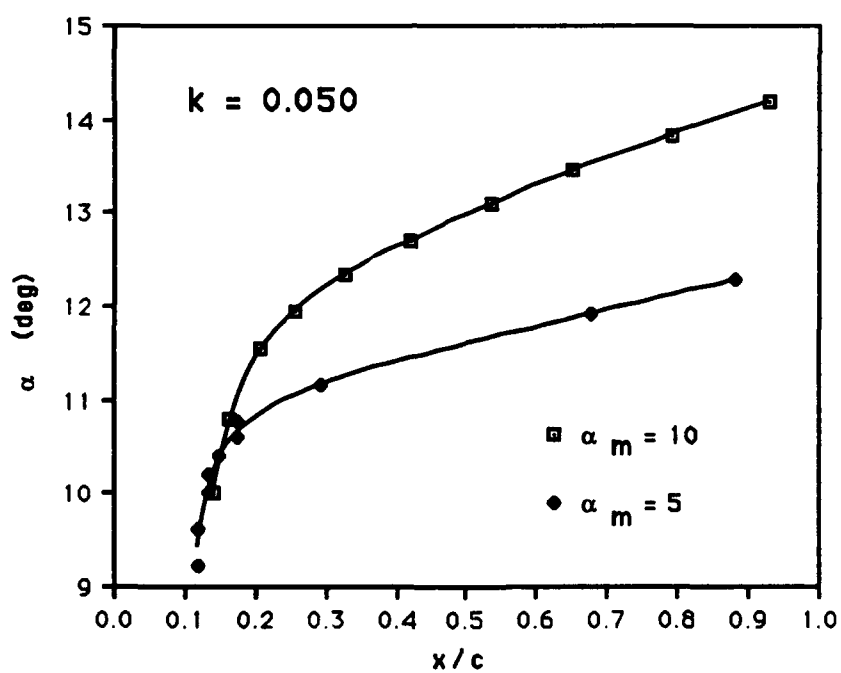
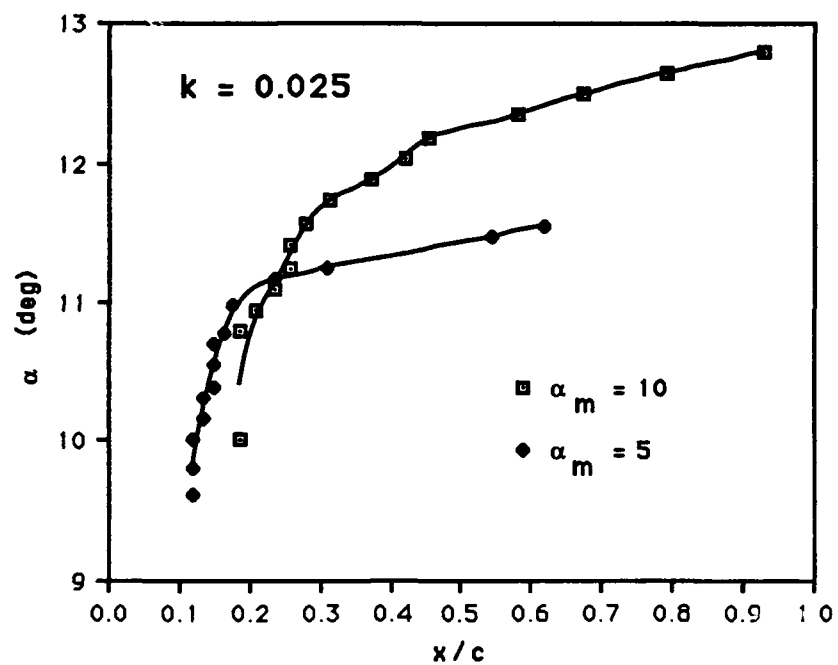


Figure 33. Amplitude Effects on Transition to Stall;
 $M = 0.40$, $Re = 720,000$

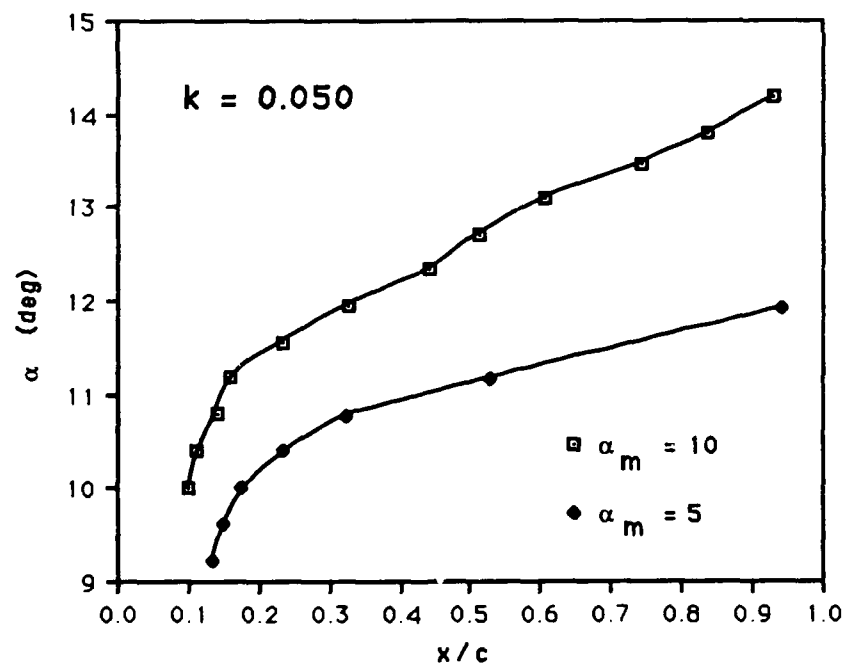
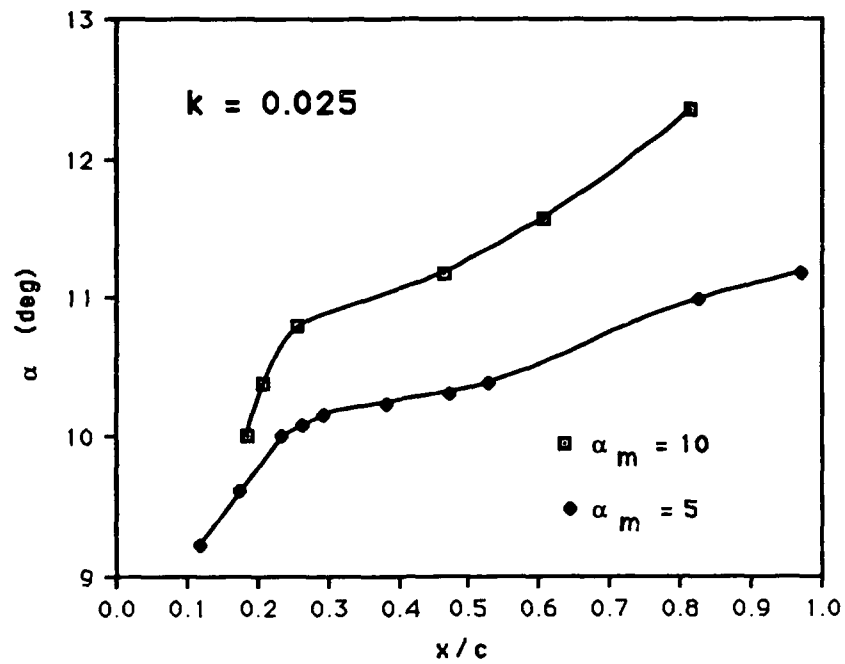


Figure 34. Amplitude Effects on Transition to Stall;
 $M = 0.45$, $Re = 810,000$

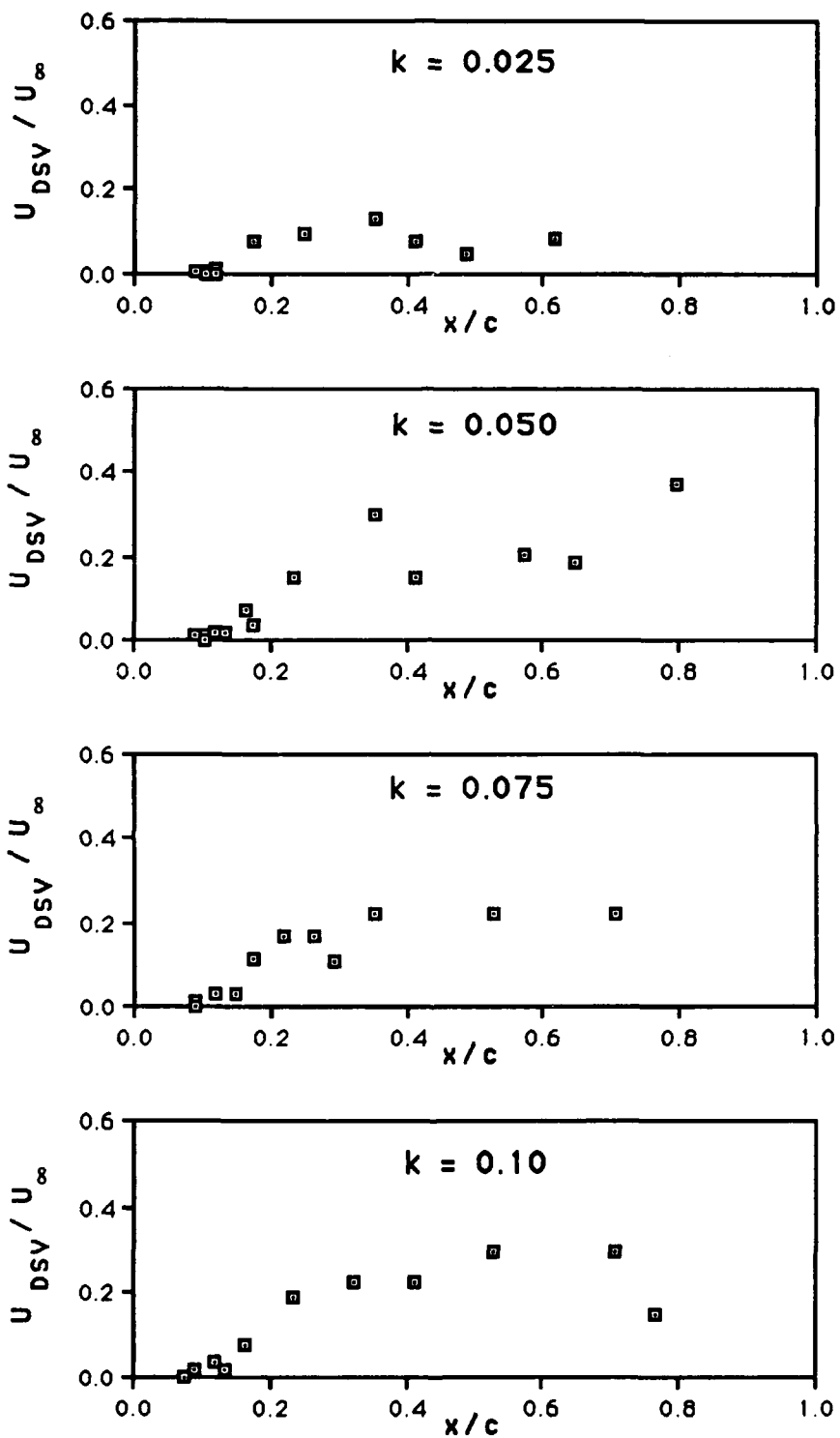


Figure 35. Convection Velocity of the Dynamic Stall Vortex;
 $M = 0.25$, $Re = 450,000$

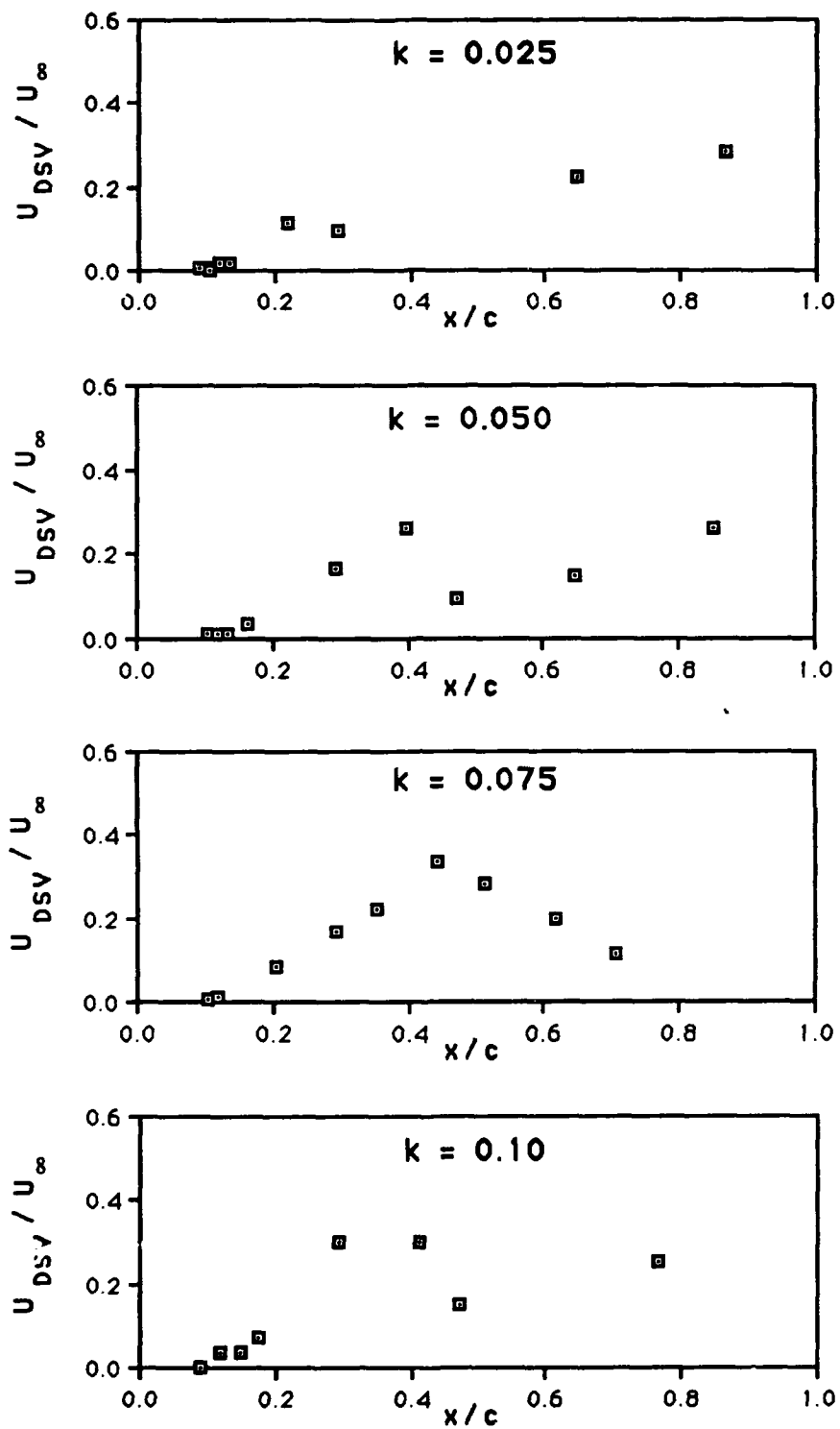


Figure 36. Convection Velocity of the Dynamic Stall Vortex;
 $M = 0.30$, $Re = 540,000$

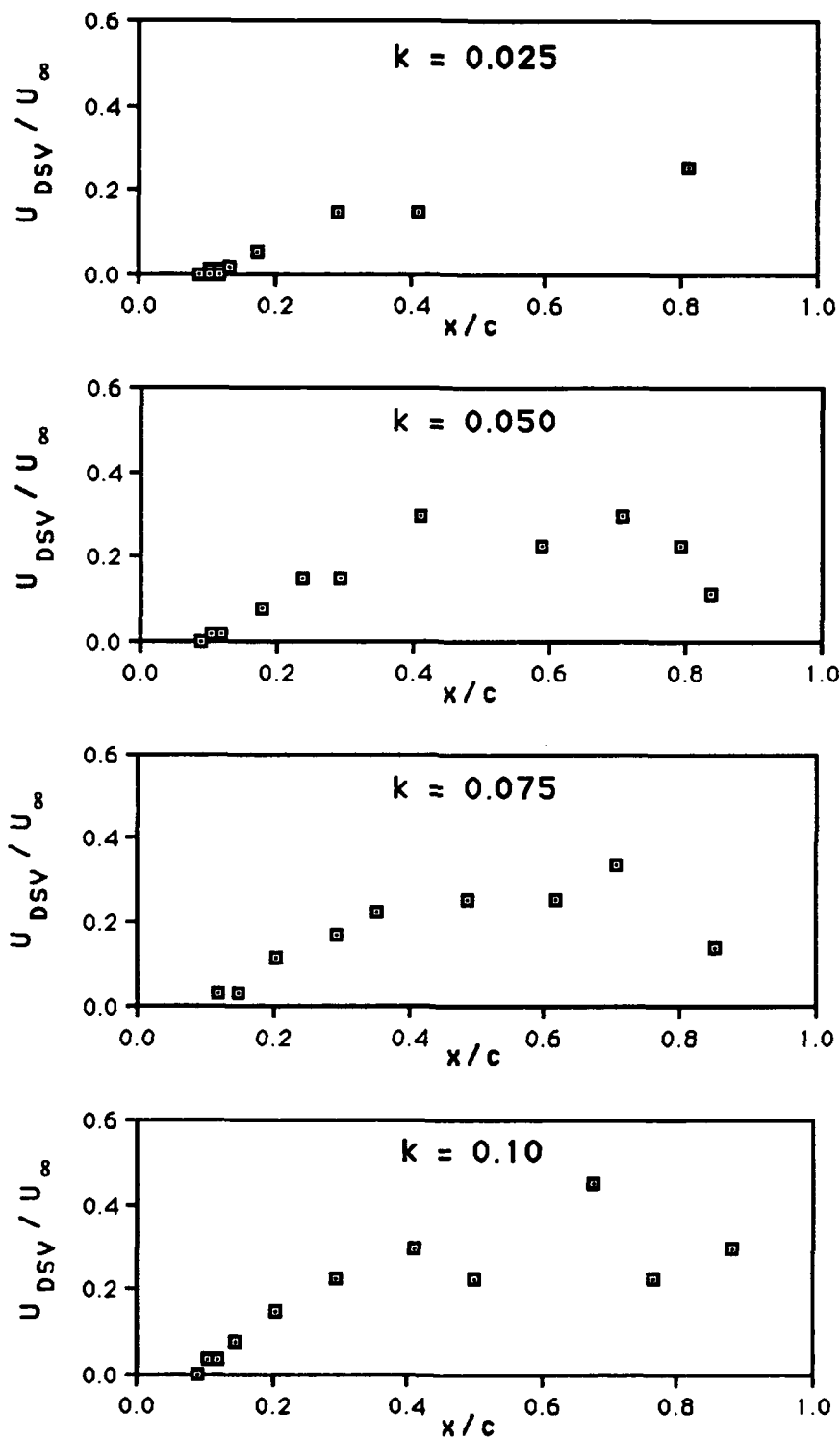


Figure 37. Convection Velocity of the Dynamic Stall Vortex;
 $M = 0.35$, $Re = 630,000$

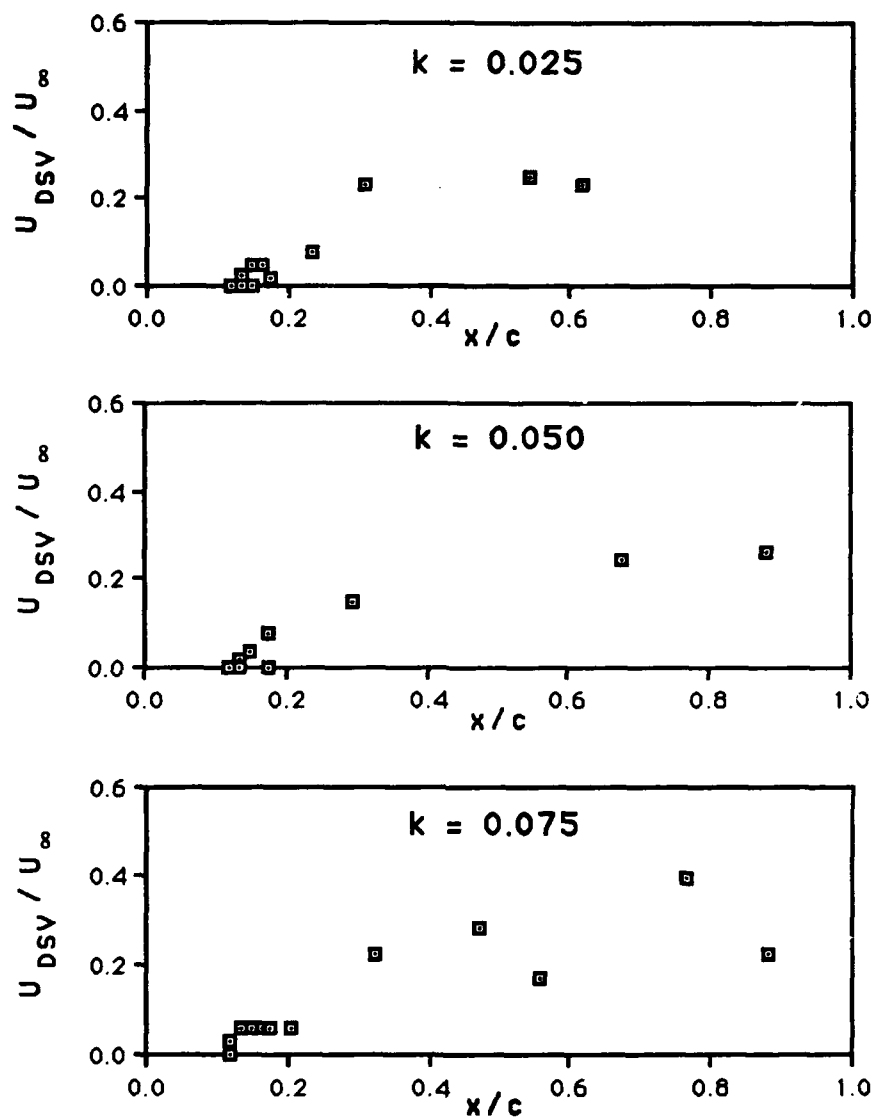


Figure 38. Convection Velocity of the Dynamic Stall Vortex;
 $M = 0.40$, $Re = 720,000$

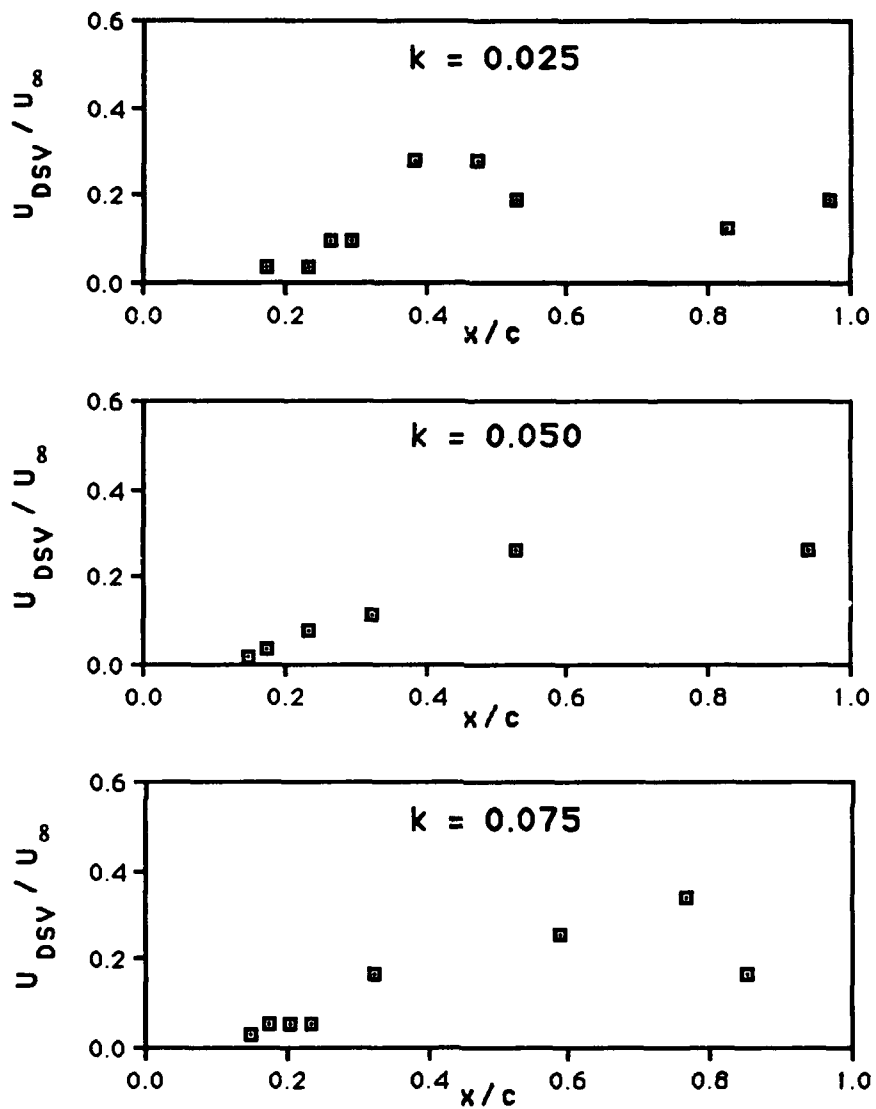


Figure 39. Convection Velocity of the Dynamic Stall Vortex;
 $M = 0.45$, $Re = 810,000$



10.0°



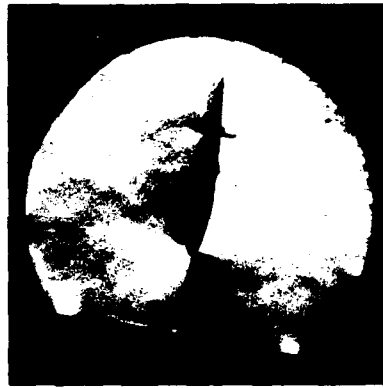
10.8°



$\alpha = 15.0^\circ$



6.5°



8.1°



$\alpha = 9.6^\circ$

Figure 40. Reattachment; $M = 0.25$, $Re = 450,000$, $k = 0.025$



10.0°



10.8°



$\alpha = 15.0^\circ$



6.5°



8.1°



$\alpha = 9.6^\circ$

Figure 41. Reattachment; $M = 0.25$, $Re = 450,000$, $k = 0.050$



10.0°



10.8°



$\alpha = 15.0^\circ$



6.5°



8.1°



$\alpha = 9.6^\circ$

Figure 42. Reattachment; $M = 0.25$, $Re = 450,000$, $k = 0.075$



10.0°



10.8°



$\alpha = 15.0^\circ$



6.5°

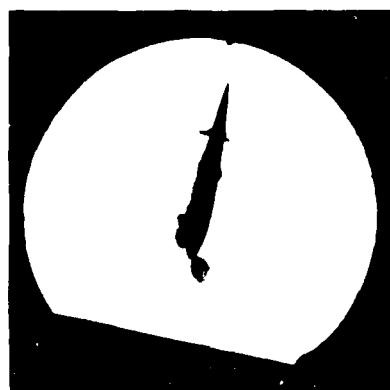


8.1°

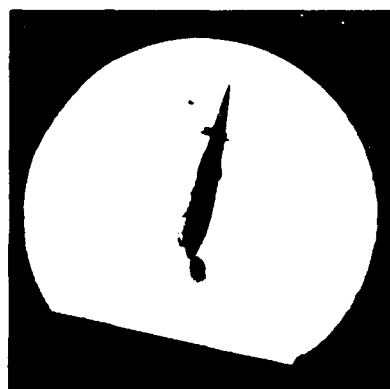


$\alpha = 9.6^\circ$

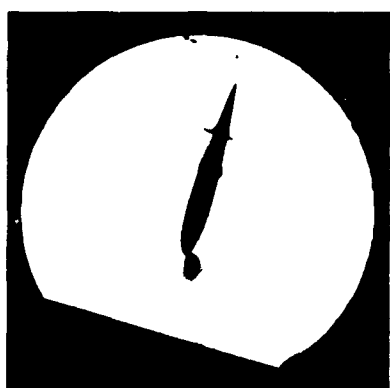
Figure 43. Reattachment; $M = 0.25$, $Re = 450,000$, $k = 0.10$



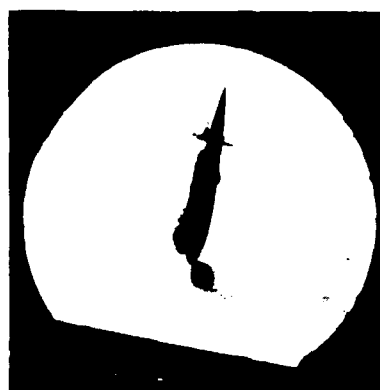
10.4°



10.8°



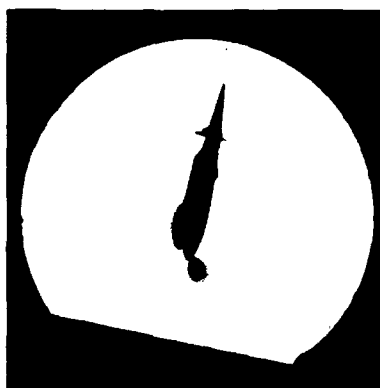
$\alpha = 15.0^\circ$



9.2°



9.6°



$\alpha = 10.0^\circ$

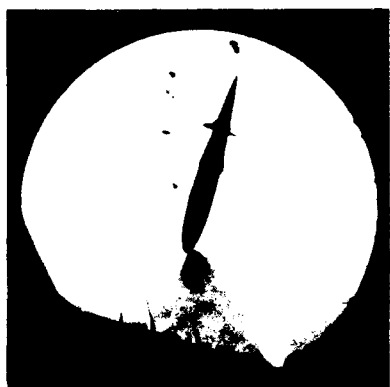
Figure 44. Reattachment; $M = 0.30$, $Re = 540,000$, $k = 0.025$



10.0°



13.5°



$\alpha = 15.0^\circ$

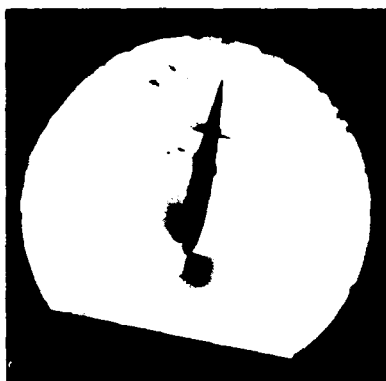


5.0°

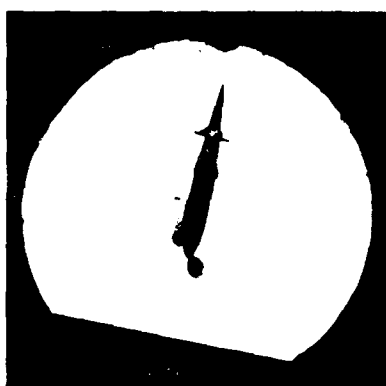


$\alpha = 6.5^\circ$

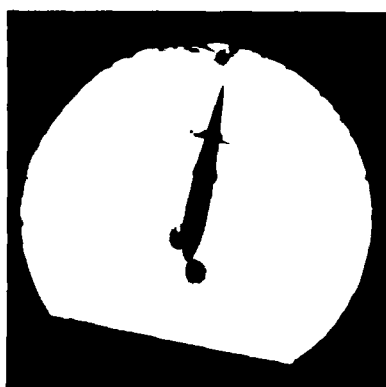
Figure 45. Reattachment; $M = 0.30$, $Re = 540,000$, $k = 0.050$



10.0°



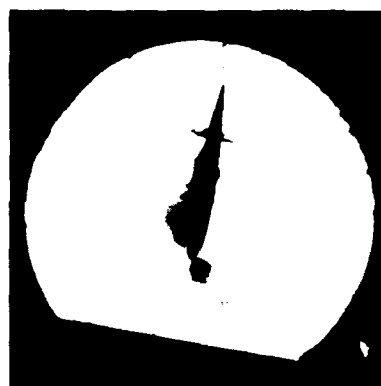
10.4°



$\alpha = 10.8^\circ$



8.1°

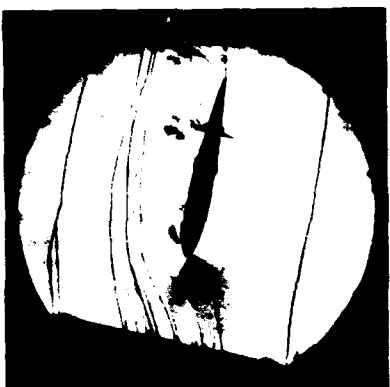


9.2°



$\alpha = 9.6^\circ$

Figure 46. Reattachment; $M = 0.30$, $Re = 540,000$, $k = 0.075$



10.8°



13.5°



$\alpha = 15.0^\circ$



5.0°



6.5°

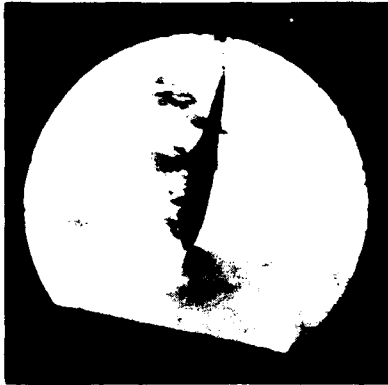


$\alpha = 8.1^\circ$

Figure 47. Reattachment; $M = 0.30$, $Re = 540,000$, $k = 0.10$



10.4°



10.8°

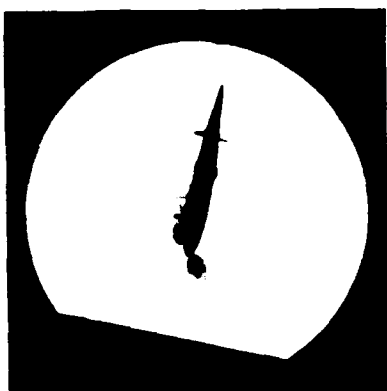


$\alpha = 15.0^\circ$

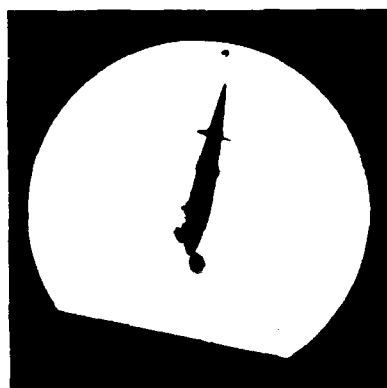


$\alpha = 10.0^\circ$

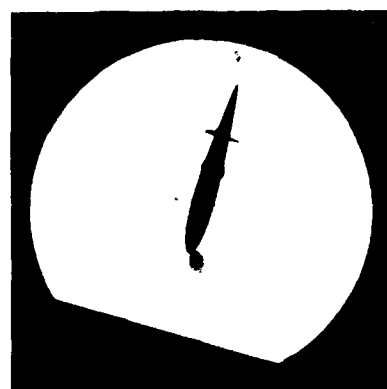
Figure 48. Reattachment; $M = 0.35$, $Re = 630,000$, $k = 0.025$



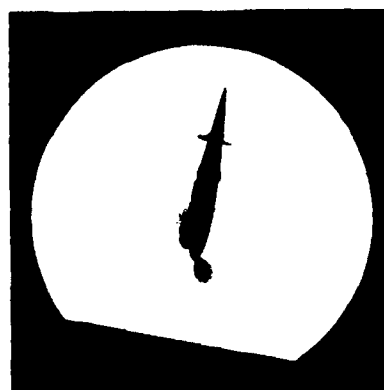
10.4°



10.8°



$\alpha = 15.0^\circ$

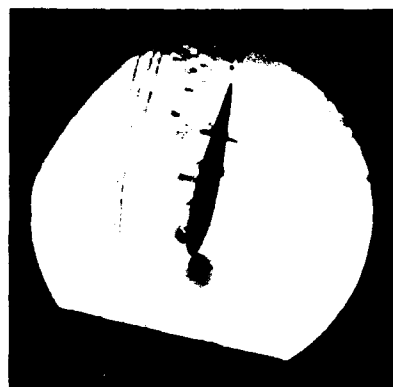


$\alpha = 10.0^\circ$

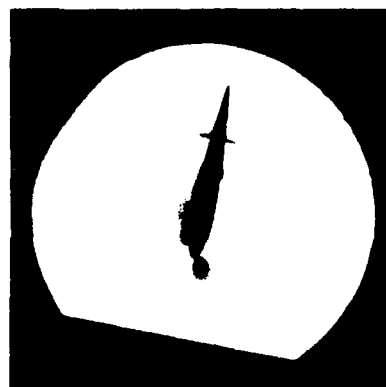
Figure 49. Reattachment; $M = 0.35$, $Re = 630,000$, $k = 0.050$



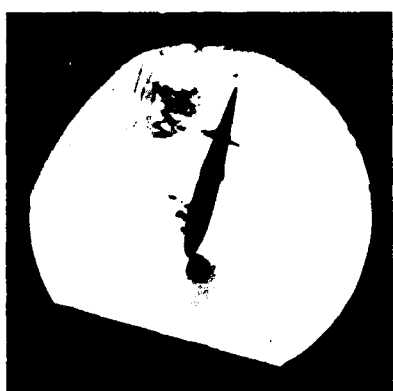
10.4°



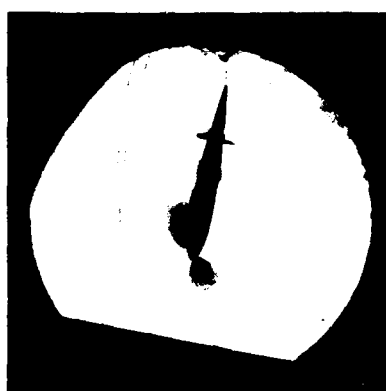
10.8°



9.6°

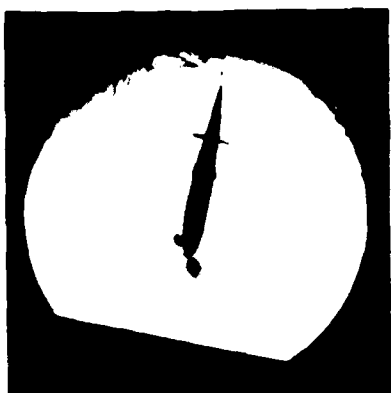


$\alpha = 15.0^\circ$

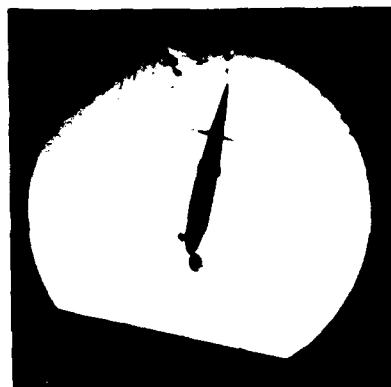


$\alpha = 10.0^\circ$

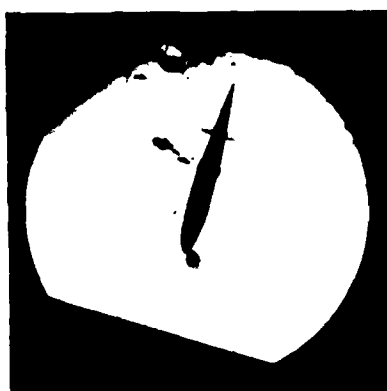
Figure 50. Reattachment; $M = 0.35$, $Re = 630,000$, $k = 0.075$



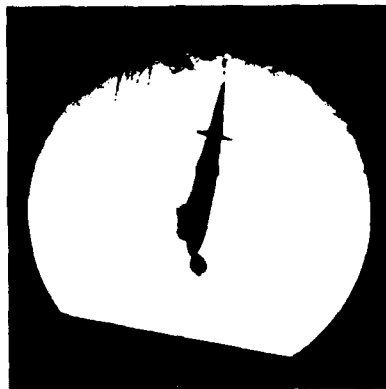
10.4°



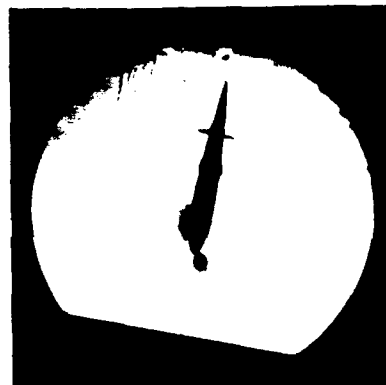
10.8°



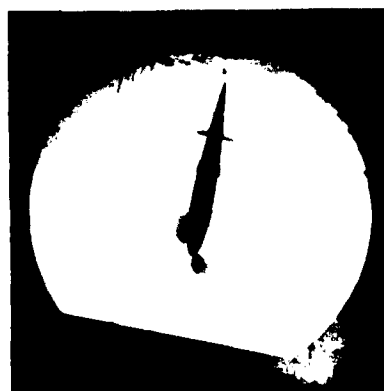
$\alpha = 15.0^\circ$



9.2°



9.6°



$\alpha = 10.0^\circ$

Figure 51. Reattachment; $M = 0.35$, $Re = 630,000$, $k = 0.10$



$\alpha = 15.0^\circ$



10.8°



10.4°



$\alpha = 10.0^\circ$

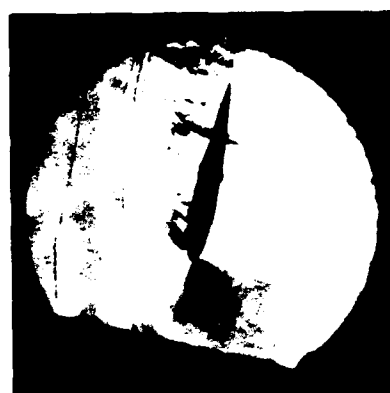


9.6°

Figure 52. Reattachment; $M = 0.40$, $Re = 720,000$, $k = 0.025$



10.4°



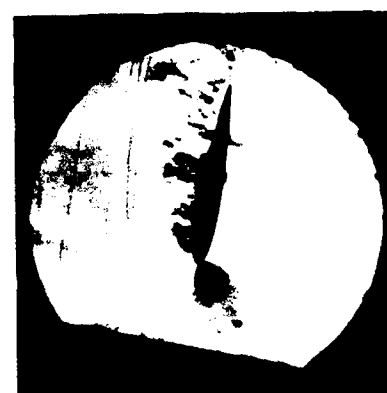
10.8°



$\alpha = 15.0^\circ$

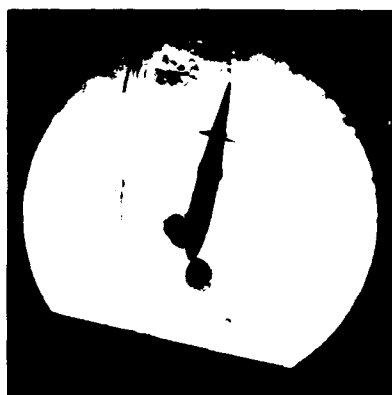


9.6°

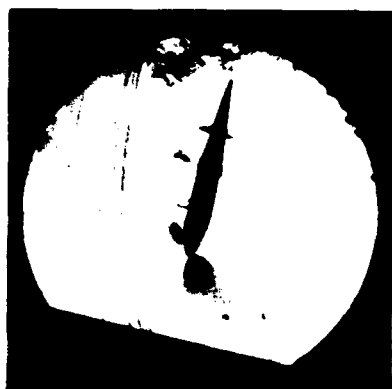


$\alpha = 10.0^\circ$

Figure 53. Reattachment; $M = 0.40$, $Re = 720,000$, $k = 0.050$



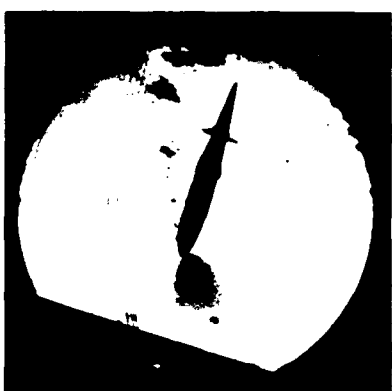
10.4°



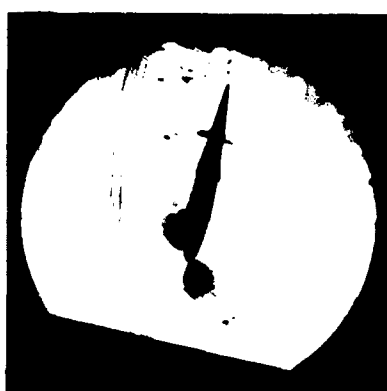
10.8°



9.6°



$\alpha = 15.0^\circ$



$\alpha = 10.0^\circ$

Figure 54. Reattachment; $M = 0.40$, $Re = 720,000$, $k = 0.075$

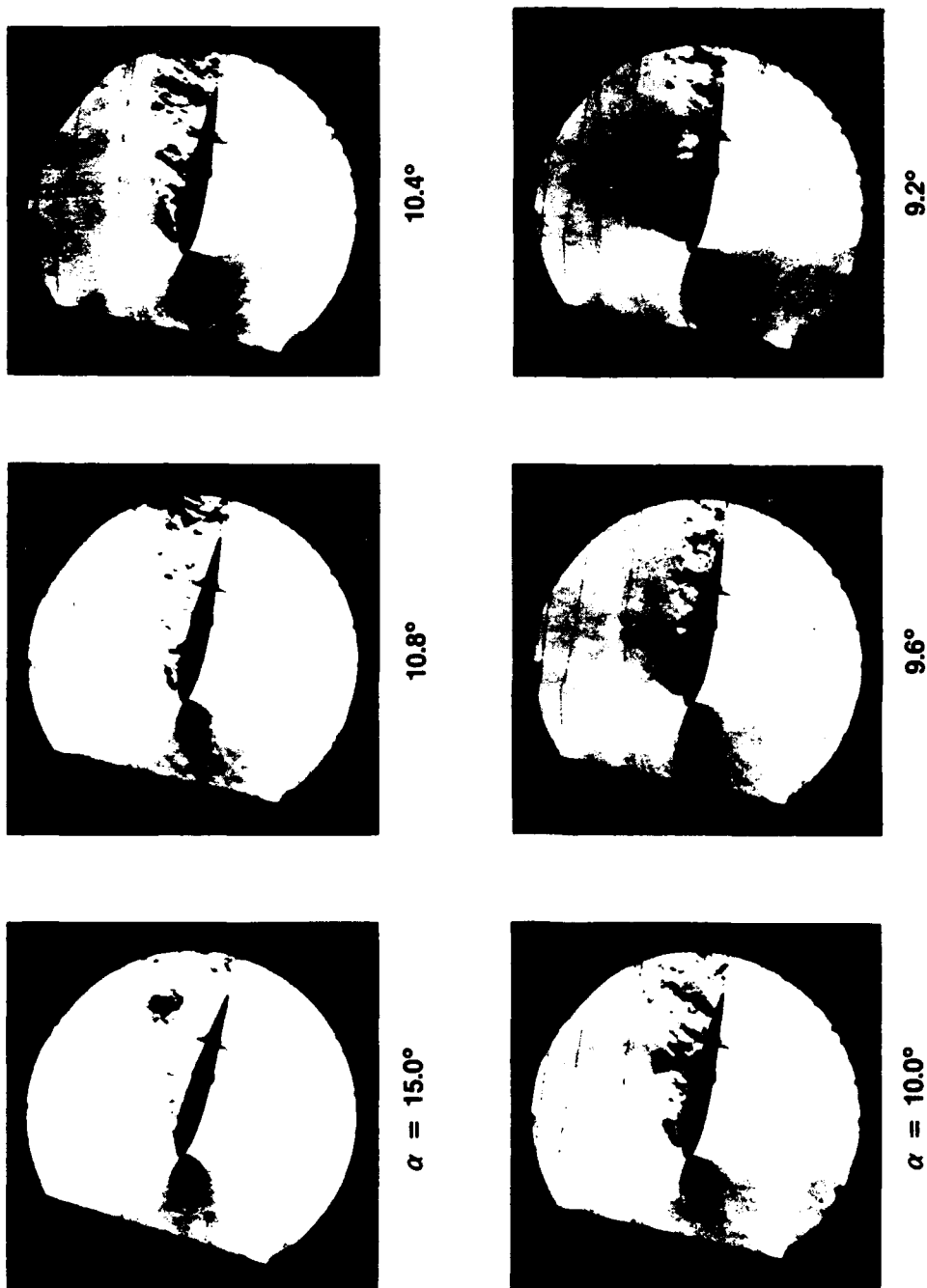
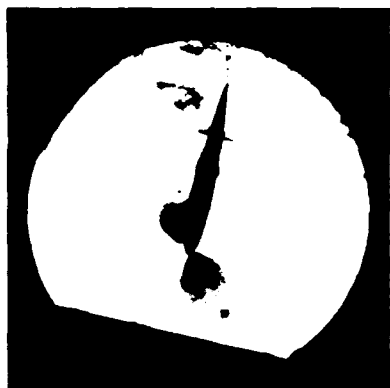
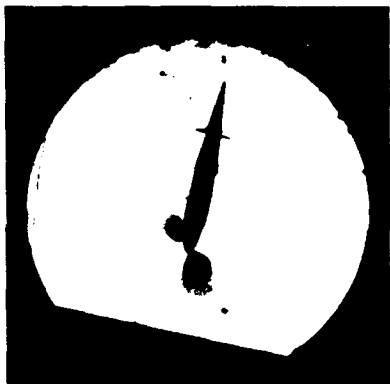


Figure 55. Reattachment; $M = 0.45$, $Re = 810,000$, $k = 0.025$



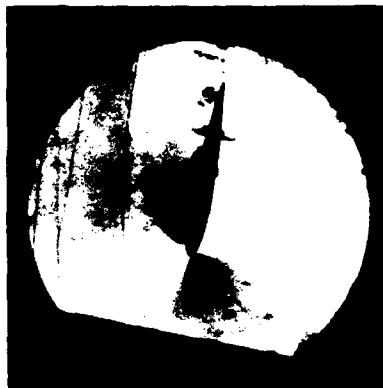
10.4°



10.8°



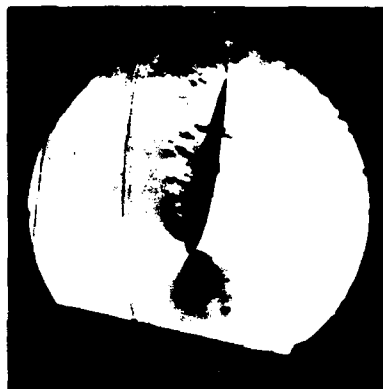
$\alpha = 15.0^\circ$



9.2°

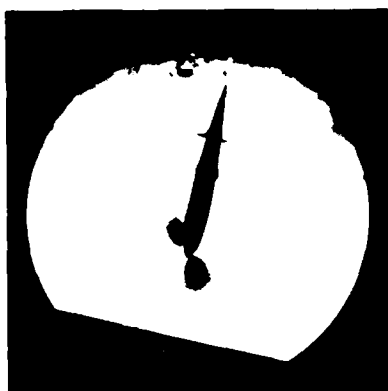


9.6°

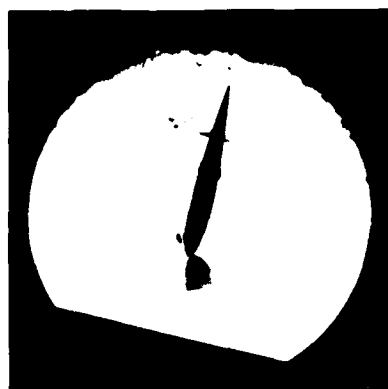


$\alpha = 10.0^\circ$

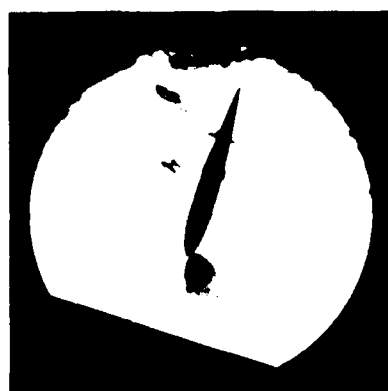
Figure 56. Reattachment; $M = 0.45$, $Re = 810,000$, $k = 0.050$



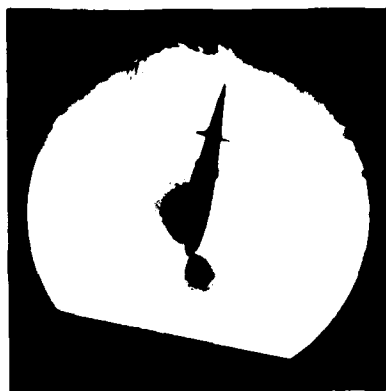
10.4°



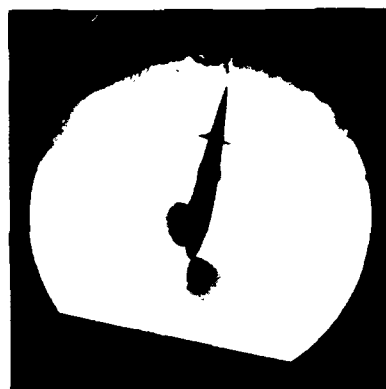
10.8°



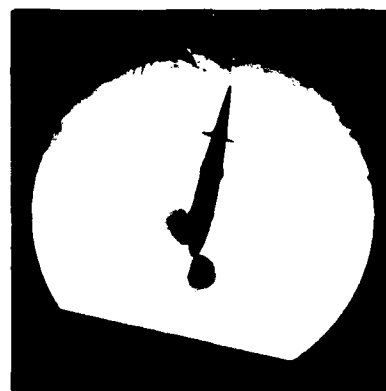
$\alpha = 15.0^\circ$



9.2°



9.6°



$\alpha = 10.0^\circ$

Figure 57. Reattachment; $M = 0.45$, $Re = 810,000$, $k = 0.075$

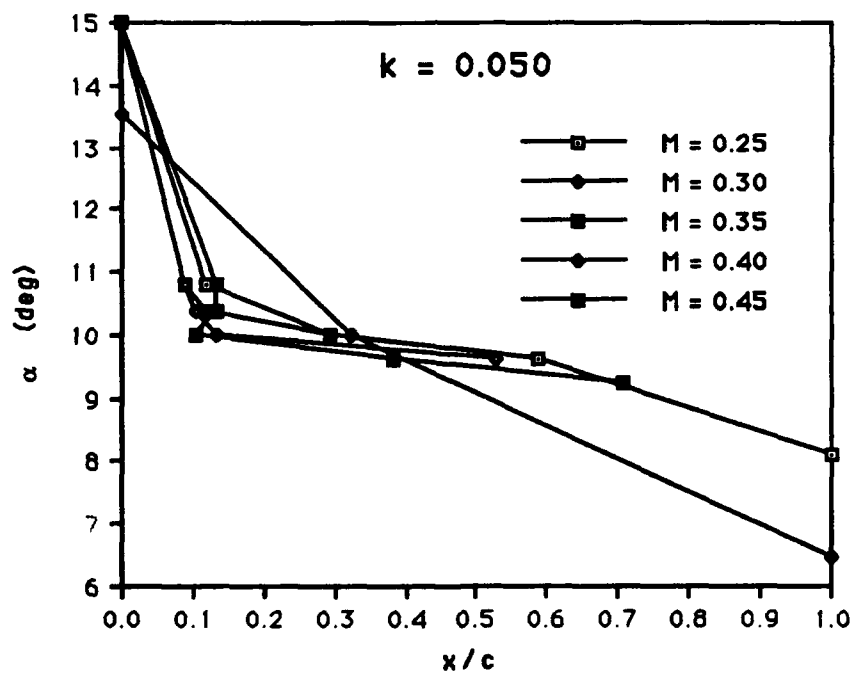
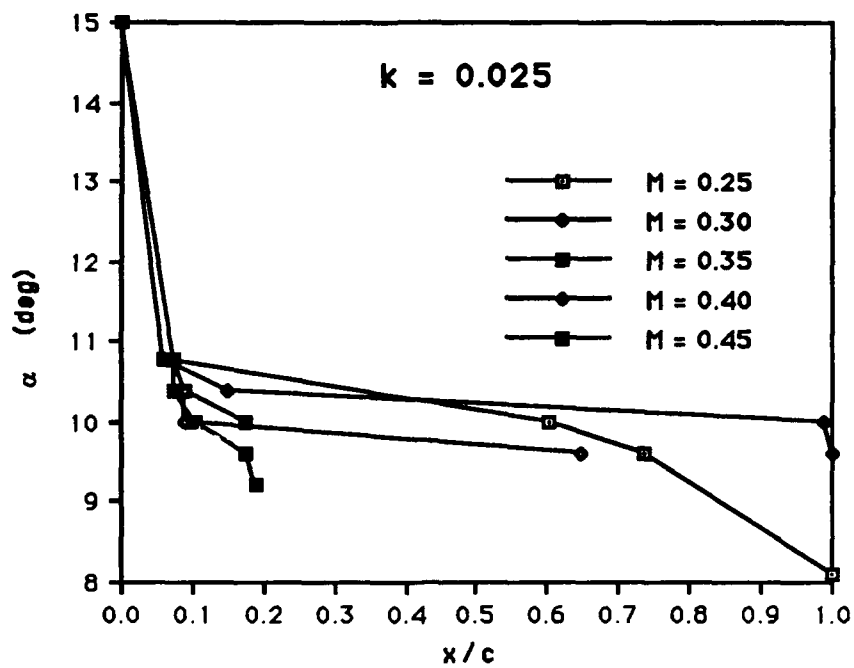


Figure 58. Compressibility Effects on Reattachment

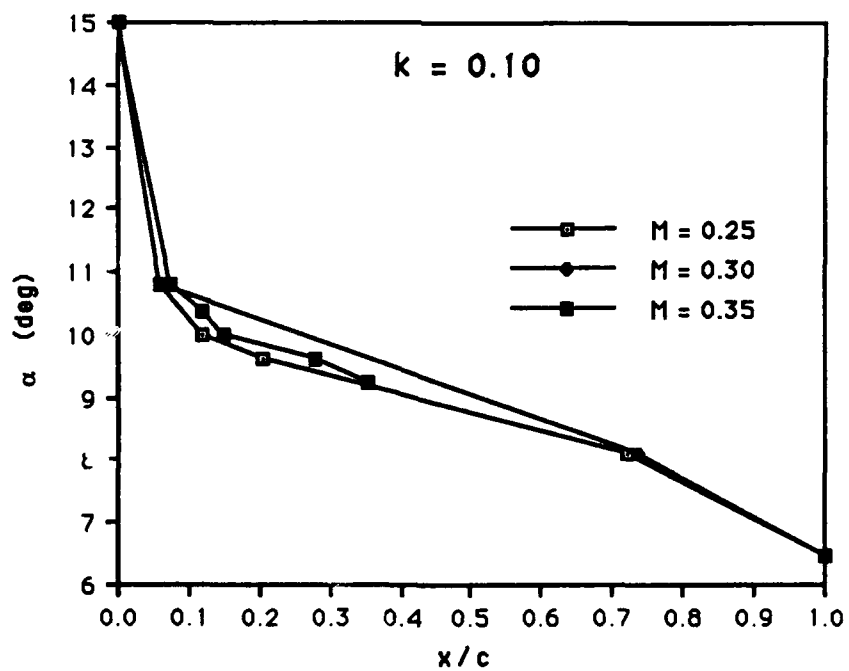
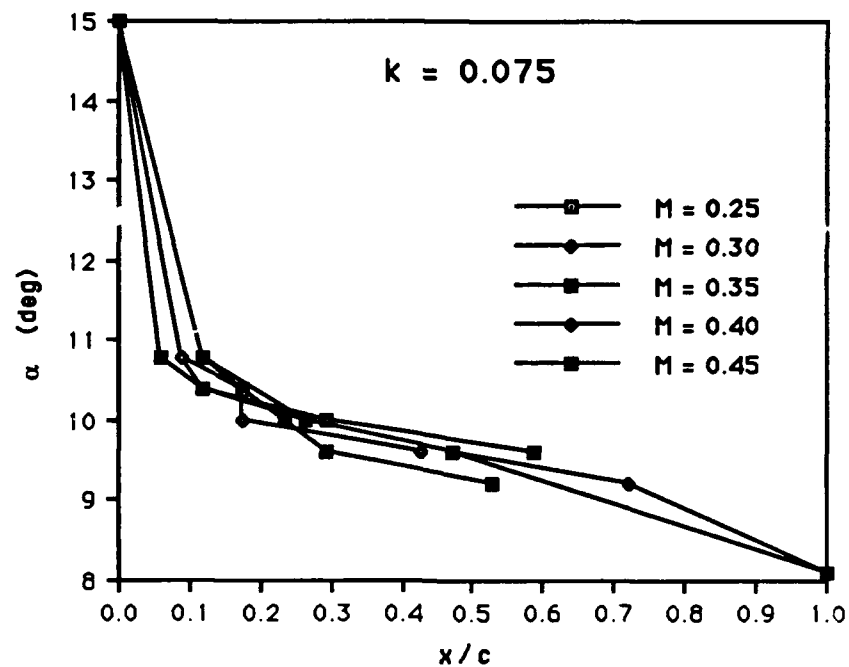


Figure 58. Compressibility Effects on Reattachment (Continued)

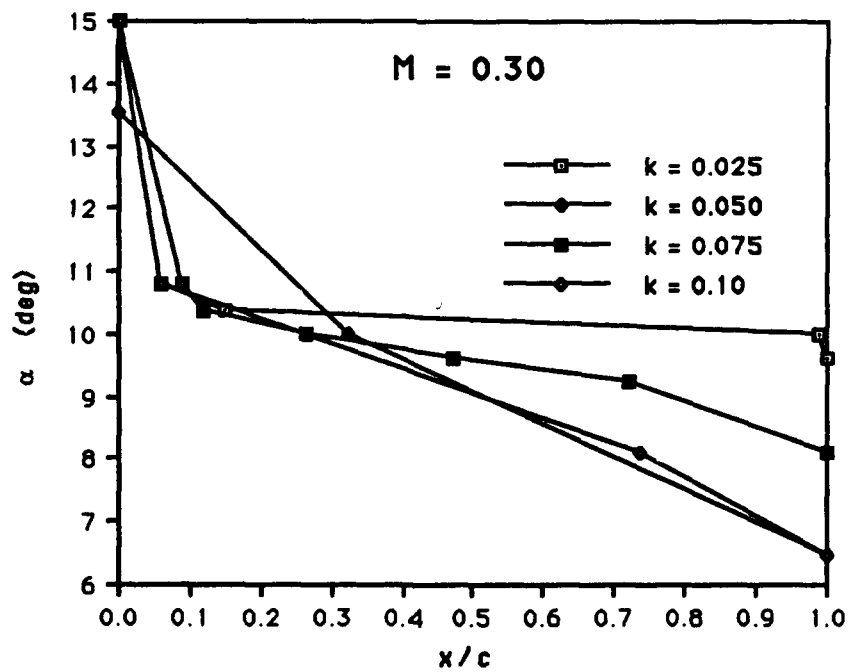
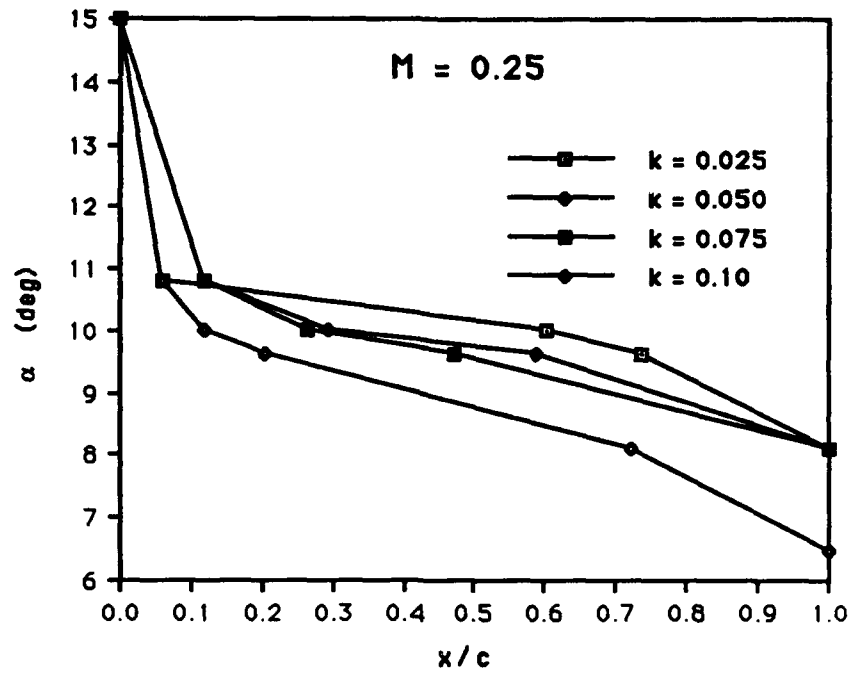


Figure 59. Reduced Frequency Effects on Reattachment

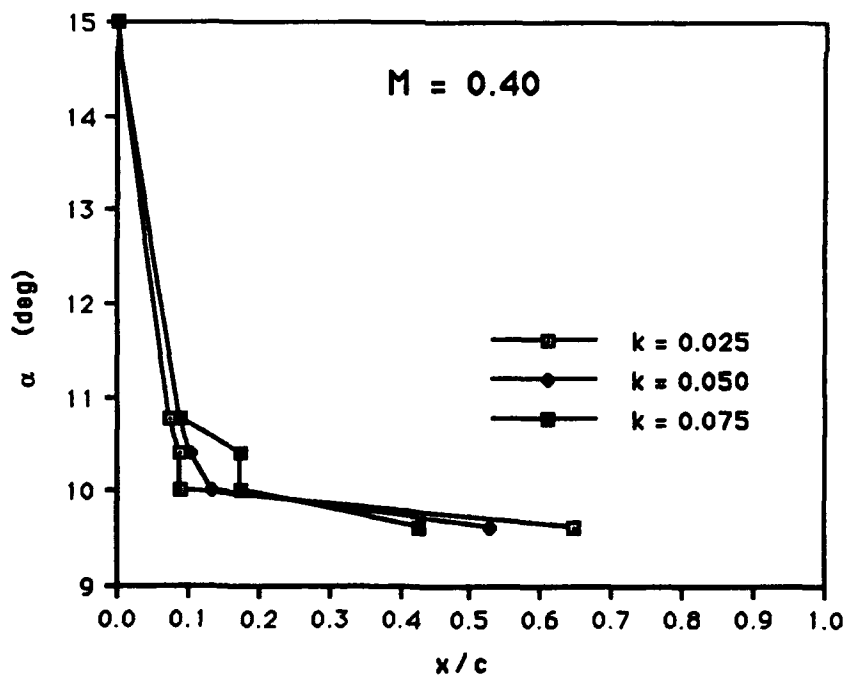
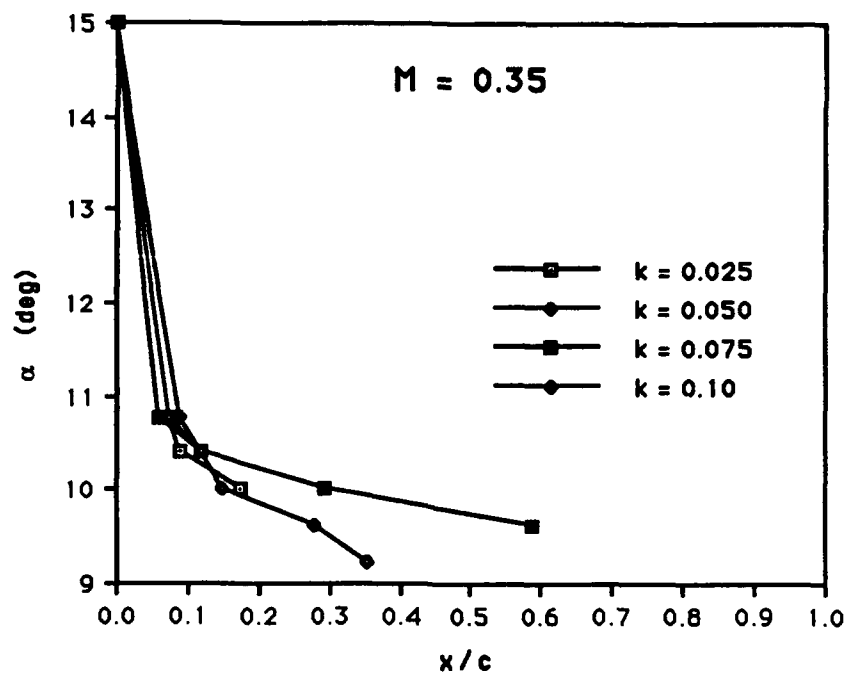


Figure 59. Reduced Frequency Effects on Reattachment (Continued)

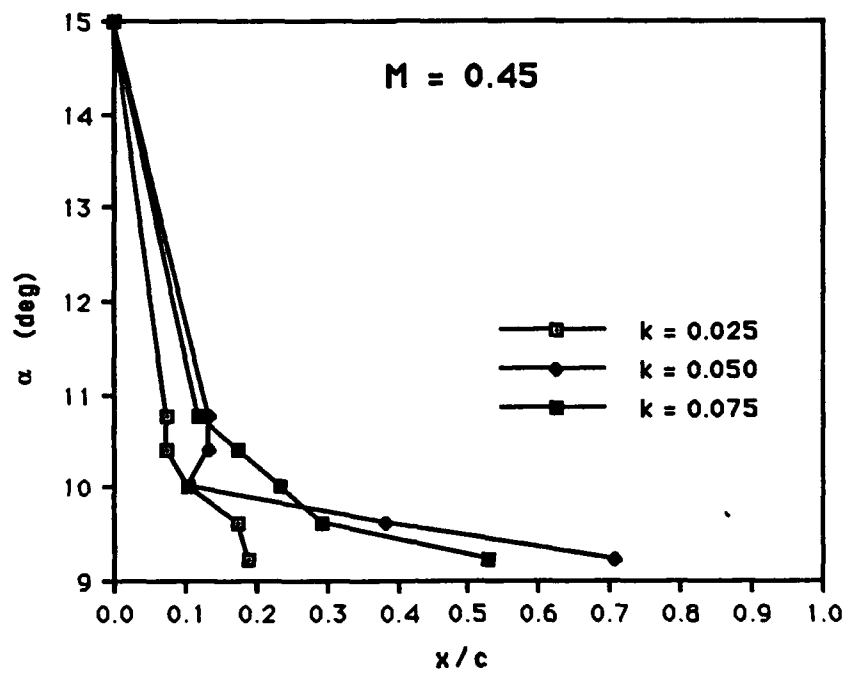


Figure 59. Reduced Frequency Effects on Reattachment (Continued)

LIST OF REFERENCES

1. Prouty, Raymond W., *Helicopter Performance, Stability and Control*, PWS Publishers, 1986.
2. NASA Technical Memorandum 81264, *The Phenomenon of Dynamic Stall*, by W. J. McCroskey, 1981.
3. Carr, L. W., "Progress in Analysis and Prediction of Dynamic Stall," *Journal of Aircraft*, v. 25, no. 1, pp. 6-17, January 1988.
4. American Institute of Aeronautics and Astronautics Paper 89-0023, *Flow Visualization Studies of the Mach Number Effects on the Dynamic Stall of an Oscillating Airfoil*, by M. Chandrasekhara and L. Carr, 9-12 January 1989.
5. Ericsson, L. E. and Reding, J. P., "Fluid Mechanics of Dynamic Stall, Part I: Unsteady Flow Concepts," *Journal of Fluids and Structures*, v. 2, pp. 1-33, 1988.
6. McCroskey, W. J., "Unsteady Airfoils," *Annual Review of Fluid Mechanics*, v. 14, pp. 285-311, 1982.
7. American Institute of Aeronautics and Astronautics Paper 89-0647, *Design and Development of a Compressible Dynamic Stall Facility*, by L. Carr and M. Chandrasekhara, 9-12 January 1989.
8. American Institute of Aeronautics and Astronautics Paper 75-488, *Measurement of Discrete Vortex Noise in a Closed-Throat Wind Tunnel*, by S. S. Davis, 24-26 March 1975.
9. Sticht, C. D., *Development of Drive Mechanism for an Oscillating Airfoil*, paper presented at the Symposium on Aerospace Mechanisms, NASA Langley Research Center, Langley, Virginia, 4-6 March 1988.
10. Goldstein, Richard J., *Fluid Mechanics Measurements*, Hemisphere Publishing Company, 1983.
11. National Aeronautics and Space Administration Technical Note D-8382, *Analysis of the Development of Dynamic Stall Based on Oscillating Airfoil Experiments*, L. W. Carr, K. W. McAlister, and W. J. McCroskey, January 1977.

12. National Aeronautics and Space Administration Technical Memorandum 84245, *An Experimental Study of Dynamic Stall on Advanced Airfoil Sections*, W. J. McCroskey, K. W. McAlister, L. W. Carr, and S. L. Pucci, July 1982.
13. American Institute of Aeronautics and Astronautics Paper 85-0527, *Review of Unsteady, Driven, Separated Flows*, W. C. Reynolds and L. W. Carr, March 1985.
14. Herring, D. G. F, Niven, A. J., Galbraith, R. A. McD., *Analysis of Reattachment During Ramp Down Tests*, paper presented at the Fourteenth European Rotorcraft Forum, Milano, Italy, 20-23 September 1988.

INITIAL DISTRIBUTION LIST

	No. Copies
1. Defense Technical Information Center Cameron Station Alexandria, VA 22304-6145	2
2. Library, Code 0142 Naval Postgraduate School Monterey, CA 93943-5002	2
3. Dr. E. R. Wood Chairman Department of Aeronautics and Astronautics, Code 67 Naval Postgraduate School Monterey, CA 93943	1
4. Dr. S. S. Davis Chief, Fluid Mechanics Laboratory NASA Ames Research Center (M.S. 260-1) Moffett Field, CA 94035	1
5. Dr. M. S. Chandrasekhara NASA Ames Research Center (M.S. 260-1) Moffet Field, CA 94035	5
6. Dr. M. F. Platzer Department of Aeronautics and Astronautics, Code 67 Naval Postgraduate School Monterey, CA 93943	1
7. Dr. L. W. Carr NASA Ames Research Center (M.S. 260-1) Moffet Field, CA 94035	1
8. Dr. J. A. Ekaterinaris NASA Ames Research Center (M.S. 260-1) Moffet Field, CA 94035	1
9. Dr. S. K. Hebbar Department of Aeronautics and Astronautics, Code 67 Naval Postgraduate School Monterey, CA 93943	1

- | | | |
|-----|--|---|
| 10. | D. P. Bencze
Chief, Applied Aerodynamics Branch
NASA Ames Research Center (M.S. 260-1)
Moffet Field, CA 94035 | 1 |
| 11. | Engineering Sciences Division
ATTN: T. L. Doligalski
Chief, Fluid Dynamics
U.S. Army Research Office
P.O. Box 12211
Research Triangle Park, NC 27709-2211 | 1 |
| 12. | Dr. R. E. Singleton
Director, Engineering Sciences Division
U.S. Army Research Office
P.O. Box 12211
Research Triangle Park, NC 27709-2211 | 1 |
| 13. | Directorate of Aerospace Sciences
ATTN: Hank E. Helin, Program Manager
AFOSR/NA
Bolling Air Force Base
Washington, D.C., 20332-6448 | 1 |
| 14. | Naval Air Systems Command
ATTN: Tom Momiyama
Code 931
Washington, D.C., 20361-9320 | 1 |
| 15. | Naval Air Systems Command
ATTN: B. Neumann, Program Manager
AIR 931K
Washington, D.C., 20361-9320 | 1 |
| 16. | Ms. Lisa Cowles
NADC Code 60C
Street Road
Warminster, PA 18974-5000 | 1 |
| 17. | Edward G. Brydges
3944 Bryony Road
Randallstown, MD 21133 | 1 |
| 18. | CPT (P) Bruce E. Brydges
92 Red Fox Drive
Savannah, GA 31419 | 5 |

- 19. 1LT Michael P. Slattery 1
572 Als Lane
Clarksville, TN 37042
- 20. Jerry Higman 1
Department of Aeronautics and Astronautics (Code 67)
Naval Postgraduate School
Monterey, CA 93940